COMPARISON OF WELD CHARACTERISTICS OF AXISYMMETRICAL AND NON-AXISYMMETRICAL BUTT WELDED PIPE JOINTS

By

SATISH KUMAR VELAGA

(ENGG02201104020)

INDIRA GANDHI CENTER FOR ATOMIC RESEARCH

KALPAKKAM

A thesis submitted to the

Board of Studies in Engineering Sciences

In partial fulfillment of requirements

for the Degree of

DOCTOR OF PHILOSOPHY

of

HOMI BHABHA NATIONAL INSTITUTE

SEPTEMBER, 2015

Homi Bhabha National Institute

Recommendations of the Viva Voce Committee

As members of the Viva Voce Committee, we certify that we have read the dissertation prepared by **Satish Kumar Velaga** entitled **"Comparison of Weld Characteristics of Axisymmetrical and Non-Axisymmetrical Butt Welded Pipe Joints"** and recommend that it may be accepted as fulfilling the thesis requirement for the award of Degree of Doctor of Philosophy.

_______________________________ **Date:** 1/4/2016
Chairman - Dr. K. Velusamy

_______________________________ **Date:** 1/4/2016
Guide / Convener - Dr. S. Venugopal

_______________________________ **Date:** 1.4.2016
External Examiner -Prof. K.P. Karunakaran

_______________________________ **Date:** 1/4/2016
Member 1 - Dr. Shaju K Albert

_______________________________ **Date:** 01.04.2016
Member 2 - Dr. S. Murugan

_______________________________ **Date:** 01/04/16
Technology Adviser - Dr. A. Ravisankar

Final approval and acceptance of this thesis is contingent upon the candidate's submission of the final copies of the thesis to HBNI.

I hereby certify that I have read this thesis prepared under my direction and recommend that it may be accepted as fulfilling the thesis requirement.

Date: 1/4/2016
Place: Kalpakkam

Dr. S. Venugopal
(Guide)

STATEMENT BY AUTHOR

This dissertation has been submitted in partial fulfillment of requirements for an advanced degree at Homi Bhabha National Institute (HBNI) and is deposited in the Library to be made available to borrowers under rules of the HBNI.

Brief quotations from this dissertation are allowable without special permission, provided that accurate acknowledgement of source is made. Requests for permission for extended quotation from or reproduction of this manuscript in whole or in part may be granted by the Competent Authority of HBNI when in his or her judgment the proposed use of the material is in the interests of scholarship. In all other instances, however, permission must be obtained from the author.

Kalpakkam,

Date: 01/04/2016

V. Satish

Satish Kumar Velaga

DECLARATION

I, hereby declare that the investigation presented in the thesis has been carried out by me. The work is original and has not been submitted earlier as a whole or in part for a degree / diploma at this or any other Institution / University.

Kalpakkam,

Date: 01/04/2016

V. Satish

Satish Kumar Velaga

List of Publications

Publications in Refereed Journal:

a. Published:

1) A. Ravisankar, **Satish Kumar Velaga,** Gaurav Rajput, S. Venugopal., Influence of welding speed and power on residual stress during Gas Tungsten Arc Welding (GTAW) of thin sections with constant heat input: A study using numerical simulation and experimental validation. ***Journal of Manufacturing Processes,*** **2014,** Vol. 16, 200-11. http://dx.doi.org/10.1016/j.jmapro.2013.11.002. **(ScienceDirect most downloaded article).**

2) **Satish K. Velaga,** Gaurav Rajput, S. Murugan, A. Ravisankar, S. Venugopal., Comparison of weld characteristics between longitudinal seam and circumferential butt weld joints of cylindrical components. ***Journal of Manufacturing Processes,*** **2015,** Vol. 18, 1-11. http://dx.doi.org/10.1016/j.jmapro.2014.11.002. **(ScienceDirect most downloaded article).**

3) **Satish K. Velaga**, Gaurav Rajput, T. Selvaraj, B.M. Anandarao, A. Ravisankar., A study on the effect of weld induced residual stresses and the influence of weld sequencing of centrifugal extractor rotating bowl using numerical simulation and experimental validation. ***Ciência & Tecnologia dos Materiais,*** **2015,** Vol. 27, 84-91. http://dx.doi.org/10.1016/j.ctmat.2015.03.011 ***(journal of the Portuguese Society of Materials).***

b. Communicated:

1) **Satish K. Velaga,** S. Arun kumar, A. Ravisankar, S. Venugopal., Weld characteristics of non-axisymmetrical butt welded branch pipe T-joints using finite element simulation and experimental validation. ***International Journal of Pressure Vessels and Piping (IJPVP).***

2) **Satish K. Velaga,** A. Ravisankar, S. Venugopal., Finite element based parametric study on the characterization of GTAW process moving heat source parameters in austenitic stainless steel. ***Archives of Civil and Mechanical Engineering (ACME).***

Publications in International Conference Proceedings:

1) A. Ravisankar, **Satish Kumar Velaga**, Gaurav Rajput, S. Murugan, S. Venugopal., Numerical simulation of welding distortion: A comparative study of variable weld speeds and powers with constant heat input, Int. conference on advances in manufacturing technology -- ***ICAMT: 2012***, Chennai, India, June 15-17, 2012.

2) **Satish K. Velaga**, Gaurav Rajput, S. Murugan, A. Ravisankar, S. Venugopal., Numerical study on the characterization of Goldak's double ellipsoid heat source parameters in thermal analysis of GTAW process. International congress of International institute of welding - ***IC-IIW: 2014***, NewDelhi, India, April 09-11, 2014.

3) **Satish K. Velaga**, Gaurav Rajput, T. Selvaraj, B.M. Anandarao, A. Ravisankar., A study on the effect of weld induced residual stresses and the influence of weld sequencing of centrifugal extractor rotating bowl using numerical simulation and experimental validation. 2nd International Conference of the International Journal of Structural Integrity - ***IJSI: 2014,*** **Funchal, Madeira, Portugal,** September 1-4, 2014.

Publications in National Seminar:

1) **Satish K. Velaga**, A. Ravisankar, S. Venugopal., Numerical investigation of thermo mechanical behavior during circumferential GTAW process of AISI 304 component. National welding seminar – ***NWS: 2015,*** Mumbai, India, December 09-11, 2015.

2) **Satish K. Velaga**, A. Ravisankar, S. Venugopal., Finite element based parametric study of moving heat source model on weld induced residual stress distributions. National welding seminar – ***NWS: 2015,*** Mumbai, India, December 09-11, 2015.

V. Satish

(Satish Kumar Velaga)

DEDICATION

The thesis is dedicated
to
my Family.

ACKNOWLEDGEMENTS

The thesis work was carried out under the guidance of Dr. S. Venugopal, Director, Metallurgy and Materials Group (MMG), Indira Gandhi Centre for Atomic Research (IGCAR), Kalpakkam. I sincerely thank for his guidance, excellent support, continuous encouragement and motivation.

I wish to thank my doctoral committee chairmen Dr. T. Jayakumar and Dr. K. Velusamy and members Dr. Shaju K Albert and Dr. S. Murugan for time-to-time evaluation of the research work and useful suggestions, which definitely improved the thesis. I would also express my sincere thanks to Dr. A. Ravisankar, Project Director, Fast Reactor Fuel Cycle Facilities, for his concurrence and support to take up this doctoral research.

I gratefully express my heartfelt gratitude to my brother Prof. Nagendra R. Velaga, Indian Institute of Technology, Mumbai, for his valuable suggestions, comments and support in various aspects while preparing the thesis and manuscripts for journals. I wish to acknowledge and thank Dr. C. Phaniraj, MMG, for his directions with patience which gave me immense confidence to write scientific articles.

I am also deeply obliged to Mr. Kempulraj, Head, Central Workshop Division and his team for their support and help during welding experiments and transient temperature measurements. I thank Mr. S. Mahadevan and Mr. S. Arun Kumar for their support during residual stress measurements.

Finally, I like to express my deepest gratitude to my parents, Shri. Subba Rao Velaga and Smt. Rama Devi who have provided me the ideal environment to grow up and make my career smooth. I would like to express my warmest appreciation to my wife Smt. Silpa, my lovely daughter Soumya and my little son Sushanth whose love, affection, sacrifices and encouragement is boundless.

Above all, I thank the Almighty, without whose wish and blessing, this work would never have seen its successful accomplishment. Thank you everyone.

TABLE OF CONTENTS

SYNOPSIS

Cylindrical shell structures comprise an important class of axisymmetrical and Non-Axisymmetrical (N-A) butt welded joints; and are extremely utilized in most of the engineering applications. The reliability of components and structures in the form of butt welded axisymmetrical and N-A joints are highly essential. In nuclear reprocessing plants, some of the important process vessels and equipment such as annular tanks, cylindrical tanks, vent pots, high level waste storage tanks etc. need to be fabricated either by Longitudinal Seam (L-Seam) weld joining (or) Circumferential Seam (C-Seam) weld joining process. In general, components whose diameters are equivalent to available standard pipe sizes are developed by carrying out C-Seam weld joining. On the other hand, components which are not equivalent to available standard pipe sizes are fabricated by L-Seam weld joining of rolled plates. It is of great interest to use L-Seam welds while fabricating large diameter components in order to reduce production costs. The cost reduction can be as high as 30% by adopting L-Seam welding. Also, Branch Pipe T-joints (BP-T-joints) are extensively used in different engineering applications. These BP-T-joints can be produced by two ways: (1) by joining run pipe and branch pipes using three circumferential axisymmetrical butt weld joints with the cast/forged pipe tee joint and (2) by using a single N-A butt weld joint. The single N-A butt weld joint has an important advantage of decrease in weld length compared to three circumferential axisymmetrical butt weld joints. The decrease in weld length results in cost reduction by 2.5 to 3 times. Further, in nuclear spent fuel reprocessing plants, Centrifugal Extractors (CE) are the most preferred extraction equipment for the separation of fissile material. During fabrication of axisymmetrical thin section high speed CE rotating bowls, several important factors such as heat input, weld speed, groove geometry, number of passes and weld sequencing are to be considered. Therefore, several axisymmetrical and N-A butt welded joints are the mandatory integrating techniques for different engineering applications, where specific strength and cost effectiveness are the major design constraints. Thus, in the present research, different weld characteristics such as microstructures, physical properties, transient temperature distributions, residual stress fields and distortion patterns for different axisymmetrical and N-A butt welded joints are investigated in detail.

For the accurate numerical simulation of the gas tungsten arc welding process, it is very important to implement the correct size and distribution of the moving heat source. Any slight variation in the geometrical parameters of heat source model, affect the weld characteristics and shape and boundaries of Fusion Zone (FZ) and Heat Affected Zone (HAZ). Therefore, several aspects for evaluating the geometric parameters of Goldak's double ellipsoidal moving heat source model are carried out prior to the assessment of weld characteristics for various axisymmetrical and N-A butt welded joints. The simulation strategy is developed and implemented by using commercially available Finite Element (FE) software SYSWELD. In this study, a Three Dimensional (3D), sequentially coupled thermo-metallurgical-mechanical analysis is performed with temperature dependent thermal and mechanical parameters. Also, various aspects such as latent heat effects during phase transformation, hardening behavior (i.e. isotropic, kinematic and mixed) and phase dependent strain hardening are considered during the analysis. In this research, several weld experiments are carried out to obtain the heat input and the macrographs which are further validated with the predicted weld molten pool sizes during

Heat Source Fitting (HSF) analysis. The Goldak's double ellipsoid heat source function obtained in HSF analysis is employed in the subsequent thermal and mechanical analysis. Further, an in-depth comparative study of weld characteristics for different cases of axisymmetrical and N-A butt welded joints is performed; in order to improve their fatigue life, reduction in stress corrosion cracking and fracture.

The results reveal that there are significant differences in 3D temperature profiles, temperature distributions and residual stress states between L-Seam and C-Seam butt joints; and run and branch pipes for different pipe sizes along different sections. The major contribution of this investigation is: (i) L-Seam weld joints are not advisable to use while fabricating cylindrical components in order to improve the service life; (ii) Joining of branch pipes to main pipes by using a single N-A butt weld joint is the most successful method with respect to cost, service life, weld length and FZ/HAZ volume; and (iii) Residual stress distributions for the three plane axisymmetrical butt weld joint are investigated and their inferences on the CE rotating bowl are discussed. In this investigation series of full scale shop floor welding experiments are also performed to verify the effectiveness of the developed FE simulation strategy by validating for the transient temperature distributions and residual stress fields.

LIST OF FIGURES

LIST OF TABLES

NOMENCLATURE

Symbol	Description
ρ	Density of the material
C	Specific heat
K	Thermal conductivity
h_f	Convective heat transfer coefficient
Q	Internal heat generation per unit volume
U	Internal work
P	External work
δ	Virtual operator
ε	Total strain
ε_e	Elastic strain
ε_p	Plastic strain
ε_{th}	Thermo-metallurgical strain
ε_{tr}	Transformation strain
ε_c	Creep strain
f_i	Phase proportion of phase 'i'
T	Body temperature
T_0	Sink temperature
T_∞	Surrounding temperature
h_{conv}	Convective heat transfer coefficient
q_{conv}	Heat loss due to convection

ε^1	Emissivity constant
σ^1	Stefan-Boltzmann constant
H	Enthalpy
q_f	Heat flux in the front quadrant of double-ellipsoid heat source
q_r	Heat flux in the rear quadrant of double-ellipsoid heat source
I	Current
V	Voltage
η	Arc efficiency (%)
a_f	Length of front double-ellipsoid heat source
a_r	Length of rear double-ellipsoid heat source
b	Half width of double-ellipsoid heat source
c	Penetration depth of double-ellipsoid heat source
f_f	Fractional factors of heat deposited front double-ellipsoid
f_r	Fractional factors of heat deposited rear double-ellipsoid
T_{max}	Peak temperature
S	Weld speed
R_i	Inner radius of cylinder
D	Outer diameter of cylinder
r	Cylinder mean radius
t	Wall thickness of cylinder
E	Young's Modulus

ΔT	Difference between the reference temperature and actual temperature
U_x	Displacement in x-direction
U_y	Displacement in y-direction
U_z	Displacement in z-direction
L-8	L-Seam-8 inch Dia.
L-6	L-Seam-6 inch Dia.
C-8	C-Seam-8 inch Dia.
C-6	C-Seam-6 inch Dia.
s	Second (time)

Abbreviation	Meaning
SCC	Stress Corrosion Cracking
BP-T-Joint	Branch Pipe T-Joints
N-A	Non-Axisymmetrical
CE	Centrifugal Extractor
L-Seam	Longitudinal Seam
C-Seam	Circumferential Seam
ASTM	American Society for Testing and Materials
FEA	Finite Element Analysis
FE	Finite Element
SS	Stainless Steel
ASS	Austenitic Stainless Steel
WZ	Weld Zone
RP	Run Pipe
BP	Branch Pipe
FZ	Fusion Zone
HAZ	Heat Affected Zone
NB	Nominal Bore
GTAW	Gas Tungsten Arc Welding
HSF	Heat Source Fitting
3D	Three Dimensional

2D	Two Dimensional
1D	One Dimensional
SHS	Square Hollow Sections
CHS	Circular Hollow Sections
FEM	Finite Element Method
TIG	Tungsten Inert Gas
BC	Boundary Conditions / Boundary Condition
XRD	X- Ray Diffraction
WC	Weld Center
S/E	Start/End
WL	Weld Location
r/t	Mean radius to Thickness ratio
R_i/T	Inner radius to Wall thickness ratios

CHAPTER - 01

INTRODUCTION

Welding is one of the most important joining techniques employed in majority of industries like nuclear, aeronautical and aerospace, shipbuilding and pressure vessel applications for production of high resilient components. Weld joining offers some significant advantages including weight & cost savings and improved structural integrity [1]. However, during the welding process, the base metal and weld metal regions near the weld undergoes severe thermal cycles. These highly localized thermal cycles produce inhomogeneous plastic deformation, which results in weld induced imperfections like residual stresses of the order of material yield strength and distortions. Both weld induced residual stress and distortion can significantly affect the performance and reliability of the welded component [2]. As a widely used joining technique, welding offers different technical challenges to the welding community. Since, tremendous efforts were made in the last couple of decades showing considerable technological innovations in weld joining technologies for defect free resilient structures capable of excellent in-service thermal and structural load bearing features. Despite these remarkable developments in high temperature joining technologies, the problems of weld induced imperfections is still a major confront for the welding engineers. In order to control weld induced imperfections and their distribution, a thorough understanding of the mechanism of development is required. The measurement of temperature distribution and residual stresses in the regions adjacent to the weld during and after the welding process is of prime importance in the improvement of fatigue life, reduction in Stress Corrosion Cracking (SCC) and fracture [3].

1.1. Welding residual stresses and distortions:

Residual stresses are locked-in stresses present in engineering components even when there is no external load and restraints. Various technical terms have been used to represent residual stress, such as initial stress, inherent stress and reaction stress [4]. These residual stresses can be either tensile or compressive depending upon the location and type of non-uniform volumetric change taking place.

The main reasons for the development of residual stresses in a welded component are due to non-uniform heating and cooling of metal in and adjacent to the weld region, microstructural change of metal, solid state phase change and volumetric strain of metal during solidification.

Type and magnitude of the residual stress vary continuously during different stages of welding. During heating, primarily compressive residual stress is developed in the region of weld metal due to thermal expansion and the same (thermal expansion) is constrained by the low temperature surrounding base metal. During cooling as metal starts to contract, tensile residual stresses develop if shrinkage is not allowed either due to adjacent metallic continuity or restraint from job clamping. The residual stress magnitude keeps on increasing until room temperature is attained. Hence, after cooling, tensile residual stress develops in the vicinity of weld area, while the surrounding areas are subjected to compressive residual stresses to maintain self-equilibrium state [5].

Fig. 1.1 shows the schematic representation of longitudinal and transverse residual stresses in a rectangular plate [5]. Due to heating and cooling cycles and restraints from adjacent materials, high longitudinal stress is developed at central section of the plate. As the distance from the Weld Center (WC) increase, the longitudinal stress gradually decreases. Along the transverse direction, the longitudinal stress changes to compressive, whereas along the longitudinal direction it reduces to zero, as stated by the equilibrium condition of residual stresses. Also, transverse residual stress is distributed with minor changes compared to longitudinal stress and smaller magnitudes are observed.

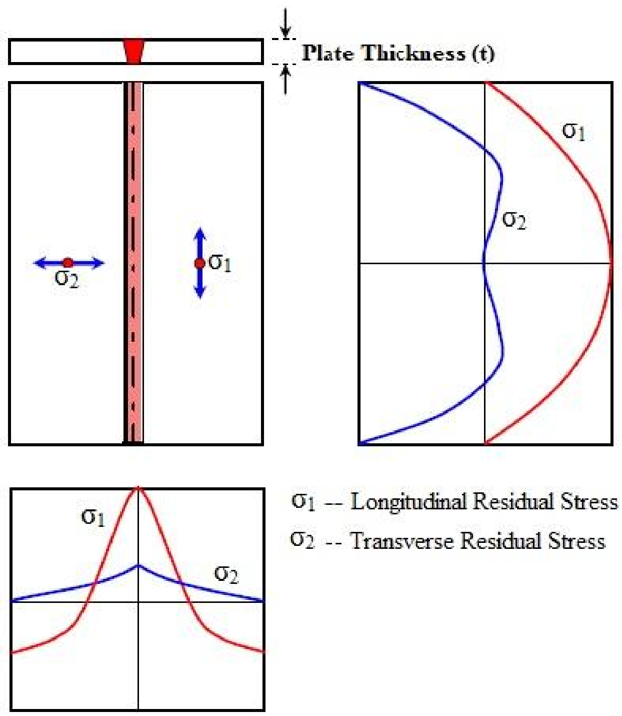

Fig. 1.1 Residual stresses in a welded rectangular plate.

The residual stress distribution and distortion pattern in a circumferentially welded cylinders/pipes are more complex. In this case, axial shrinkage and the radial deflection are the two dominating factors. The schematic representation of deformation patterns and the free body diagram of resultant forces are shown in Fig. 1.2 [6]. The expansion and shrinkage patterns in an axisymmetrical Circumferential Seam (C-Seam) butt welded pipe are shown in Fig. 1.2(a). The weld expansions and shrinkages in different directions induce circumferential force (F), shearing force (Q) and bending moments (M), to the butt welded pipe as show in Fig. 1.2(b). These forces are the resultants for the residual stresses in both circumferential and axial directions. Hence, the distribution of residual stresses in a C-Seam butt welded pipe is affected by many factors such as diameter, wall thickness of the pipe, weld geometry, material, welding procedure and sequence.

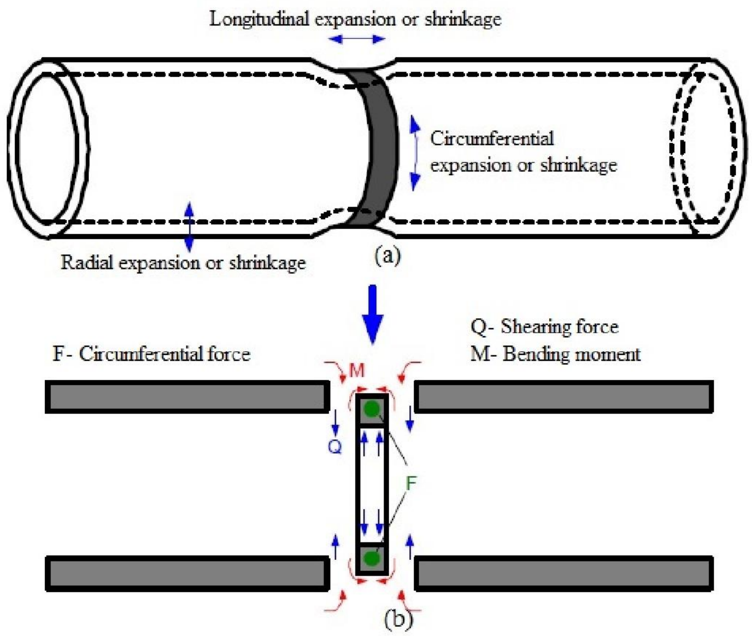

Fig. 1.2 (a) Expansion and shrinkage patterns in a circumferentially butt welded component and (b) Resultant forces at the weld.

Welding distortion or deformation is caused by the non-uniform expansion and contraction of the weld and base metal during the heating and cooling cycle. Different types of distortion patterns for C-Seam butt welded component are shown in Fig. 1.2(a). During fusion welding of plates, six different types of distortions are observed such as (a) transverse, (b) longitudinal, (c) angular, (d) rotational, (e) longitudinal bending, and (f) buckling [7]. The extent of welding distortion for both cylinders and plates depends on (a) geometry of the joint, (b) type of weld preparation, (c) rate of heat input during welding process, (d) volume of weld deposition, (e) alignment of structural elements, and (f) the sequence in which welds are made. Further, in the recent past many researchers presented the mechanism involved and the factors influencing different types of weld induced distortions [8-11]. During fusion welding of cylindrical components and plates both the residual stress and distortion are generated due to restraints by the fixtures or due to adjacent materials to the weld. If the restraints are partly removed, these stresses can cause the base material to distort and may even result in fractures or tears. Another significant disadvantage of welding distortion is that the productivity is decreased due to additional manufacturing steps involved. Hence, distortion is very costly and difficult to correct, so prevention is important. In this regard, a thorough understanding on the distortion, residual stresses and the influence of various welding parameters on the distribution of weld induced imperfections are required. The measurement of temperature distributions, residual stresses and distortion patterns adjacent to weld regions during and after the welding process is of prime importance for understanding the nature and behavior of the distortion, residual stresses and the influence of process parameters on the performance of welded component.

1.2. Industrial Relevance:

In the recent years, the welding segment in the manufacturing industry seems to be fastest growing. The growth of the welding industry has been approximately 4% per year. The fusion welding process is extensively used in different engineering applications such as nuclear power plants, petroleum refineries, chemical processing plants, super critical power generation plants and pressure vessel industries. For instance, Figs. 1.3(a)-(c), show three different applications such as, cylindrical tank, high radioactive level waste transfer container and vent pot; which are being used in nuclear spent fuel reprocessing industry are fabricated by Longitudinal Seam (L-Seam) weld joining process. Because, components whose diameters are equivalent to available standard pipe sizes are developed by carrying out C-Seam weld joining. On the other hand, components which are not equivalent to standard pipe sizes are fabricated by L-Seam weld joining of rolled plates. Also, Figs. 1.4(a) and (b), represents the containers fabricated by both L-Seam and C-Seam weld joints; which are being used in chemical processing industries.

Further, Branch Pipe T-joints (BP-T-joints) are extensively used in different engineering applications such as nuclear power plants, petroleum refineries, chemical processing plants, super critical power generation plants and pressure vessel industries. These BP-T-joints can be produced by two ways: (1) by joining run pipe and branch pipes using three C-Seam butt weld joints with the cast/forged pipe tee joint as shown in Fig. 1.5(a) and (2) by using a single Non-Axisymmetrical (N-A) butt weld joint as shown in Fig. 1.5(b).

On the other hand, Centrifugal Extractor (CE) is used in the fast reactor spent fuel reprocessing plants to recover valuable uranium and plutonium from radioactive solution leaving by solvent extraction step using 30% Tributyl phosphate in an alkane diluents as solvent. The CE has the advantages of fine dispersion through shearing of liquid layers between the stationary and rotating bowls. In addition to this, it has fast phase separation due to high centrifugal field in the order of 200 to 1000g. This leads to reduced contact time and less radiation damage to solvent. Steady state is achieved faster and stage equilibrium will not be disturbed due to stoppage of unit unlike pulse columns or mixer settlers. The design of this particular equipment is such that the level of precision on its dimensions required for the bowl itself is extremely critical. A typical CE rotating bowl and its parts are shown in Fig. 1.6. Ideally the CE rotating bowl, being a single integral unit; has to be machined as a single piece by special machining techniques. Since the complex machining techniques are not available indigenously, rotating bowl components have to be machined individually then fitted, aligned and welded together as shown in Fig. 1.6. During development of CE rotating bowl there could be a possibility for the alteration of dimensions of the bowl as the result of weld induced distortion. An induced distortion during welding of this straight bowl causes varying wall thickness along the face of the bowl as well as around the circumference. When these bowls are operated at higher speeds, the tiny local unbalanced masses along the face will result in higher unbalance forces when operating at higher speeds. During rotation at higher speeds, higher unbalance forces push the rotating bowl radially outward and increases the eccentricity between the axes. Further, any irregularities, may lead to deformation of the shell of the bowl and results in shape-change of the bowl. This condition is called as whip or kinetic unbalance. This whip can be corrected by individual correction in every plane wherein imbalance exists, with great care during each and every step in manufacturing. This distortion can be corrected by re-machining of the bowl and the re-machining inside the rotating bowl is seldom in practice. Hence, the CE rotating bowl is assembled by using three C-Seam welds. These joints are to be welded from outside. Tolerances requirements of the finished welded bowl are quite critical. For achieving a smooth and stable operation of CE rotating bowl, overall allowable tolerance on the finished unit shall not exceed the value of ± 0.020 mm. Hence, it is very essential to forecast the distortions in advance in order to minimize the negative effects, so that it helps in improving the performance of the rotating bowl and finally to reduce the manufacturing costs as well.

In different above discussed engineering applications, residual stresses are induced during their manufacturing phase including casting, forging, sheet metal forming, shaping (bending, grinding, machining etc.) and welding. Welding induced residual stresses are produced in a structure as a consequence of local plastic deformations initiated by local temperature history due to rapid heating and subsequent cooling phase. As per the reported literature, both weld residual stresses and distortions can significantly affect the performance and reliability of the components in different hi-tech engineering applications.

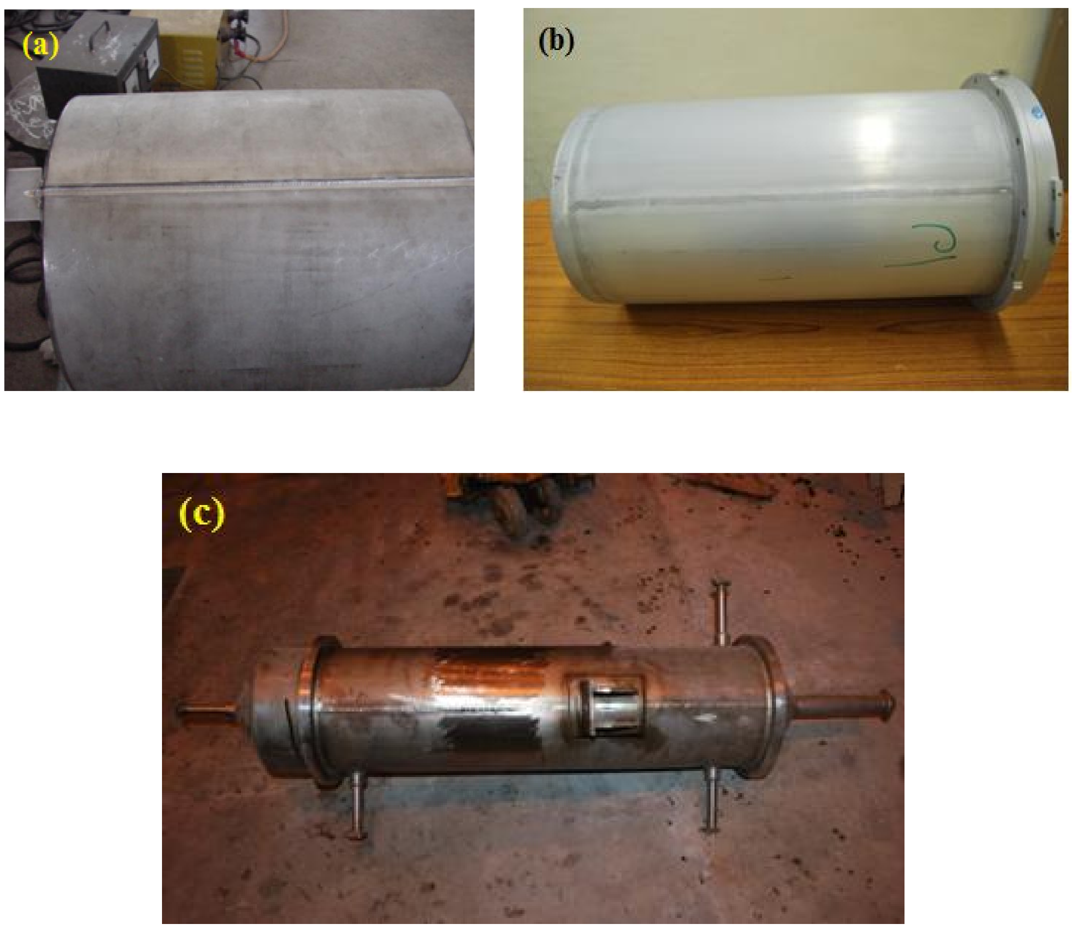

Fig. 1.3 Components with L-Seam weld joints (a) Cylindrical tank (b) High level radioactive waste transfer container and (c) Vent pot.

Fig. 1.4 Containers with both L-Seam and C-Seam weld joints (a) Annular tank and (b) Cylindrical tank.

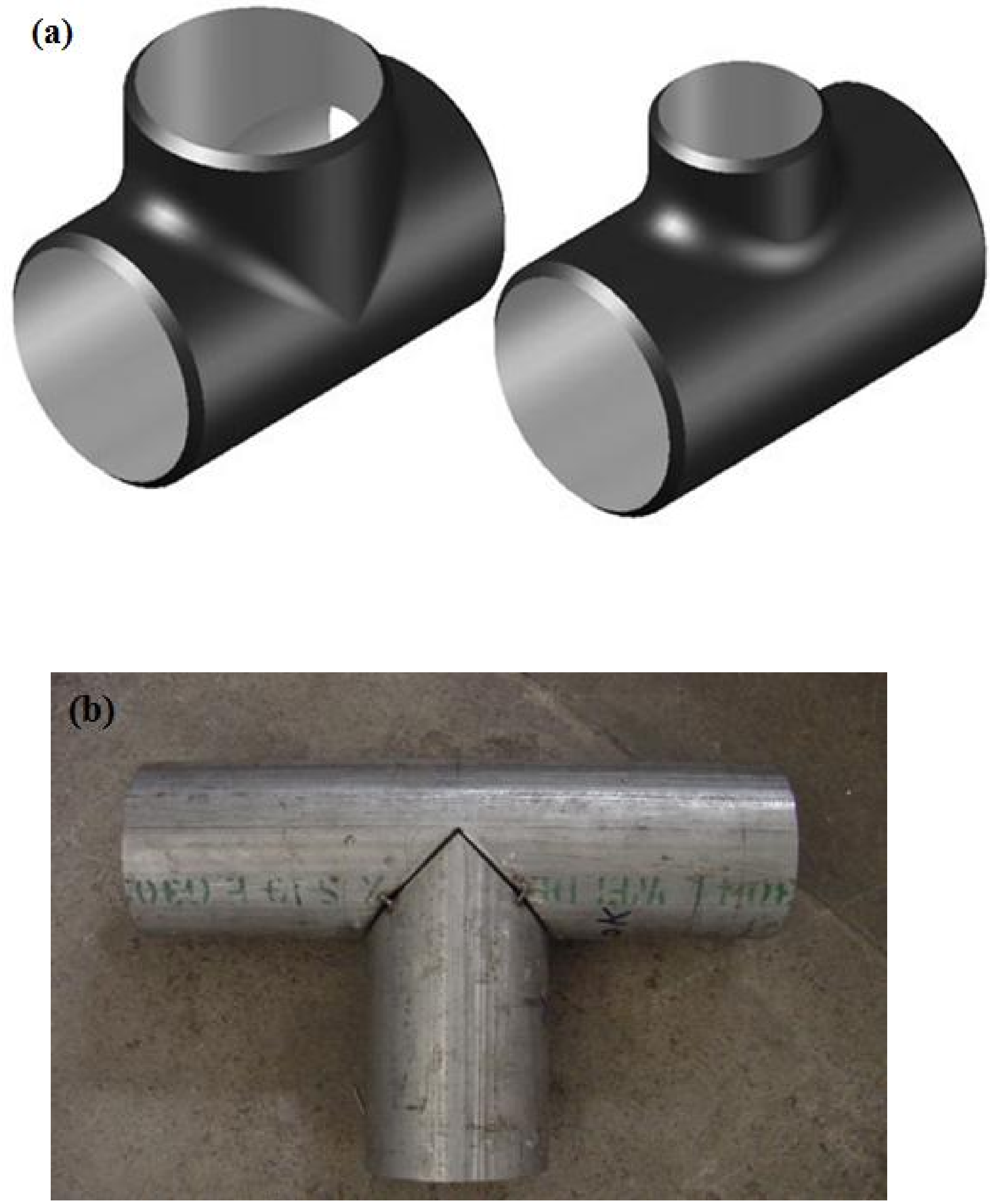

Fig. 1.5 BP-T-joints (a) Cast/forged pipe tee joint and (b) Single N-A butt welded joint.

Contd.

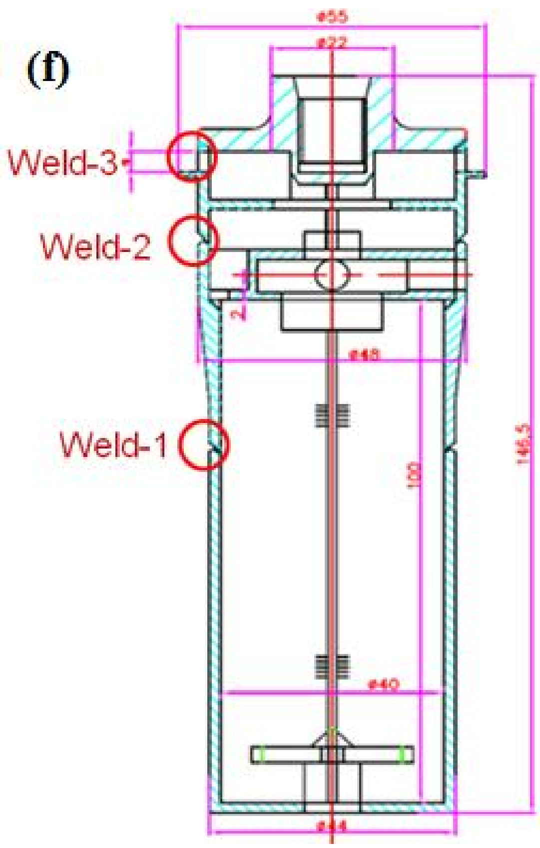

Fig. 1.6 Three plane axisymmetrical C-Seam butt welded CE rotating bowl (a) Assembly (b) Top plate (c) Organic weir (d) Bottom off (e) Baffle plate and (f) Cross sectional view.

1.3. Motivation for this study:

From the previous discussion it is obvious that welding is the extensively utilized permanent joining method in many fabrication industries for different precision engineering applications. On the other hand, welding has number of unfavourable effects on the structural integrity and in-service performance. These unfavourable outcomes which include imperfections induced by the welding process will have effects on the mechanical strengths and possibly may lead to catastrophic failures. One such example is failure of thin-cylindrical shell structure due to L-Seam and C-Seam welds, which is shown in Fig. 1.7. This failure occurs at the junction of L-Seam and C-Seam welds due to weld induced imperfections.

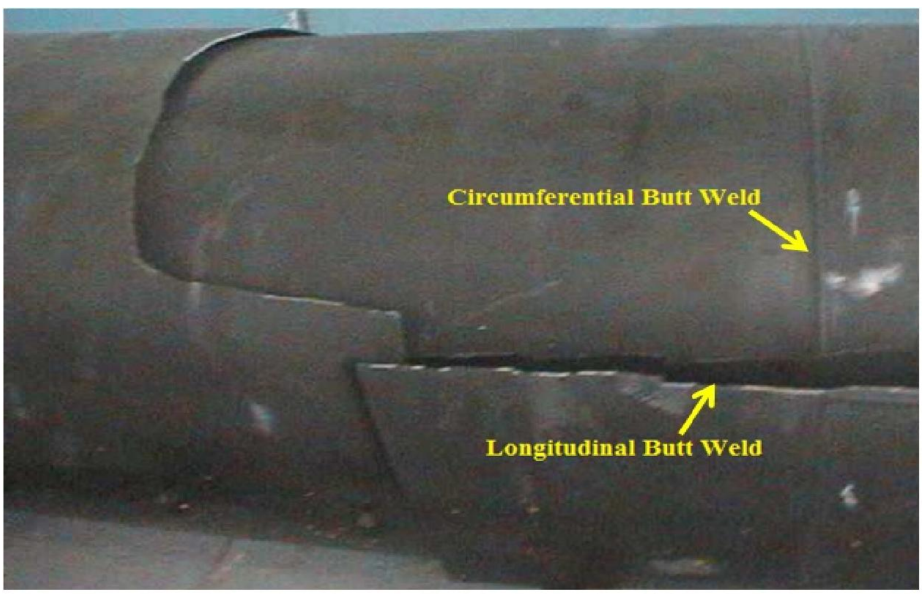

Fig. 1.7 Failure of a component fabricated by both L-Seam and C-Seam butt weld.

In general, tanks and vessels which are subjected to high pressure are preferably fabricated by using C-Seam weld joint considering the effect of high hoop stress compared to longitudinal stress. In majority of the industrial equipments are not subjected to high pressure and high temperature. Hence, these equipment can be fabricated either by L-Seam or C-Seam weld joining process. Also, it is of great interest to use L-Seam welds while fabricating large diameter components in order to reduce production costs. Segle *et al.* [12] found that the cost reduction can be as high as 30% by adopting L-Seam welding.

In addition to this, the single N-A butt weld joint has an important advantage of decrease in weld length compared to the BP-T-joint which is produced by using three C-Seam butt weld joints with the cast/forged pipe tee joint. The decrease in weld length results in cost reduction by 2.5 to 3 times. Moreover, as discussed in Section 1.2 welding plays a major role in fabrication of CE's used in spent fuel reprocessing plants. The material of construction for the CE rotating bowl is solution annealed Austenitic Stainless Steel (ASS) grade 304L with supplementary requirements such as Inter Granular Corrosion test as per ASTM A262 practice C. During fabrication of Stainless Steel (SS) components it is important to note that SS has higher coefficients of thermal expansion and lower coefficients of thermal conductivity than carbon steels. This causes a greater tendency to weld distortion.

During welding process of axisymmetrical L-Seam and C-Seam joints, N-A branch pipe T-joint and three plane C-Seam butt joint of CE rotating bowls generates severe thermal cycles. These thermal cycles produce inhomogeneous plastic deformation which in turn results in high level of residual stresses in the weld metal. In addition to this, significant levels of local stresses occur in the vicinity of weld joints due to internal and external loads. This localized stress due to internal and external loads adds vectorially with the weld induced residual stresses. Therefore, the presence of tensile residual stresses within and near the Weld Zone (WZ) increases the susceptibility to cold cracking, fatigue damage [13], buckling strength, fracture [14] and promotes SCC [15] under certain combination of materials and environment during their service life. Further, the presence of welding distortion has adverse effects on the accuracy of assembly, geometrical tolerances and unbalance mass [16]. Tremendous efforts were made in the past to investigate weld induced imperfections by various authors focusing on different type of weld joint configurations such as L-Seam weld joint of cylinders, J-groove weld joints, T-joint weld plates, plate-to-plate Y-joints, box section T-joints, octagonal pipe-plate joints, penetration nozzle weld joints, spiral welded pipe joints, tube to tube sheet joints, cruciform weld joints, spot welding, axisymmetric models, and layered-to-layered girth welding joint of cylindrical vessels.

It can be observed from the open literature that the comparative study of weld characteristics between L-Seam and C-Seam butt weld joints has not been undertaken to study the effect of variation in temperature distributions and residual stresses on cylindrical components. Literature survey also reveals that comparative study has not been reported on the L-Seam and C-Seam welds of different radius to thickness (r/t) ratios for AISI 304 SS. Further, it concludes that joint configurations will certainly influence both the residual stress distributions and magnitudes. Also, tensile residual stresses in the order of material yield strength are noticed irrespective of the joint type. Hence, failure is also more prone to occur in the N-A: BP-T-joints due to dissimilar geometries of branch and run pipes at the weld vicinity. But, the information on the variation in weld characteristics along the different sections on the Run Pipe (RP) and Branch Pipe (BP) is scanty in the open literature. It is understood that, literature is also not focused on the variations of weld characteristics between RP and BP; outer and inner surface; and for different pipe sizes of BP-T-joints.

Furthermore, very limited literature exists, describing the prediction of residual stresses and weld distortions in three plane axisymmetrical C-Seam butt welding of thin walled cylinders particularly for CE rotating bowls.

Hence, the complex phenomenon in these axisymmetrical and N-A butt welded joints demands immediate attention and focus to ensure the structural integrity of various critical components for improved product quality and reliability. Therefore, in-depth study is attempted to compare the weld temperature characteristics, peak temperature, weld pool (Fusion Zone (FZ) and Heat Affected Zone (HAZ)) shapes and sizes and weld induced residual stresses for the cases of axisymmetrical L-Seam and C-Seam weld joints, N-A butt welded BP-T-joints and for the three plane C-Seam butt joint of CE rotating bowl. The major contribution from this research is to compare the weld characteristics of different axisymmetrical and N-A butt welded joints in order to ensure stringent dimensional tolerances, quality, minimize weld induced imperfections, reduce failure rates, minimizing the wastage and mock-up trails, improving product life and most importantly reduction in welding cost.

1.4. Objectives and scope of this study:

The scope of the present work is butt welding of several cylindrical shell components with an important class of axisymmetrical and N-A joints, primarily focusing on the welding induced residual stresses and deformations. In the present investigation, various welding experiments are performed for different axisymmetrical and N-A butt weld joints in order to validate the developed Finite Element (FE) models for the analysis of complex welding phenomenon. In this study, similar groove geometry, Boundary Conditions (BC), weld sequencing (progressive welding), wall thickness and the constant heat input are used to compare the weld characteristics between L-

Seam and C-Seam butt weld joints of cylindrical components and for the N-A butt welded BP-T-Joints of 50 and 150 Nominal Bore (NB) pipe sizes. Also, comparative study has been performed on the L-Seam and C-Seam welds of different r/t ratios for AISI 304 SS. The importance of weld sequencing and its inference on the three plane axisymmetrical C-Seam butt weld joint of CE rotating bowl is investigated in detail and validated against the experimental results. Further, the scope and major objectives of this study as follows,

i) Several aspects for defining the geometric parameters of Goldak's double ellipsoidal heat source model as implemented in code SYSWELD are studied. Also, different combinations of geometric parameters are characterized on the shape and boundaries of FZ and HAZ. Investigated the effect of variation in geometric parameters of moving heat source model on the thermal and mechanical characteristics in a circumferential butt joining process.

ii) The relationship between moving heat source geometric parameters *versus* weld bead geometry is established, through FE modeling. The assessment of heat source geometric parameters prior to numerical simulation studies can cause reduction in cost and time by avoiding weld experiments.

iii) Obtained some of the important numerical simulation parameters such as voltage and current (power) for the considered weld speed (i.e. energy input), by carrying out Gas Tungsten Arc Welding (GTAW) experiments before FE modeling. Further, macrographs of the weld sections were obtained to confirm the width and depth of penetration for the obtained weld power during experiments.

iv) Heat Source Fitting (HSF) analysis is carried out to define the Gaussian parameters. During this, moving heat source parameters are adjusted such that the simulated molten pool size must match with the cross section of the macrograph. This calibrated heat source is used in Three Dimensional (3D) sequentially coupled thermo-metallurgical-mechanical numerical simulation.

v) Both the hoop and axial residual stress distributions are obtained on the inner and outer surface during L-Seam and C-Seam weld joining process for two different r/t ratios. The influence of L-Seam and C-Seam weld joints on the generation of weld induced imperfections is studied in order to improve the service life of cylindrical components.

vi) 3D temperature profiles, temperature distributions and residual stress states are obtained for different pipe sizes at different sections and locations for the butt welded BP-T-Joints. Meanwhile, in-depth study is performed to compare the significant differences in weld characteristics between run and branch pipes; 50 and 150 NB pipe cases; and along 90^o, 180^o and 270^o sections.

vii) Investigated weld induced residual stress fields, during and after the welding process in a three plane C-Seam butt welded CE rotating bowl by using FE simulation.

1.5. Structure of the thesis:

The thesis is organized in eight chapters and the major contributions in each chapter can be briefly summarized as follows:

Chapter 1 presents introduction to welding induced residual stresses and distortions in a rectangular plate and circumferentially butt welded cylindrical components. Also, it's relevance in different engineering applications are discussed. Based on the importance and detrimental effects offered by welding to the structural integrity, motivation for the present research work and in line with scope and objectives of the research work are established, followed by the brief description of structure of the thesis.

Chapter 2 is an effort to cover literature review on the issues in computational welding mechanics. It includes previous contributions pertaining to moving heat source model, L-Seam and C-Seam butt weld joints of cylindrical components, different N-A weld joint configurations and overview on welding of thin sections. Efforts being made to cover the significant contributions focusing on experimental measurement techniques and prediction of weld induced imperfections in different welded joints along with several techniques are outlined.

Chapter 3 focuses on the guidelines for numerical welding simulation approach and the methodology for FE welding simulations. It presents various governing equations during thermal and mechanical analysis. This chapter also describes thermal and mechanical BC and the temperature dependent thermal and mechanical properties for two different materials used in the present study. Further, it covers calibration of a moving heat source during welding simulation.

The results with significant outcomes from numerical and experimental studies are discussed from chapters 4 to 7.

In chapter 4 several aspects for evaluating the geometric parameters of Goldak's double ellipsoidal heat source model as implemented in code SYSWELD are evaluated. Also, transient temperature distributions, peak temperatures, shape and boundaries of FZ and HAZ for different geometrical conditions of Goldak's heat source model are investigated and compared. This chapter also compares the molten pool sizes obtained by the numerical simulation for different combinations of heat source parameters with the results reported in literature.

Chapter 5 deals with the comparison of weld characteristics between L-Seam and C-Seam butt weld joints of AISI 304 cylindrical components during GTAW process. This chapter provides experimental strategy, welding procedure, analysis of HSF and validation of macrographs with the predicted weld molten pool sizes. Further, the significant differences in residual stress distributions between L-Seam and C-Seam butt joints are presented.

Chapter 6 presents the quantitative characterization of the residual stress distribution in the vicinity of BP weld joint junctions; to assess how such stresses will affect the service life and integrity of components. Simulation strategy for the 3D sequentially coupled analysis discussed in chapter 3 is implemented in this study and the results pertaining to weld temperature characteristics, maximum temperature and weld induced residual stress distributions at different locations and sections for the butt welded BP-T-Joints are presented in detail.

In chapter 7 computational procedure for the evaluation of weld induced residual stresses and distortions for a GTAW welded three-plane axisymmetrical C-Seam butt joint of CE rotating bowl is discussed. The axial and hoop residual stresses on the inner and outer surfaces are computed and their impacts on the CE rotating bowl are also discussed. Further, the distribution of residual stresses during and after the welding process of CE rotating bowl using FE simulation are also presented in this chapter. The importance of weld sequencing and its inference is described in detail.

Finally, in Chapter 8 significant conclusions and the future scope from the present work are presented.

CHAPTER - 02

LITERATURE REVIEW

Welding is the principle activity in modern fabrication industry. The performance of these industries regarding product quality and productivity depends upon structural design, welding technology adopted and control measures on weld induced imperfections implemented during fabrication. Tremendous efforts have been made in the past few decades by various researchers showing a remarkable development in new welding techniques for excellent in-service performance against thermal and structural loading. In spite of these considerable innovations in joining techniques, the problems of weld induced imperfections like distortions and residual stresses are the major challenges for the modern welding engineers. In view of this, lot of research work on the Finite Element Analysis (FEA) of complex welding phenomena has been reported in the literature.

2.1. Previous contributions pertaining to moving heat source model during welding process:

In an arc welding process, a moving heat source is applied at the interface of the two parts to be joined so that they will be connected after liquid metal solidification. The basic idea of the heat source model is the substitute of the physical process with a suitable volumetric heat flux and involves accurate application of heat source parameters during numerical simulation of welding process. The first step towards the simulation of welding process is the modeling of moving heat source. In this regard, Rosenthal [17] did the most important early work on the theory of the effect of moving heat sources in the late of 1930's. The analytical solution derived by

Rosenthal was based on the principle of quasi-stationary thermal state. The quasi-stationary thermal state represents that the origin moves with the heat source, the temperature distribution and the pool geometry do not change with time. In other words, it is a steady thermal response of the weldment with respect to the moving coordinates. He introduced the moving coordinate system to develop solutions for the point and line heat sources and applied this successfully to address a wide range of welding problems. His analytical solutions of the heat flow made possible for the first time for the analysis of the weld process from a consideration of the parameters namely the current, voltage, welding speed, and weld geometry. These analytical solutions can be used to predict temperature distributions at a distance away from the heat source but fail to predict in the near heat source regions.

Further, Eager *et al.* [18] modified Rosenthal's solution to include Gaussian Two Dimensional (2D) surface distributed heat source which can be considered as an arc radius. He found an analytical solution for the temperature distribution when the component subjected to a moving heat source. This solution has become a considerable step for the improvement of temperature prediction in the vicinity of the heat source. Jeong *et al.* [19] introduced an analytical solution for transient temperature distributions of a fillet welded joint. Using this, they have successfully predicted temperature field in the finite thickness plate of a fillet welded joint. Even though they predict temperature fields close to the moving heat source, it was still limited by the shortcoming of the 2D heat source with no effect of penetration. This short coming was overcome by introducing 3D Goldak's [20] double ellipsoid moving heat source.

The double-ellipsoidal heat source model was considered to be the most popular than the single ellipsoidal model, because of its greater flexibility in modeling realistic shapes of a moving heat source [21]. However, the major drawback of this heat source model was the selection of heat source parameters. It should be noted that the dimensions of the heat source are generally not known and there is no link between welding process parameters and dimensions of the heat source. In most cases, the dimensions of the heat source are estimated for initial simulation of a specific welding process and then modified and adjusted based on experimental results.

As per the literature survey, it is apparent that several researchers considered different criteria to define double ellipsoid geometrical parameters for the known bead geometry, welding process and materials during their studies. For instance, Yadaiah *et al.* [21] studied the influence of ratio of rear and front length of double ellipsoidal heat source and found that it has a significant effect on the weld pool dimensions as well as thermal distortion and residual stress of final weld joint. Fachinotti *et al.* [22] considered three different cases, corresponding to different choices of the heat source parameters defining the size and the portion of heat absorbed by the front and rear semi-ellipsoids. In all cases, the fractions of the total heat corresponding to the front and rear semi-ellipsoids are defined as $f_f + f_r = 2$. They observed that, the increase of temperature induced by the source at a given point along the weld path is earlier for the case whose f_f is more than f_r and it is shown in Fig. 2.1 [22]. Guangming Fu *et al.* [23] investigated transient temperature distributions under different geometric parameters of Goldak's heat source model and welding speed. The results demonstrate that they have important effects on the peak temperature and also to the distributions surrounding the welding line. But the temperature distributions in the area which far away from welding line are uniform.

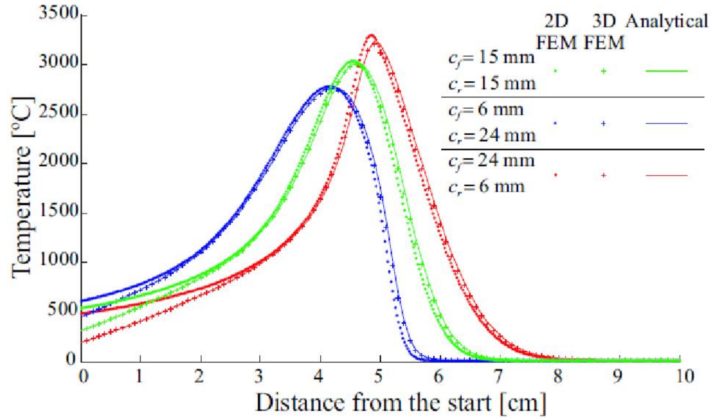

Fig. 2.1 Variation in temperature profiles with the fractions of front and rear semi-ellipsoids [22].

Azar *et al.* [24] established a correlation between analytical and numerical models. The results reveal that the analytical model of a heat source, calibrated using the actual weld bead geometry can be implemented in numerical simulations. Due to this, the time for finding heat source parameters by trial and error can be reduced noticeably and the required parameters can be calculated in a fairly short time by using analytical methods. In this study, FE simulation code was employed to implement the calibrated heat source parameters. Different heat source dimensions were incorporated in the FE model of a finite plate. The contribution of each heat source parameter is shown in Fig. 2.2.

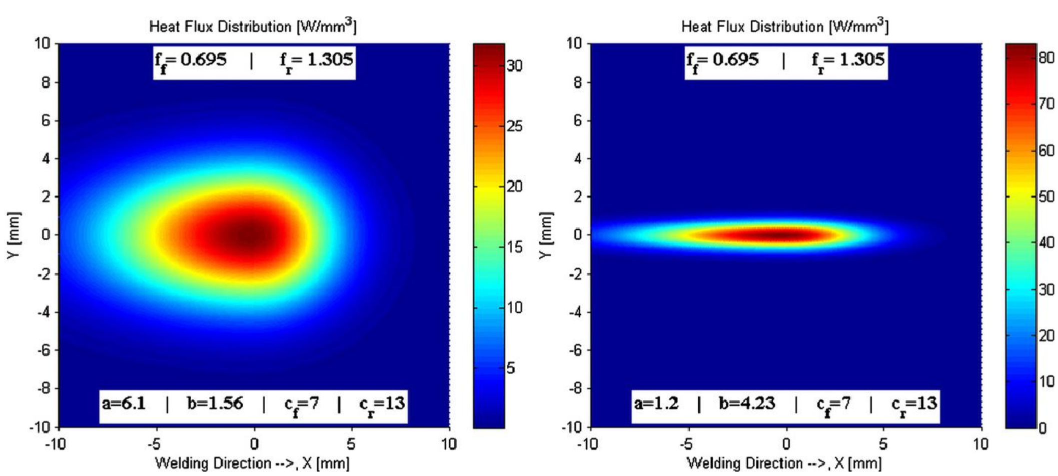

Fig. 2.2 Wide and narrow distributions of a heat source on the top of a plate [24].

Gery *et al.* [25] predicted the welding temperature distributions and variations based on Goldak's moving distributed heat source model. This study revealed that, the FZ and HAZ boundaries are sensitive to the changes of heat source parameters. Variations of the heat source distribution and magnitude affect the shape and boundaries of FZ and HAZ as shown in Fig. 2.3(a). Also, causes change in peak temperatures in FZ and has noticeable effect on temperature distributions in the vicinity of HAZ as shown in Fig. 2.3(b). The results demonstrate that the change in heat source distributions and magnitudes shows a non-linear effect on peak temperatures in FZ and temperature distributions in the areas close to HAZ. Nguyen *et al.* [26] newly derived and reported analytical solutions for the transient temperature field subjected to 3D power density moving heat sources such as semi-ellipsoidal and double ellipsoidal heat sources. The results also depict that the behavior of maximum temperature, heat flux density, shape and size of weld pool for the significance of heat source parameters. Suraj *et al.* [27] presents several aspects of characterization of welding heat source parameters in Goldak's double ellipsoidal model of two overlapping beads. Finally, the Goldak's double ellipsoidal heat source parameters were determined for the welding simulation of overlapping beads. Guang *et al.* [28] obtained the transient temperature distribution and the weld pool sizes by using analytical method. Then, a neural network based algorithm is developed to learn and predict the heat source parameters. Finally, the results of temperature distribution and molten pool size obtained by the numerical method with parameters from Goldak and predicted heat source parameters (by artificial neural network) are verified by the published experimental measurements. The results demonstrate that the developed neural network can accurately predict the heat source parameters and the proposed numerical methodology can obtain the accurate temperature distribution.

(a)

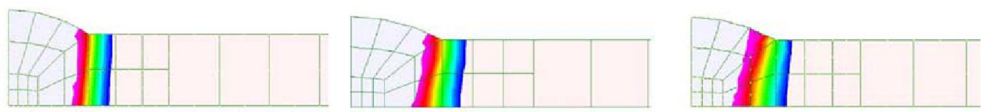

(b)

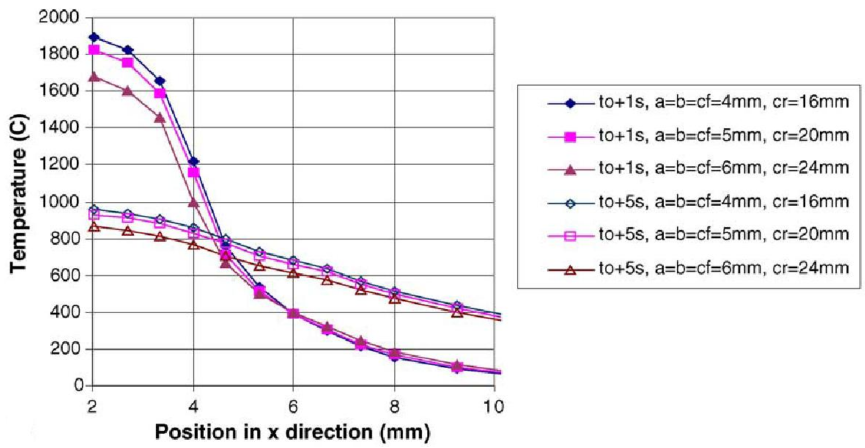

Fig. 2.3 Effect of heat source parameters on (a) FZ and HAZ and (b) Temperature distribution along transverse direction [25].

Behulova *et al.* [29] analyzed and discussed the influence of Goldak's heat source model geometrical parameters on the distribution of internal heat source volumetric density (W/mm^3), temperature history, shape and size of FZ in welded materials. Their study revealed that, the enlargement of geometrical parameters results in decreasing of maximum weld pool temperature, for larger values of heat source width and fractions of front and rear semi-ellipsoids the fusion of weld root does not occur and with increasing heat source depth the maximum weld pool temperature raises, the FZ becomes narrower and deeper.

2.2. L-Seam and C-Seam butt weld joints of cylindrical components:

In nuclear reprocessing plants, some of the important process vessels and equipment such as annular tanks, cylindrical tanks, vent pots, high level waste storage tanks etc.

need to be fabricated either by L-Seam weld joining (or) C-Seam weld joining process. Measurement of transient thermal and mechanical history during welding process is expensive and time consuming. It often fails to provide a complete picture of weld characteristics in the weldment. Therefore, mathematical modeling of temperature and residual stress evaluation provides an effective method in comparison to experimental measurements. Many weld numerical simulations have been performed to understand the residual stress distributions and distortion patterns. A significant research work focusing on longitudinal welding of cylindrical shells is available in literature [12, 30-32]. For instance, Segle *et al.* [12] investigated the life assessment of L-Seam welds based on creep tests with cross weld specimens: further, authors studied the influence of variations in creep properties between the weldment constituents and the size effect of the cross-weld specimen. Maksimovich *et al.* [30] studied the effect of position of heat sources in relation to the weld joint on magnitude of thermal stresses in the WZ. Also, determined optimum heating zones and distribution of heat sources for strengthening of L-Seam weld joints in cylindrical shells. Silva *et al.* [31] investigated the effect of high frequency induction heating on the influence of degradation of mechanical properties of the L-Seam submerged arc welded steel pipe. It was concluded that the tempering temperature during heat treatment process improves the mechanical properties of longitudinal weld joint. Guirao *et al.* [32] carried out 3D FE analyses to evaluate the best welding sequence in longitudinal rib welds of vessel advanced technology segment by electron beam welding through distortion analysis. Based on this analysis, the optimal weld sequence was obtained to minimize welding distortions in the large vaccum vessel components.

Further, several other researchers [33-38] have studied the effect of different types of weld joints, weld configurations, weld process parameters for different material applications of C-Seam weld joining of cylindrical shells towards controlling the weld temperature characteristics, residual stresses etc. For instance, Prokhorenko *et al.* [33] solved the problem to reduce axial residual stresses in a near root region of a C-Seam welded joint of section of steam pipe line by developing a numerical simulation. It was concluded that the increase of static strength for C-Seam weld joint can be achieved by rising number of weld passes from one to three. Barsoum *et al.* [34] found the relation between weld quality and fatigue strength for multi pass welded tubular structures. Results showed that the weld position has a significant effect on quality and fatigue resistance of fillet welds of tubular joint structure. Zhu *et al.* [35] investigated the effects of transverse welds on aluminium alloy stub columns of Square Hollow Sections (SHS) and Circular Hollow Sections (CHS) with respect to section slenderness. Based on this study, softening factors for the HAZ have been proposed for SHS and CHS and compared with their numerical results. Lee *et al.* [36] performed a 3D FE simulation to estimate the residual stresses in C-Seam butt welding of steel pipes with variable r/t ratio ranging from 10 to 100. Also investigated the effects of pipe diameter on residual stresses; and further the differences in residual stress distributions were discussed. Malik *et al.* [37] evaluated the residual stress fields on the inner and outer surfaces of circumferentially arc welded thin-walled cylinders. Their study presented the data to confirm the validity of in-process C-Seam welding technology for thin walled cylinders. Deng *et al.* [38] presented a computational procedure for analyzing temperature fields and residual stresses in multi pass C-Seam welds of SS pipes.

In addition to the above studies, there are numerous investigations [39-46] that pertain to study the effect of different weld sequencing, weld process parameters, BC, heat input, number of weld passes, influence of pipe radius to thickness ratio, effect of weld metal yield stress, dissimilar pipe materials, phase transformation effects, post weld heat treatments, stress distributions near weld Start/End (S/E) location for the C-Seam joining of cylindrical components. As well as, weld temperature characteristics and residual stress distributions are described through numerical analysis with experimental validation. A recent review of literature by Jiang *et al.* [47] revealed the development of weld residual stress and deformation in half pipe jackets and shells. The contours of transverse stress and longitudinal stress are shown in Fig. 2.4 It was concluded that with the increase in heat input from 255 to 455 J/mm residual stress and deformation linearly increasing and in the case of cooling water inside the shell, residual stress and deformation decreasing. Jiang *et al.* [47] results provided a reference for the welding of half pipe jacket and shell.

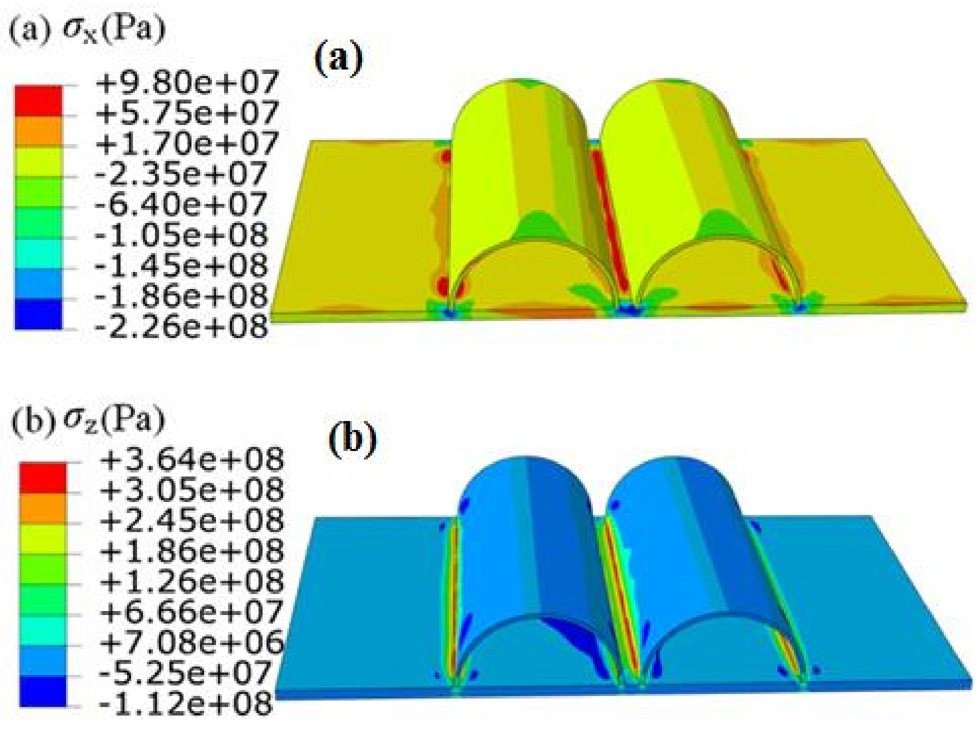

Fig. 2.4 Residual stress contours in a half jacketed pipe: (a) Transverse stress and (b) Longitudinal stress [47].

Michaleris [48] and Blass *et al.* [49] provided some of the perspectives on L-Seam and C-Seam welds. Michaleris [48] computed residual stresses for C-Seam welds in thin and thick walled pipes with variable r/t ratio of single and double-V butt weld joints by using multi pass FE methodology. Further, their analysis performed to evaluate the effects of end restraints and hydro test on L-Seam welds. Author concluded the effect of r/t ratio for single and double-V joints on the axial residual stress distribution for thin and thick walled pipes. In addition to this, author summarised that hydro test influences the axial residual stress in C-Seam welds and has negligible effect in L-Seam welds. Blass *et al.* [49] conducted tensile and torsional tests on tubular specimens with C-Seam and longitudinal weldments of modified 9Cr-1Mo steel. Their results provided much needed confirmation of the reduction factors for creep strength and fatigue life.

It can be observed from the above detailed literature survey that comparative study of weld characteristics between L-Seam and C-Seam butt weld joints has not been undertaken to study the effect of variation in temperature distributions and residual stresses on cylindrical components. Further, literature survey also reveals that comparative study has not been reported on the L-Seam and C-Seam welds of different r/t ratios for AISI 304 SS.

2.3. Different axisymmetrical and N-A weld joint configurations:

Welding induced imperfections within and near the WZ can influence metal shrinkage, dimensional instability, microstructure change, fatigue performance, cold cracking, buckling strength and promotes SCC during their service life. Hence, quantitative characterization of weld induced imperfections in the vicinity of BP weld joint junctions is quite important; to assess how such stresses will affect the service life and integrity of components, and also to understand the mechanism of development on the evolution and distribution of residual stresses.

A review of literature reveals that a significant research work has been undertaken by various authors focusing on different type of weld joint configurations such as L-seam weld joint of cylinders [50], J-groove weld joints [51,52], T-joint welds [53-55], plate-to-plate Y-joints [56], box section T-joints [57,58], octagonal pipe-plate joints [59], penetration nozzle weld joints [60], spiral welded pipe joints [61], tube to tube sheet joints [62], cruciform weld joints [63, 64], spot welding [65], axi-symmetric models [66], and layered-to-layered girth welding joint of cylindrical vessels [67]. It can be observed from the above literature survey that the evaluation of weld characteristics for different type of weld joint configurations were performed using numerical analysis coupled with experimental validation. For instance, Velaga *et al.* [50] compared the weld characteristics between L-Seam and C-Seam butt weld joints of cylindrical components during GTAW process. Their results revealed that there are significant differences in residual stress distributions between L-Seam and C-Seam butt weld joints. Bae *et al.* [51] investigated effects of variables related to 3D FE welding residual stress analyses of J-groove welds in penetration nozzles. Variables such as number of elements and beads in circumferential direction, kinematic BC and circumferential modelling angle in 3D FE models were considered. Based on their analysis, guidelines for 3D FE welding residual stress analysis of penetration nozzles were developed. Deng [52] performed a computational approach to study the influence of deposition sequence based on the final residual stress distribution and deformation in multi-pass J-groove weld joints. The simulation results indicate that the weld sequence significantly affects the residual stresses and to a certain extent on the deformations. Bhatti *et al.* [53] studied the influence of thermo-mechanical material properties of different steel grades on welding residual stresses and angular distortion in T-fillet weld joints. It is concluded that for the investigation of residual stress, except yield stress, all of the thermo-mechanical properties can be considered as constant. For the angular distortion, temperature dependent heat capacity, yield stress and thermal expansion coefficient shall be employed. Fu *et al.* [54] evaluated the welding residual stress and distortion in T-joint welds under various mechanical BC. The results suggest that the transverse residual stress, vertical displacement, angular distortion and transverse shrinkage significantly depend on the mechanical BC and the influence on the longitudinal residual stress is not significant. Oliveira *et al.* [55] performed one-sided laser beam welding of autogenous T-joints. The influence of shielding gas, seam angle and beam focal position was investigated. It is concluded that the weld mechanical behaviour depends on the sheet rolling direction.

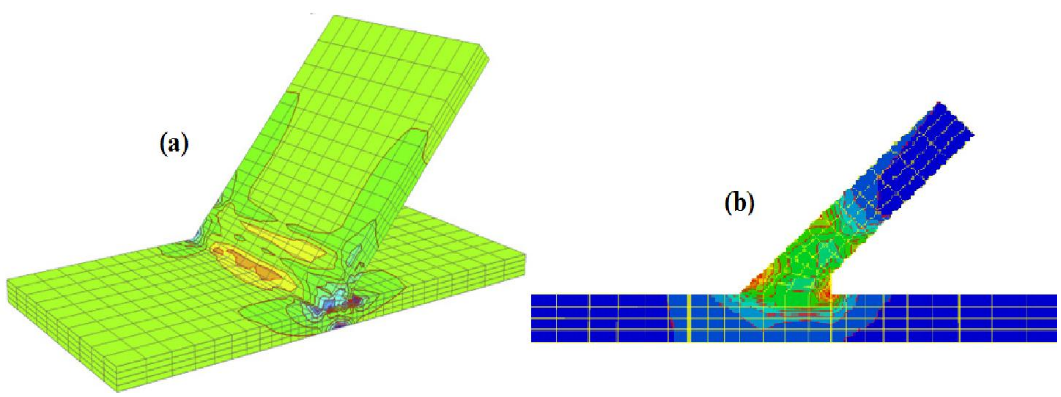

Fig. 2.5 Plate-to-plate Y-joint: (a) Transverse residual stress and (b) Von Mises residual stress at the middle section [56].

Lee *et al.* [56] carried out full 3D sequentially coupled thermo-mechanical modelling procedure for the investigation of residual stresses distributions in plate-to-plate Y-joints fabricated using high strength steel. Figs. 2.5(a) and (b) show the transverse residual stress distribution and Von Mises residual stress distribution respectively in a plate-to-plate Y-joint. Results reveal that the high tensile stress is generated near the weld toe and the weld direction between successive weld passes can affect the maximum residual stress value near the chord weld toe. Lee *et al.* [57, 58] conducted experimental investigation and welding process simulations to estimate the residual stress distributions of the high strength steel box section T-joints. Temperature distribution of box section T-joint from the numerical modeling results is shown in Fig. 2.6. Also, studied the influence of joint angle, weld starting point, the preheating temperature, brace-to-chord width ratio and weld speed on the residual stresses along the chord weld toe of T-joint box sections. FU *et al.* [59] developed a 3D FE approach to investigate the effect of welding sequence on residual stress distribution in a thin-walled octagonal pipe-plate joint. The FE mesh of octagonal pipe-plate joint is shown in Fig. 2.7. The results suggest that a suitable welding sequence can reduce the final residual stress.

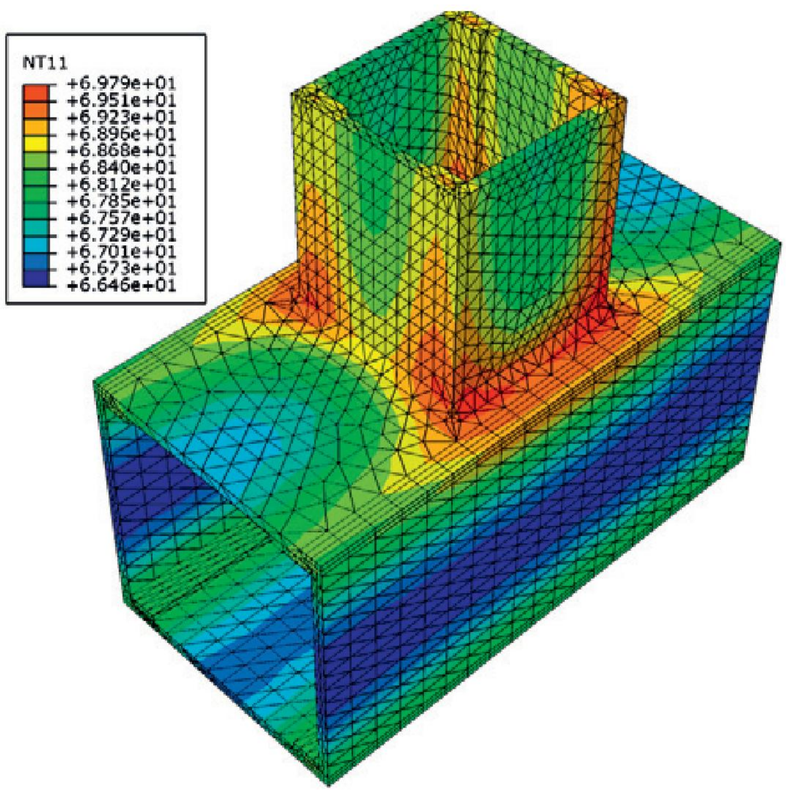

Fig. 2.6 Box section T-joint: Temperature fields in ^{0}C after time (t)=10 mins [57].

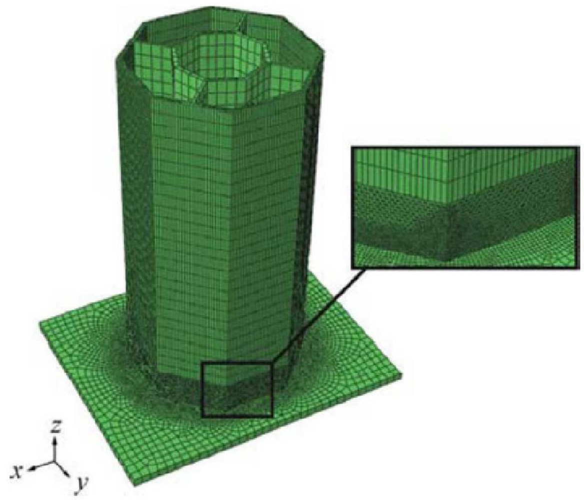

Fig. 2.7 3D FE mesh of octagonal pipe-plate joint [59].

Jiang *et al.* [60] performed a new method which uses overlay welding on the inner surface of penetration nozzle weld joint in order to reduce the residual stresses. It was concluded that with the overlay weld, tensile hoop stress in weld root is decreased about 45% and the radial stress is decreased to compressive stress which helps in decreasing the susceptibility to SCC. Nasim *et al.* [61] investigated the residual stress distributions in a spiral welded pipe. In their study, the distribution of residual stress is calculated using three separate methods: (1) uniform method, (2) power series method and (3) integral method. Also, FE modelling by sequentially coupled thermal and structural analysis of welding was carried out for the estimation of welding residual stresses in a spiral welded pipe. Shugen Xu *et al.* [62] investigated the residual stress in tube to tube sheet joint of a heat exchanger by using numerical simulations. Also, discussed the effect of heat input, preheating temperature and the gap between tube and tube hole on the residual stress distribution. It is concluded that with increase in preheating temperature peak hoop stresses are decreased and with increase in gap between tube and tube hole the residual stresses are increased. Zhao *et al.* [63] studied the residual stress and fatigue behavior of large scale cruciform weld joint with groove. The 3D model of cruciform weld joint and the 2D mapping of the longitudinal residual stress are shown in Figs. 2.8 (a) and (b). The fatigue test results reveal that the fatigue strength of 30 mm thick cruciform welded joint with groove can reach fatigue level of 80 MPa. The stress nephogram indicates that the largest axial residual stress is located at the welding center.

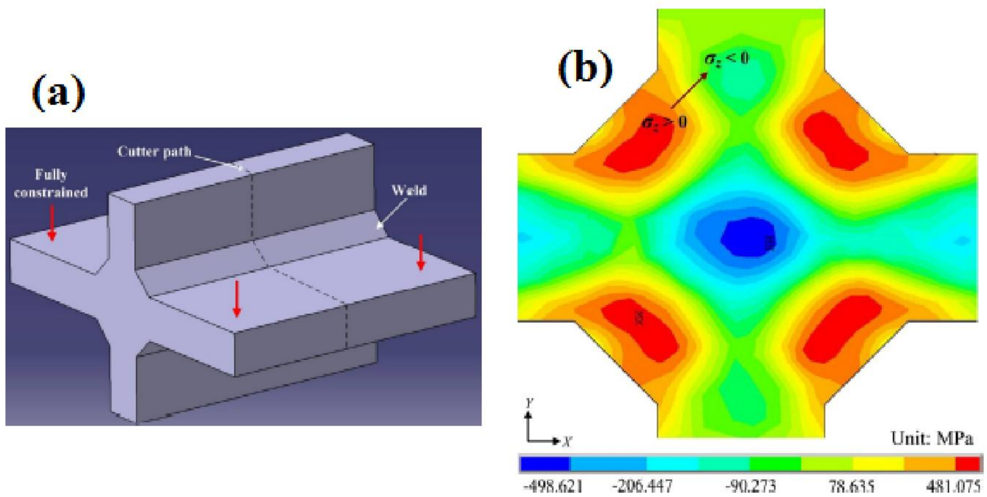

Fig. 2.8 Cruciform weld joint: (a) 3D model and (b) 2D mapping of longitudinal residual stress [63].

Brar *et al.* [64] investigated the residual stresses in HAZ of cruciform welded joint of hollow sectional tubes based on 3D FE simulation of gas metal arc welding process. The temperature distribution in welded cruciform joint is shown in Fig. 2.9. Further, authors altered the welding process parameters in order to reduce the residual stresses to improve weld joint strength. Eshraghi *et al.* [65] computed the effect of resistance spot welding parameters on weld pool properties of DP 600 steel sheets. Authors used design of experiments method to analyze the effects and interactions of the current intensity, welding time, sheet thickness and squeeze force over a realistic range of values. Jie Xu *et al.* [66] compared a 3D pipe and axisymmetric FE model for the same welding simulation parameters. The results indicate that the residual stress distribution for the 3D model and axisymmetric model are same with the equal heat source shape parameters. Shugen Xu *et al.* [67] predicted residual stresses in a layered-to-layered girth welding joint of cylindrical vessels. Their study reveals that large residual stresses are generated in the weld and HAZ. This is due to the material mismatching between inner SS layer and outer low alloy steel layer. Also, it is concluded that the gap between discrete layers has a significant effect on the residual stress in HAZ.

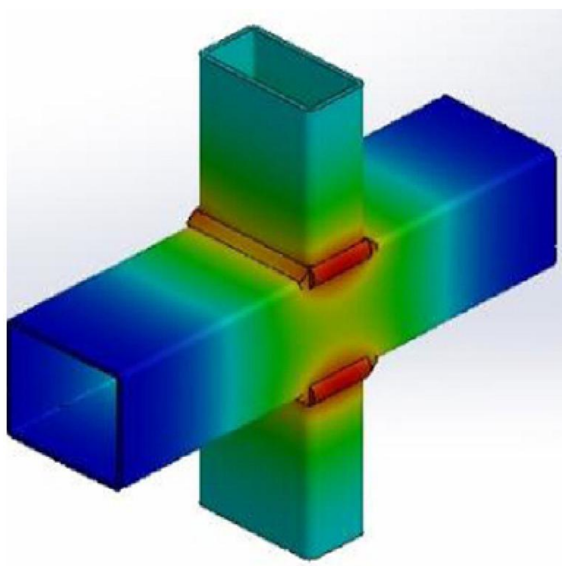

Fig. 2.9 The temperature distribution in welded cruciform joint of hollow sectional tubes [64].

Further, several other investigations [68-71] were performed on the FE based limit load analysis of BP junctions due to combined loading, theoretical stress analysis subjected to external loads transmitted through branch pipes, stress factors effectiveness for reinforced butt-welded branch outlets subjected to internal pressure or external moments and evaluation of flexibility factors for BP connections subjected to in-plane and out-of-plane moments.

2.4. An overview of the literature on welding of thin sections:

During fabrication of thin sections there is a greater tendency to weld induced imperfections. The reliability and high performance of thin-walled cylindrical components are of paramount important in different engineering applications. Further, the welding distortion has negative effects on the accuracy of assembly, geometrical tolerances and unbalance mass [16]. For these reasons, prediction and control of temperature distributions, residual stresses and welding distortions during and after the welding process is very important.

In the past decades, typical numerical analyses with supporting experimental data were established leading to ample fundamental knowledge about weld induced imperfections. For instance, Masubuchi [4] and Connor [72] discussed various types of welding induced distortions, residual stresses in thin walled structures and the control and mitigation techniques. Distortions are considered as the most common defects during welding, which can severely affect the dimensional accuracy and thus lead to expensive corrective work. Hence, it is very essential to forecast the distortions in advance in order to minimize the negative effects, so that it helps in improving the quality of welded parts and finally to reduce the manufacturing cost as well. Liang Wang *et al.* [73] investigated the effect of laser travel velocities with constant power and the laser powers with constant velocity on the distribution of residual stress during laser welding of thin wall plates. In this study, net heat input during welding process was also varied. Spina *et al*. [74] evaluated the effect of welding speeds on the weld profiles and distortion of the components during laser welding of AA 5083 sheets using numerical simulations. This study revealed that as the welding speed reduced the net heat input increased and vice versa. Brickstad *et al*.

[41] numerically simulated a multi-pass C-Seam butt-welding of SS pipes using a non-linear thermo-mechanical FEA to study the variation in weld heat inputs. They also studied the variation in the through-thickness of the weld and HAZ on the axial and hoop stresses for ASS pipe welds and their sensitivity against weld parameters. Kazuo Ogawa *et al*. [75] investigated the residual stress in penetration nozzles by considering different nominal heat inputs and weld speeds at constant weld power for different weld passes. Chaowen Li *et al*. [76] carried out 3D FEA of temperatures and stresses for increasing weld speeds with constant power on different samples. The above study reveals that increase in weld speed at constant power, increases the net heat input. Wu. C.S *et al*. [77,78] used different levels of heat inputs with different welding currents by keeping welding speed and voltage as constant for two different arc welding processes (double sided and plasma) in the numerical simulation. They also carried out numerical analysis to predict the temperature field and weld pool shape as a function of welding speed with constant laser power and current. Díaz *et al*. [79] carried out the comparative analysis on distortion of Tungsten Inert Gas (TIG) welding of austenitic and duplex SS by considering two different net heat inputs for both the stainless steels. Yanhong Tian *et al*. [80] investigated the effect of heat input and welding speed on the temperature field, especially on the shape and dimensions of the weld pool.

Rybicki E.F. *et al*. [81] developed a mathematical model for predicting transient temperature distributions, residual stresses, and residual deflections for pipe girth-butt welds and compared temperature profiles for a two-pass weld. They validated their predicted residual stresses and deflections based on FE representation against individual weld passes, temperature dependent elastic-plastic constitutive behavior with the data obtained from a butt welded 304 SS pipe. Dong. Y., *et al*. [82] has discussed the 3D welding simulation of residual stresses in a girth-welded, with a main emphasis on modeling procedures for the global residual stress distributions. They have suggested the shell element model with a heat source moving along the C-Seam joint, which is cost effective and capable of predicting the global residual stresses. They have also presented the effects of pipe wall thickness and welding speed on residual stresses. Fricke. S. *et al.,* [83] demonstrated a technique that has been developed for numerical simulation of the welding process and validated with the experimental results of ASS pipe welding. They have accounted for the effect of inter-pass cooling which causes sensitization of the HAZ, the effect of gap width on the resultant residual stresses and the effect of the welding of the final passes while simultaneously cooling the inner surface with water producing compressive stresses in the root area of a C-Seam weld in an ASS pipe. Lundback *et al*. [84] have developed a model for weld deposition to describe the material behaviour, strain rate and temperature range in welding. They validated their model with the physical model by measuring temperature and weld deformations. The phase changes for optimizing residual stresses and distortions are the concern of recent Investigators. Teng *et al*. [85] employs the technique of element birth and death to simulate the weld filler variation with time in T-joint fillet welds using thermo-elasto-plastic analysis considering the effects of welding penetration depth, flange thickness and restraint conditions on the weld induced residual stresses and distortions. Shoichi *et al*. [86] develop a method based on the variable length heat sources which is a time-effective computational approach for engineering analysis of multi-pass joints. They analyzed a dissimilar metal with J-groove joint configuration of axisymmetric geometrical shape and discussed the influence of heat source model on welding residual stress and distortion.

It can be observed from the above detailed literature survey that no focused studies had been undertaken to study the prediction of residual stresses and welding distortions in three plane C-Seam butt welding of thin walled cylindrical CE rotating bowls. Further a limited literature is available for the study of influence of weld sequencing on the weld induced residual stresses of CE rotating bowl by numerical simulation.

CHAPTER - 03

METHODOLOGY FOR NUMERICAL WELDING SIMULATIONS

3.1. Introduction:

The analysis of welding process involves different branches of physics, and requires the coupling of several models address to describe the phenomenological behavior of a system. Many of these welding models have been executed numerically and are being used in an efficient way to solve the problems. In an arc welding process, the energy required for melting of metal is produced by the joule effect. This effect generates the energy required for the fusion of both filler and base metals, forming which is known as the weld liquid pool. In the liquid pool, the effects of convection take place that improves the heat transport. Finally, after removing the heat sources, material solidification takes place. During weld process, temperature changes in the metal produce solid state transformations. These transformations originate the changes in material properties [87].

Several numerical approaches are available to provide sufficiently accurate approximations to the solution of complex problems. These different numerical methods are finite difference method, boundary element method, boundary domain integral method, FE method and the finite volume method. All of these methods are applicable for the solution of complex physical problems for which analytical solutions are not readily available. Where, analytical solutions are continuous, given by function of spatial variables and time, whereas the numerical solutions obtained are discrete in nature.

For the last few decades, Finite Element Method (FEM) has been used to simulate the welding process. Some well known references are Ueda *et al.* [88], Marcal [89], Karlsson [90], Goldak *et al.* [91], Radaj [92]. In most of the FE weld simulations, it has been a common practice to assume several simplifications, which can be described as:

1) To solve 2D models, several authors assumed symmetries in the problem. This assumption can be found in the works of Song *et al.* [93] on welded joints, Branza *et al.* [94] on TIG welding for repairing parts, Cho *et al.* [95] in laser welding, Hyde *et al.* [96] for TIG butt welding and Hou *et al.* [97] for spot welding. The motivation of this simplification is the high computational cost of 3D models.

2) With reference to the mechanical description of the weld simulation problem, it has been assumed that materials respond as an in viscid elasto-plastic model in the works of Song *et al.* [93], Hou *et al.* [97], Mochizuki [98] and Mollicone *et al.* [99], with isotropic hardening Branza *et al.* [94], Duranton *et al.* [100], Ferro *et al.* [101], Hyde *et al.* [96] as an elasto-viscoplastic material. Alberg *et al.* [102] compared plastic and visco-plastic models applied to welding simulations, and recommend using a simple plastic model in the initial stages of the weld simulations. However, Fachinotti *et al.* [103] indicated that at high temperature, the viscous effects have a noticeable effect on the behaviour of metals and it cannot be ignored. Also, in general, welding involves heating and cooling cycles whose effect on the mechanical behavior of the material is represented only if kinematic hardening is taken into account [87]. Therefore, the justification of using simple models such as the elasto-plastic without hardening or only with isotropic hardening (the most widely used) is a mere reduction of computational cost.

3.2. FE welding simulation approach:

In this work, for GTAW process simulation, FE modelling program SYSWELD is used on a Dual Intel Xeon E5-2687W @ 3.1 GHz (8 Core, 64 GB RAM, 992GFLOPS) processor PC with a Windows 7 operating system. The methodology and the physical phenomena used in SYSWELD commercial code for different weld process simulations are described in [104]. The methodology for numerical simulations of welding process which is used during this research is described as follows:

Methodology for numerical simulations:

1) ***Step 1***: In order to obtain some of the numerical simulation parameters such as voltage and current (power) for the considered weld speed GTAW experiments were carried out before FE modeling.

2) ***Step 2:*** The macrographs of the weld sections were obtained to confirm the width and depth of penetration for the obtained power during step-1.

3) ***Step 3:*** HSF was carried out to define the Gaussian parameters. During this, heat source parameters were adjusted such that the simulated molten pool size must match with the cross section of the macrograph.

4) ***Step 4:*** Finally, a calibrated heat source is used in thermo-metallurgical-mechanical numerical simulation. The flow chart of the welding simulation procedure used in SYSWELD was described in [105].

The significant capabilities of SYSWELD are as follows: The SYSWELD is a tool for simulation of heat treatment, welding and corresponding welding assembly processes.

It has the capability to consider various aspects such as phase transformations, latent heat effects during phase transformation, changes in microstructure, diffusion and precipitation of chemical elements, hardening behavior (i.e. isotropic, kinematic and mixed), visco-plasticity and phase dependent strain hardening, etc. Temperature dependent material properties, phase proportions; and proportion of chemical composition can be considered. It is also possible to develop a user defined heat source by a volume density of energy which moves along the weld trajectory with a FORTRAN program using graphic user interface. In this work, the numerical simulation procedure was performed in two steps by a sequentially coupled thermo-metallurgical-mechanical analysis. The term 'sequentially coupled' implies that in the first step, temperature histories and phase fractions were computed at each node in a coupled thermo-metallurgical analysis. In the second step, temperature histories and its corresponding phase fractions at each node were employed as the thermal load for subsequent mechanical analysis. The complex nature of weld pool formation is extremely difficult to include each phenomenon occurring within the molten zone. Some of the phenomena like vaporisation, ions formation, molten metal circulation etc. are ignored in this study.

3.3. Governing equations and FE interpretation:

The FE weld simulation analysis is limited to a thermo-metallurgical-mechanical problem by neglecting fluid flow phenomenon in the weld pool, plasma physics, electromagnetism etc, and hence the equilibrium equations left to solve are the heat balance and force equilibria for the thermal and mechanical analysis. These are presented below, with the necessary discretization adopted in the FE code in order to solve it numerically.

3.3.1. Thermal analysis : Temperature distribution:

For the evaluation of transient temperature distributions, principle of law of conservation of energy/first law of thermodynamics is used during thermal modeling; which tells that the addition of volumetric heat conduction and heat generation rate equals to the thermal inertia. In heat transfer analysis, the transient temperature field in time (t) and space (x, y, z) is conducted by solving the governing partial differential equation for the transient heat conduction can be mathematically expressed in its most general form is described in the literature [105]. In this analysis, it is assumed that both the base and weld metals are isotropic materials, so the value of temperature dependent thermal conductivity is same in X, Y and Z directions. During thermal cycle, radiation heat losses dominate in and around the weld pool while the convection losses dominate away from the weld pool. For the evaluation of realistic temperature history, thermal analysis with appropriate BC such as heat loss due to convection and radiation are taken into consideration. These thermal BC are employed for all the free surfaces of the cylindrical component. Their combined effect represented by the general equation is given in [36]. The corresponding FE equations for the thermal analysis are obtained by choosing a form of interpolation function representing the variation of the field variables, namely temperature (T).

3D temperature distribution for an isotropic material is governed by the Fourier law of heat conduction. Together with the heat source from the weld process, the transient governing equation for 3D temperature distribution becomes

$$\rho C \frac{\partial T}{\partial t} = \frac{\partial}{\partial x}\left(K\frac{\partial T}{\partial x}\right) + \frac{\partial}{\partial y}\left(K\frac{\partial T}{\partial y}\right) + \frac{\partial}{\partial z}\left(K\frac{\partial T}{\partial z}\right) + Q \qquad (3.1)$$

Matrix form of the above equations can be written as

$$\rho C \frac{\partial T}{\partial t} = (L)^T(|D|\{L\}T) + Q \tag{3.2}$$

Where, $L=\begin{bmatrix} \frac{\partial}{\partial x} \\ \frac{\partial}{\partial y} \\ \frac{\partial}{\partial z} \end{bmatrix}$ and $D=\begin{bmatrix} K & 0 & 0 \\ 0 & K & 0 \\ 0 & 0 & K \end{bmatrix}$

FE formulation including BC can be written as

$$[C]\{T\}+[K]\{T\}=\{F_E\} \tag{3.3}$$

In the Equation 3.3, [C] represents specific heat matrix, [K] represents thermal conductivity matrix and $\{F_E\}$ represents heat generation and convection matrix.

$[C] =\int_v^{\cdot} C[N][N]\mathrm{T})dv$ Specific heat matrix (3.4)

$[K]=\int_v^{\cdot}([B]^T[D][B])dv + \int_A^{\cdot} hf\ [N][N]^T dA$ Thermal conductivity matrix (3.5)

$\{F_E\}=\int_V^{\cdot} Q[N]dv+\int_A^{\cdot} h_f T_B[N]\ dA$ Heat generation & convection matrix (3.6)

Where:

ρ is the density (kg/m^3),

C is the specific heat (J/kg.K),

K is the conductivity (W/m.K),

h_f is the convective heat transfer coefficient (W/m^2.K),

Q is the rate of internal heat generation per unit volume (W/m^3),

[N] is the matrix of element shape functions,

[B] is the matrix of shape functions derivative, and

{T} is the vector of nodal temperature.

3.3.2. Mechanical analysis:

The temperature distributions obtained by solving the above heat conduction equation from thermal analysis will be further used as input for mechanical analysis in order to obtain stress / strain fields. The mechanical analysis is based on the solution of force equilibrium equations. The FE form of mechanical analysis can be derived using the principle of virtual work; which states that a very small change in internal strain energy/work must be offset by a similar change in external work due to applied load. Mathematically, this can be written as δU = δP. Where, U is internal work, P is external work and δ is the virtual operator. In tensor notation, this can be represented as

$$\sigma_{ij} + P_j = 0 \tag{3.7}$$

Where, σ_{ij} is the stress tensor and P_j is the body force at any point within the volume.

For the FE formulation, the three equilibrium equations are replaced with an equivalent weak form, i.e. the principle of virtual work and it can be expressed as

$$\int_V^{'} \sigma_{ij}\ \mathcal{E}_{ij} dV = \int_V^{'} P_i\ U_i dV + \int_S^{'} T_i\ U_i dS \tag{3.8}$$

Where, δƐ corresponds to virtual strain/deformation, δU is the virtual displacement field and T is the surface traction at any point on the surface (s).

The physical meaning of the virtual work is that the work done by external forces subjected to a virtual displacement is equal to the work done by the equilibrium stresses due to the same virtual displacement.

When solving the above equilibrium equations, small strain theory can be applied during the numerical simulations of welding process. During mechanical analysis, the total strain (ε) in a metal can be defined into several components and it is described with the following governing Equation 3.9.

$$\varepsilon = \varepsilon_e + \varepsilon_p + \varepsilon_{th} + \varepsilon_{tr} + \varepsilon_c \tag{3.9}$$

In Equation 3.9, ε_e, ε_p, ε_{th}, ε_{tr} and ε_c represent elastic, plastic, thermo-metallurgical, phase transformation and creep strains respectively. In numerical simulations of the welding process, the thermal, elastic and some plastic part are always necessary to consider in order to predict weld induced residual stresses and distortions. For high carbon steels, the solid-solid phase transformation has a considerable influence on the mechanical behaviour and the strain induced due to phase transformations shall be considered [52]. For AISI 304L, whose carbon equivalent is less than 0.03%, the strain component due to phase transformation can be ignored [60]. Also, due to short thermal cycles in the welding process, the creep induced strain can also be neglected in the total strain. Hence, in the present study, the strain components due to solid-state phase transformations and creep are neglected in the total strain calculation. The elastic strain component is modelled using isotropic Hook's law with temperature dependent Young's modulus and Poisson's ratio. The plastic behaviour is employed with Von Mises criterion, temperature dependant mechanical properties and isotropic hardening model. To calculate the thermo-metallurgical strain, strains that arise due to temperature dependent thermal expansion coefficient and phase change are included. This strain component (ε_{th}) is given in Equation 3.10:

$$\varepsilon_{th} = \sum f_i \varepsilon_{th_i}(T) \tag{3.10}$$

Where, $\varepsilon_{th_i}(T)$ is the thermo-metallurgical strain corresponding to phase i at temperature T and f_i is the phase proportion of phase i.

3.4. Boundary conditions:

In the welding process, transient temperatures are the source for the development of elastic and plastic strains leading to residual stresses in the welded components. During heating, the heat energy is transported by conduction to the material boundaries. The condition at these material boundaries can be defined in several ways and it is essential for the correct prediction of the temperature distributions in the welded components. Similarly, different mechanical constraints acting on the component during weld heating and cooling of the material, have a significant influence on the weld induced residual stresses and distortions development. The BC which influences the thermal and mechanical analysis is discussed in the following sections.

3.4.1. Thermal boundary conditions:

During thermal cycle, radiation heat losses dominate in and around the weld pool while the convection losses dominate away from the weld pool. For the evaluation of realistic temperature history, thermal analysis with appropriate BC such as heat loss due to convection and radiation are taken into consideration. This thermal boundary condition is employed for all the exposed free surfaces of a FE model. The total heat loss from all heat dissipating surfaces is calculated by Equation 3.11.

$$q_{loss} = q_{convection} + q_{radiation} \tag{3.11}$$

Heat loss from the convective surface according to Newton's law is given by

$$q_{conv} = h_{conv} \cdot (T - T_0) \tag{3.12}$$

Where, h_{conv} is the heat transfer coefficient, T is body temperature and T_0 is the sink temperature. Convective heat loss occurs due to natural convection and forced convection of the surrounding media. Thus, ambient conditions during welding, i.e. wind speed where the structure is welded can have a significant effect and can be taken into account considering the forced convection phenomenon. To determine the convective heat transfer coefficient, several empirical relations have to be considered describing the surrounding media and its behavior is described in [106 and 107].

Another surface effect is the heat loss due to radiation. Radiative heat transfer occurs in the form of electromagnetic waves. In contrast to convective heat transfer the radiative heat transfer is not conditional on the exposed surfaces. On the other side, it is highly depending on the welded work piece material, its surface condition and the direction of radiation. The amount of radiation emitted from the surrounding media can be determined experimentally by using infrared thermography, with respect to the results of a black body [108]. According to Stefan-Boltzmann's law the radiative heat loss is given by the Equation 3.13.

$$q_{rad} = \mathcal{E}^1 . \sigma^1 . (T^4 - T_\infty^4) \tag{3.13}$$

Where, $\mathcal{E}^1$ is the emissivity constant, σ^1 is the Stefan-Boltzmann constant ($5.670*10^{-8}$ W/m^2K^4), T is the body temperature and T_∞ is the surrounding temperature. Form the open literature, some researchers suggest that in addition to both the above heat losses, heat loss due to contact surface plays an important role [109]. Gery *et al.* [25], ignored the contact heat losses. In the present work, most of the mechanical restraints are in point contact or line contact. Therefore, the contact heat losses are neglected in this study.

3.4.2. Mechanical boundary conditions:

If a metallic component is heated uniformly and if it has complete freedom to distort in all directions, it will return to its original form after cooling uniformly. During welding process, heating is not uniform. The heat is concentrated at the joint, with the arc temperature being very much higher than the base metal. Due to this uneven expansion and contraction between the weld metal and base metal, stresses generate at the welded joint. These stresses are greatly influenced by different factors such as external constraint, material thickness, type of weld process etc. As the amount of external constraint increases, magnitude of internal stresses will increase. If no external constraint is applied during welding, the stresses will cause the component to distort very freely. It can be concluded that the constraint is a measure of structure's ability to develop residual stresses and diminish distortions. In this study, to match the experimental BC, minimum clamping was applied as the artificial boundary condition in order to prevent rigid body motion in the numerical simulation. The detailed BC used during FE simulations are discussed in the Sections 5.2.2, 6.3 and 7.1.

3.5. Material modeling:

During simulation, the material properties for both base and weld metal were assumed to have the same mechanical and thermal properties. The material properties, for instance, the thermal conductivity, specific heat, modulus of elasticity and yield stress, vary with the change in temperature. The average values can be used in calculations if the temperature does not vary too much. But during the welding process, the temperature of the weldment changes very shapely. In this case, neglecting temperature dependent material properties result in big deviations. Consequently, temperature dependent thermal and mechanical properties are the most important aspect for the accuracy of computational weld mechanics. In the past, numerous efforts have been made for the investigations of material properties at elevated temperatures and the subsequent effects on the thermal-structural response under different transient loading conditions.

In the present research work two different materials such as AISI 304 and AISI 304L are considered. The FE heat transfer analysis for welding simulation requires precise values of thermo-physical properties. Thermo-physical properties that are taken into account include thermal conductivity, specific heat capacity and density. Heat transfer by conduction involves energy transfer with in a material. The heat transfer rate depends on the temperature gradient and material thermal conductivity. The heat capacity of a material is a measure of how the component stores heat. The density of a material must be required in the thermal analysis to calculate the amount of heat storage in the material. This property is also included directly in the specification of heat capacity as a combined property.

Similarly, the three most important thermo-mechanical properties such as Young's modulus, thermal expansion coefficient and yield stress are used during mechanical analysis. According to hook's law the stress is proportional to strain within the elastic region i.e. prior to material yielding. The ratio of the stress and strain in an uni-axial test is young's modulus and it indicates the material elasticity. A body normally expands with the increase in temperature and contracts when temperature decreases. This behavior is known as thermal dilation and the proportionality factor between strain and temperature is called as thermal expansion coefficient. The yield stress is an expression of the stress necessary to produce plastic deformation in a material. The level at which yielding happens is strongly dependent on the temperature. As the temperature increases material softens and the yield strength reduces.

Also, the temperature independent material properties and constants for the ASS, such as convective heat transfer coefficient, Stefan-Boltzmann constant, emissivity and Poisson's ratio considered in the present investigation. For this analysis, isotropic hardening model with linear strain hardening behavior is considered. Various welding numerical simulation studies [51, 52, 61] have been performed over a period of time, which assumed isotropic hardening behavior.

3.5.1. Material model for AISI 304:

The above described material properties for AISI 304 are taken from Ravisankar *et al.* [110] and the temperature dependent thermo-physical and thermo-mechanical properties are shown in Figs. 3.1 and 3.2 respectively. The temperature independent material properties and constants such as convective heat transfer coefficient, Stefan-Boltzmann constant, emissivity and Poisson's ratio considered in the present investigation are listed in Table 3.1 [110]. In the analysis, latent heat is accounted for defining the enthalpy (H) and it is represented by the Equation 3.14.

$$H = \int \rho . C_p . dT \qquad (3.14)$$

At higher temperature, metal expands and resulting low density. Therefore, temperature dependent density is used in this study and it is shown in Fig. 3.1. During welding process, change in state occurs in between solidus and liquidus temperatures. For this analysis, the material solidus and liquidus temperatures were considered as 1360^0C and 1450^0C respectively. The latent heat of fusion was taken as 260 KJ/kg, to include the thermal effects due to solidification of the weld pool.

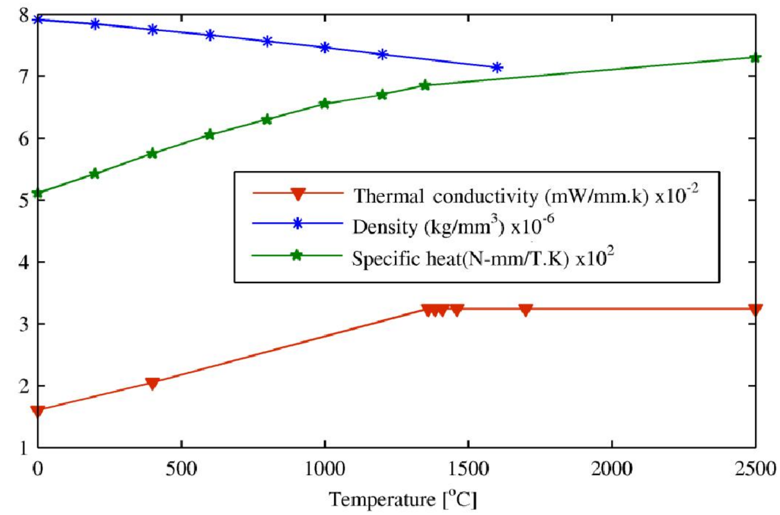

Fig. 3.1 Temperature dependent thermo-physical properties.

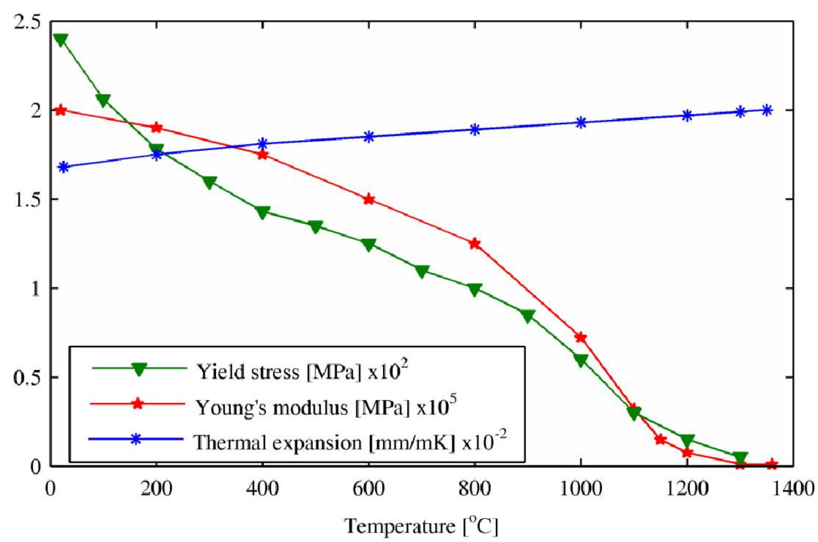

Fig. 3.2 Temperature dependent thermo-mechanical properties.

Table 3.1 Temperature independent material properties and constants.

Property	Value
Convection heat transfer coefficient	25 W/m^2K
Stefan-Boltzmann constant	$5.670*10^{-8}$ W/m^2K^4
Emissivity	0.8
Poisson's ratio	0.33

3.5.2. Material model for AISI 304L:

The temperature dependent thermo-physical properties that are taken into account include thermal conductivity, specific heat capacity and density; and temperature dependent thermo-mechanical properties such as Young's modulus, thermal expansion coefficient and yield stress are used during thermal and mechanical analysis respectively. The temperature dependent thermal and mechanical properties are shown in Figs. 3.3 and 3.4 respectively and these properties are adopted from Zhu and Chao [111], Mir Zahedul *et al.* [112] and SYSWELD reference manual and material [113]. The chemical composition of AISI 304L material is listed in Table 3.2. Material solidus and liquidus temperatures are considered as 1360^{o}C and 1450^{o}C respectively [113]. The latent heat of fusion is taken as 274 KJ/kg [111] to include the thermal effects during phase transformations of the weld molten metal. The temperature independent material properties and constants for the ASS i.e. AISI 304L, such as Poisson's ratio, convective heat transfer coefficient, Stefan–Boltzmann constant and emissivity, which are used in this study are similar to the properties of AISI 304, and these are specified in Table 3.1.

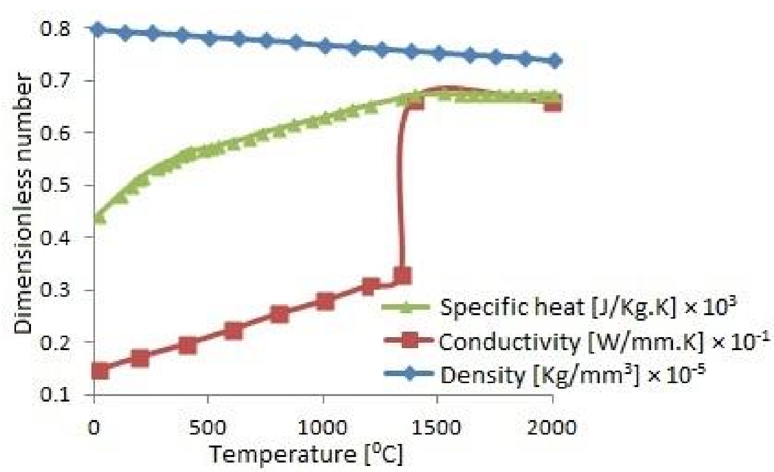

Fig. 3.3 Temperature dependent thermo-physical properties.

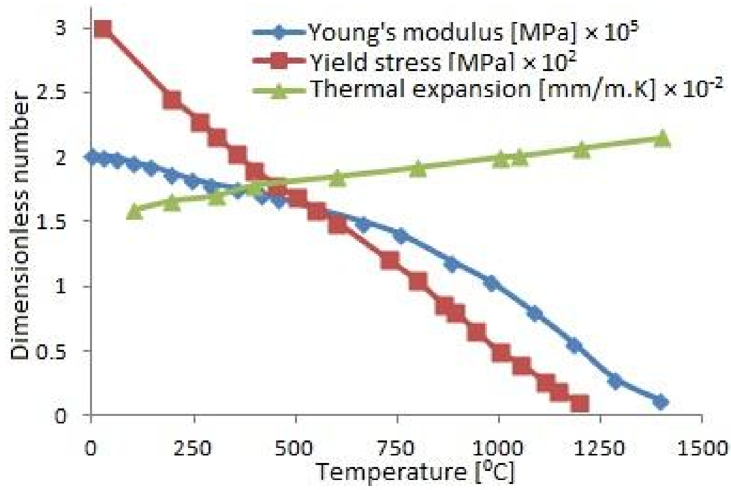

Fig. 3.4 Temperature dependent thermo-mechanical properties.

Table 3.2 Chemical composition (in Wt %) of AISI 304L.

C	Cr	Mn	Ni	Si	S	P	Fe
0.02	17-19	1.1-1.3	9-10.4	<= 1	<= 0.03	<= 0.045	Bal.

3.6. Moving heat source calibration:

For the welding processes with limited penetration, a Gaussian heat flux source on the surface of the weld pool is a solution as suggested by Pavelic *et al.* [114]. With the heat flux prescribed on the surface, the weld pool shape will be approximately spherical because the total heat input is transported by diffusion. But during practical weld applications heat is transported in a different way. The difference is that with diffusion, heat flows equally in all directions whereas for real welds more amount of heat flows to downstream. The physical phenomena of the weld pool formation and the directions of heat and mass transfer are shown in Fig. 3.5 [115]. As shown in Fig. 3.5, the buoyancy force and electromagnetic force contribute to the convection in the weld pool with the arc pressure and volume expansion. These effects together with the heat transfer mechanisms are represented by Pavlyk *et al.* [115]. As a result of this physical phenomena acting on the weld pool, the convective flow in the welding leads to narrower and deeper weld pools than the spherical approximation attained by a pure diffusion model. In the case of penetrated fusion welds, a semi double ellipsoidal model can be used.

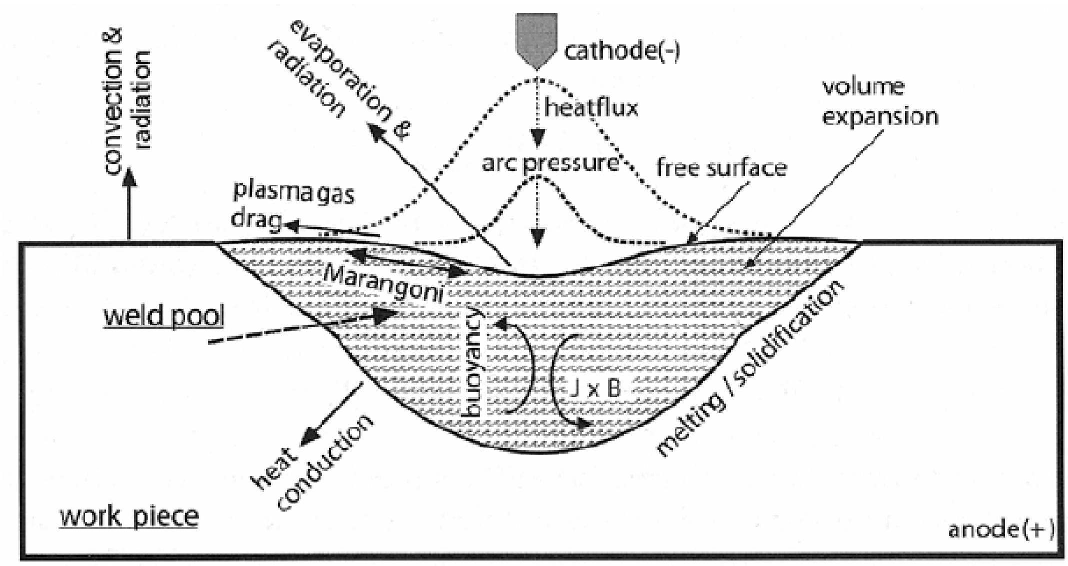

Fig. 3.5 Physical phenomena of weld pool formation: heat and fluid flow in the weld pool Pavlyk *et al.* [115].

In GTAW process, a moving heat source is applied at the interface of the two parts to be joined so that they will be connected after liquid metal solidification. Numerical simulation of welding process is a complex phenomenon and involves accurate application of heat source parameters. The basic idea of the heat source model is the substitute of the physical process with an appropriate volumetric heat flux. The double-ellipsoidal heat source model is considered to be the most popular than the single ellipsoidal model, because of its greater flexibility in modeling realistic shapes of a moving heat source [21]. The most appropriate model for the heat source of GTAW process is the double ellipsoidal heat source. In this study, Goldak's double ellipsoidal heat source model [20] is adopted to present the heat generated by the weld torch and is shown in Fig. 3.6. The variations due to curvature of the circular component are not taken into account.

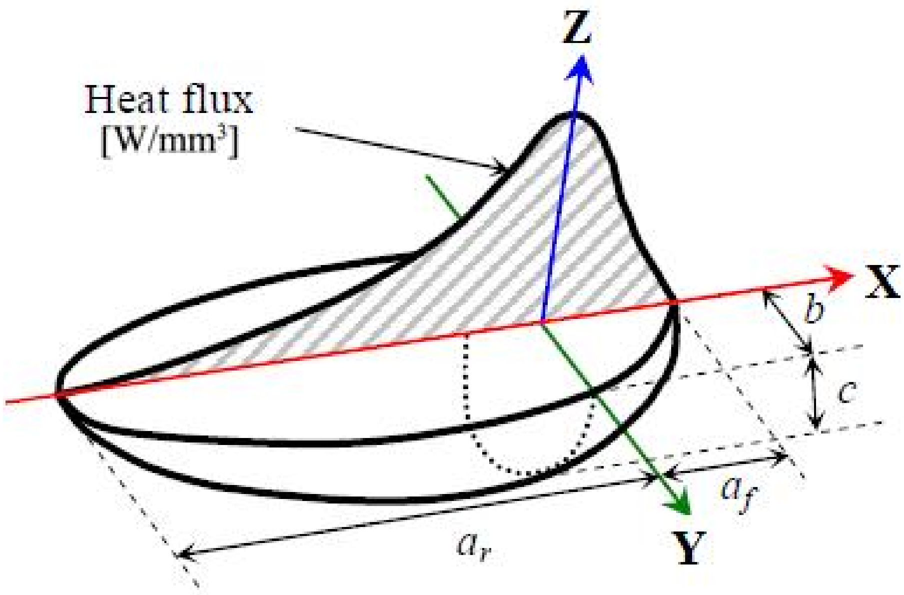

Fig. 3.6 Double ellipsoid heat source model.

The power densities of the double-ellipsoid heat source, q_f (x, y, z) and q_r (x, y, z), which describe the heat flux distributions in the front and rear quadrant respectively are defined with the governing Equations 3.15 and 3.16 [20]:

$$q_f(x,y,z) = \frac{6\sqrt{3}f_fQ}{a_f bc\pi\sqrt{\pi}} \cdot e^{-\frac{3x^2}{a_f^2}} \cdot e^{-\frac{3y^2}{b^2}} \cdot e^{-\frac{3z^2}{c^2}} \tag{3.15}$$

$$q_r(x,y,z) = \frac{6\sqrt{3}f_rQ}{a_r bc\pi\sqrt{\pi}} \cdot e^{-\frac{3x^2}{a_r^2}} \cdot e^{-\frac{3y^2}{b^2}} \cdot e^{-\frac{3z^2}{c^2}} \tag{3.16}$$

Where Q=I×V×η is the energy input rate which is determined by the product of welding current (I), Voltage (V) and weld efficiency (η). f_f and f_r are the fractional factors of the heat deposited in the front and rear quadrant, which can be determined by $f_f + f_r = 2$ [20]. The front and rear fractions of the heat source f_f and f_r were considered as 0.4 and 1.6 respectively. As shown in Fig. 3.7, the constants a_f, a_r, b and c are the double ellipsoidal heat source parameters that define size and shape of the ellipses therefore the heat source distribution. A double ellipsoidal heat source axes and parameters implemented in SYSWELD are shown in Fig. 3.7.

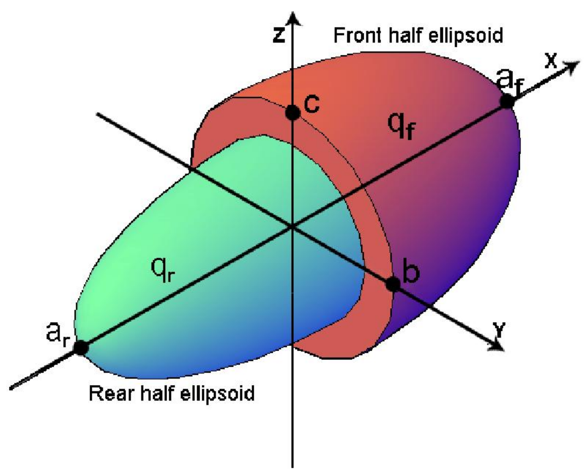

Fig. 3.7 Axes and parameters as implemented in SYSWELD.

CHAPTER - 04

CHARACTERIZATION OF HEAT SOURCE PARAMETERS

Double-ellipsoidal volumetric source with Gaussian heat distribution is one of the most popular heat source model used for different fusion welding process simulations. In order to accurately simulate the detailed aspects of welding process, it is important to implement the correct size and distribution of the heat source. It is a common practice that the dimensions of a heat source model are decided based on experimentally observed weld craters and pool sizes. But the major difficulty is to accurately measure the experimental weld pool sizes to obtain the dimensions of a moving heat source model before starting weld simulation. Any slight variation in the geometrical parameters of Goldak's heat source model may affect the weld thermal, mechanical characteristics and the shape and boundaries of FZ and HAZ.

Also, the major drawback of this heat source model is the selection of heat source parameters. It should be noted that the dimensions of the heat source are generally not known and there is no link between welding process parameters and dimensions of the heat source. In most cases, the dimensions of the heat source are estimated for initial simulation of a specific welding process and then modified and adjusted based on experimental results [29]. As per the literature survey, it is apparent that several researchers considered different criteria to define double ellipsoidal moving heat source geometric parameters for different cases of bead geometries, welding process and materials during their investigations.

It can be observed from the detailed literature survey that the benchmark studies have not been performed to obtain dimensions of the moving heat source geometric parameters. Also, it should be noted that the characterization of moving heat source geometric parameters has not been commenced to study the effect of variation in both the temperature distributions and residual stresses on cylindrical components. Further, literature review also reveals that no studies have been reported on the variation in axial, hoop and radial residual stress distributions for different cases of moving heat source geometric parameters on the inner and outer surfaces of AISI 304 stainless steel (SS).

In this study, several aspects for evaluating the geometric parameters of Goldak's double ellipsoidal heat source model as implemented in code SYSWELD are evaluated. A 3D FE model is developed in order to implement a moving heat source into FE simulation for butt joint of AISI 304 SS cylindrical component. Sixteen different double ellipsoidal volumes are defined corresponding to the front, rear, bead width and depth of the moving source.

The transient temperature distributions, peak temperatures, shape and boundaries of FZ and HAZ for different geometrical conditions of Goldak's heat source model are investigated and compared. The molten pool size obtained by the numerical simulation for different combinations of heat source parameters are also compared with the results reported in literature. The constants a_f, a_r, b and c as shown in Figs. 3.6 and 3.7 are the double ellipsoidal heat source parameters that define size and shape of the ellipses therefore the heat source distribution.

4.1. Numerical simulation for the thermal and mechanical analysis:

While determining the influence of heat source parameters in thermal analysis of GTAW process, it was imperative to consider the variation of thermo-physical properties of AISI 304 material with temperature. Thermo-physical properties such as thermal conductivity, specific heat capacity and density were considered in the present study. The various properties of AISI 304 for the numerical simulation were described in the Section 3.5.1.

4.1.1. FE modeling:

The characterization of moving double ellipsoid heat source parameters and the evolution of thermal cycles were investigated by means of FE method using SYSWELD. In order to predict the influence of Goldak's double ellipsoid geometrical parameters on the shape and size of FZ and HAZ, to compute the distribution of volumetric heat flux density and to make accurate estimation of temperature distributions, a full 3D model was developed by revolution of a 2D mesh. The details and dimensions of the components for simulation model were given in Fig. 4.1 and the details of 2D mesh and 3D mesh with BC were shown in Figs. 4.2 (a) and (b).

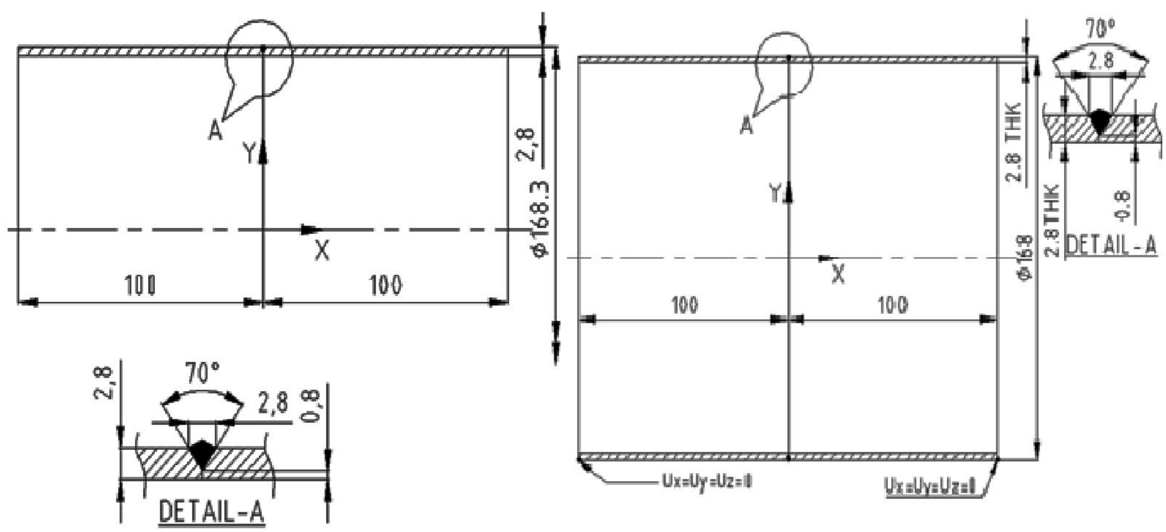

Fig. 4.1 Schematic 2D line diagram.

The element type was Quard, 3D solid with three translational degrees of freedom at each node. In radial direction the element size adjacent to V- groove was 0.5 mm and below the V- groove was 0.4 mm. In longitudinal direction, the element size within and adjacent to HAZ was kept constant equal to 0.5 mm and at longitudinally away from HAZ, it was kept constant equal to 1 mm. In circumferential direction, the element size was also kept constant (i.e. 1 mm uniformly).

During thermal analysis, the thermal BC such as radiation and convective heat losses were employed for all free boundaries of the cylindrical component. To consider the heat transfer due to fluid flow in the weld pool, a temperature dependent thermal conductivity was used. The solidification of the weld pool was modeled by taking into account the latent heat of fusion. The ambient temperature was assumed to be 25^0C.

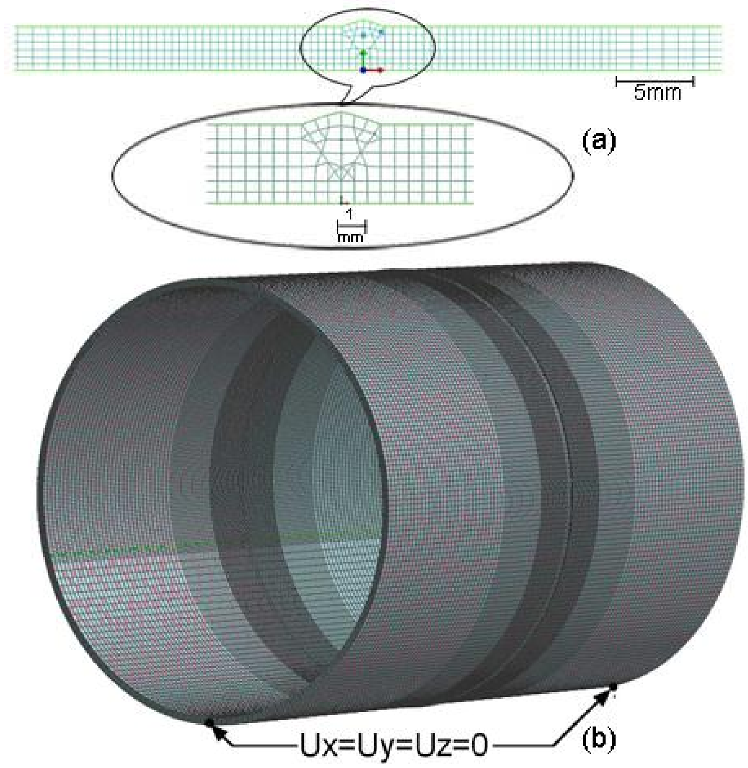

Fig. 4.2 (a) 2D mesh and (b) 3D mesh with boundary conditions.

4.2. Results and discussions:

In the present numerical analysis, GTAW circumferential butt welding was carried out on 2.8 mm wall thick cylindrical component. In this investigation, the welding process parameters such as weld speed and power are considered as 1 mm/s and 375 watts respectively; for the characterization of heat source parameters and to evaluate temperature and residual stress distributions.

4.2.1. Experimental verification of the FE model:

For experimental validation of predicted temperatures, single-V groove butt joint configuration, single pass GTAW process and AISI 304 SS as base material are considered. The filler material is SS 308 having diameter of 1.6 mm and argon is used as shielding gas. Welding experiments are carried out on 2.77 mm thick × 168.3 mm outer diameter cylindrical sections which are equivalent to 150 NB-SCH 5 standard pipe dimensions. Two cylindrical components each of 100 mm length are initially tack welded at different circumferential locations. The experimental weld setup with data logging system is shown in Fig. 4.3. For the welding experiments, 54 A current, 10 V voltage and weld speed of 1 mm/s are considered. The above mentioned weld process parameters with a GTAW process arc efficiency give the heat input per unit length is 375 J/mm; which is equal to the heat input that is used in FE simulation. Transient temperatures are measured using Chromel-Alumel (K-type) thermocouples connected on the outer surface by silver brazing and the temperatures are recorded for every second interval. For this validation, total ten numbers of thermocouples are connected at 90^{o}, 180^{o} and 270^{o} planes from the weld start position. The temperature distributions from FE simulation are validated with the experimental measurements and their correlation is shown in Fig. 4.4. The locations 10 and 20 mm away from the weld centre (WC) line are considered along the axial direction. From Fig. 4.4, it can be noticed that the experimental and the predicted FE results are reasonably comparable.

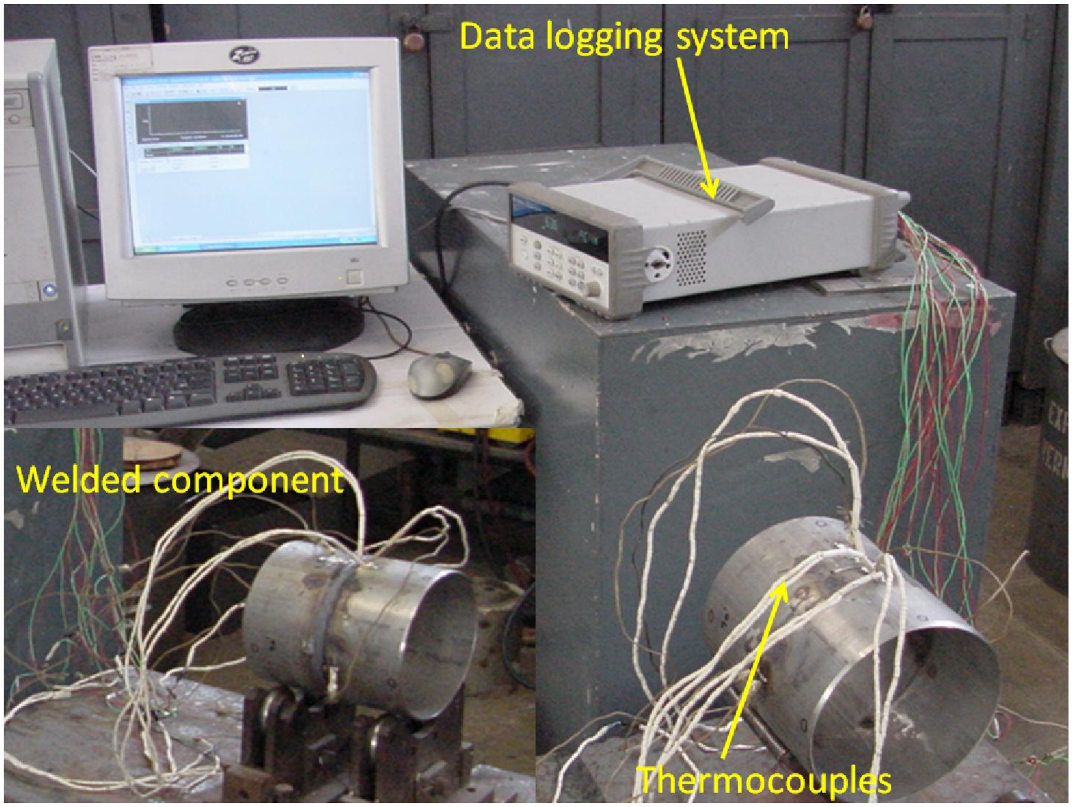

Fig. 4.3 Experimental weld setup with data logging system.

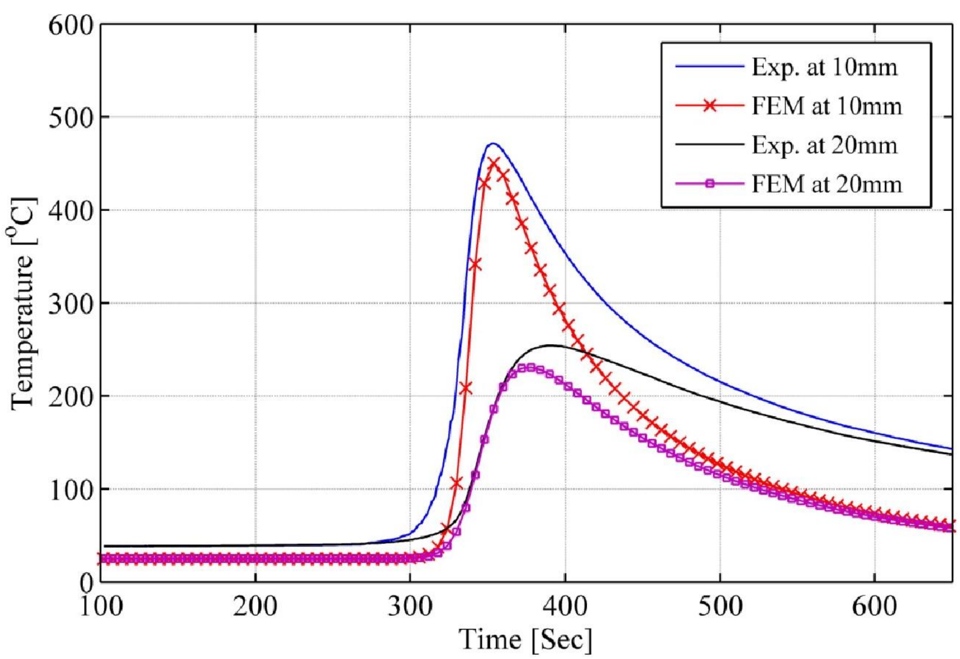

Fig. 4.4 Experimental validation of predicted and measured transient temperatures.

4.2.2. Characterization of the heat source parameters:

This section would give us a better understanding of effect of moving heat source geometric parameters on FZ shape and sizes. The four important geometric parameters explained in Equations 3.15 and 3.16 (a_f, a_r, b and c) define the front ellipsoid length, rear ellipsoid length, half width and depth of penetration of double ellipsoid heat source model. Sixteen different cases of double ellipsoid parameters are considered to study the importance of each parameter. Figs. 4.5 and 4.6 describe details of variations of the FZ shape and size, temperature profile on the outer surface and volumetric heat flux distribution for the considered heat input i.e. 375 J/mm. The evaluated front (q_f) and rear (q_r) heat flux densities (W/mm^3) according to Equations 3.15 and 3.16 are also represented in Figs. 4.5 and 4.6. The Figs. 4.5(II) and 4.6(II) show the sharp thermal gradients in front of the heat source. The gradients behind the weld torch indicate the cooling phenomenon after peak temperature is attained. Also, the elliptical temperature profiles are noticed on the component outer surface. Figs. 4.5 and 4.6 demonstrate that the ratio of q_f and q_r is always in the ratio of front (f_f) and rear (f_r) fractions. It is discerned to note that the maximum temperature (T_{max}) is different for all the sixteen different cases. Also, high value of geometric parameters a_f, a_r, b and c promotes to reduce the heat flux densities (q_f and q_r) and the peak temperature (T_{max}); that ultimately causes reduction in weld pool dimensions and vice-versa is observed in Figs. 4.5 and 4.6. Each case represented in Figs. 4.5 and 4.6 has its own significance.

For instance, cases 1, 2 and 3 in Fig. 4.5, illustrate that if a_f is greater than half width (i.e. b) and a_r is equal to a_f then the FZ is wider throughout the depth of penetration.

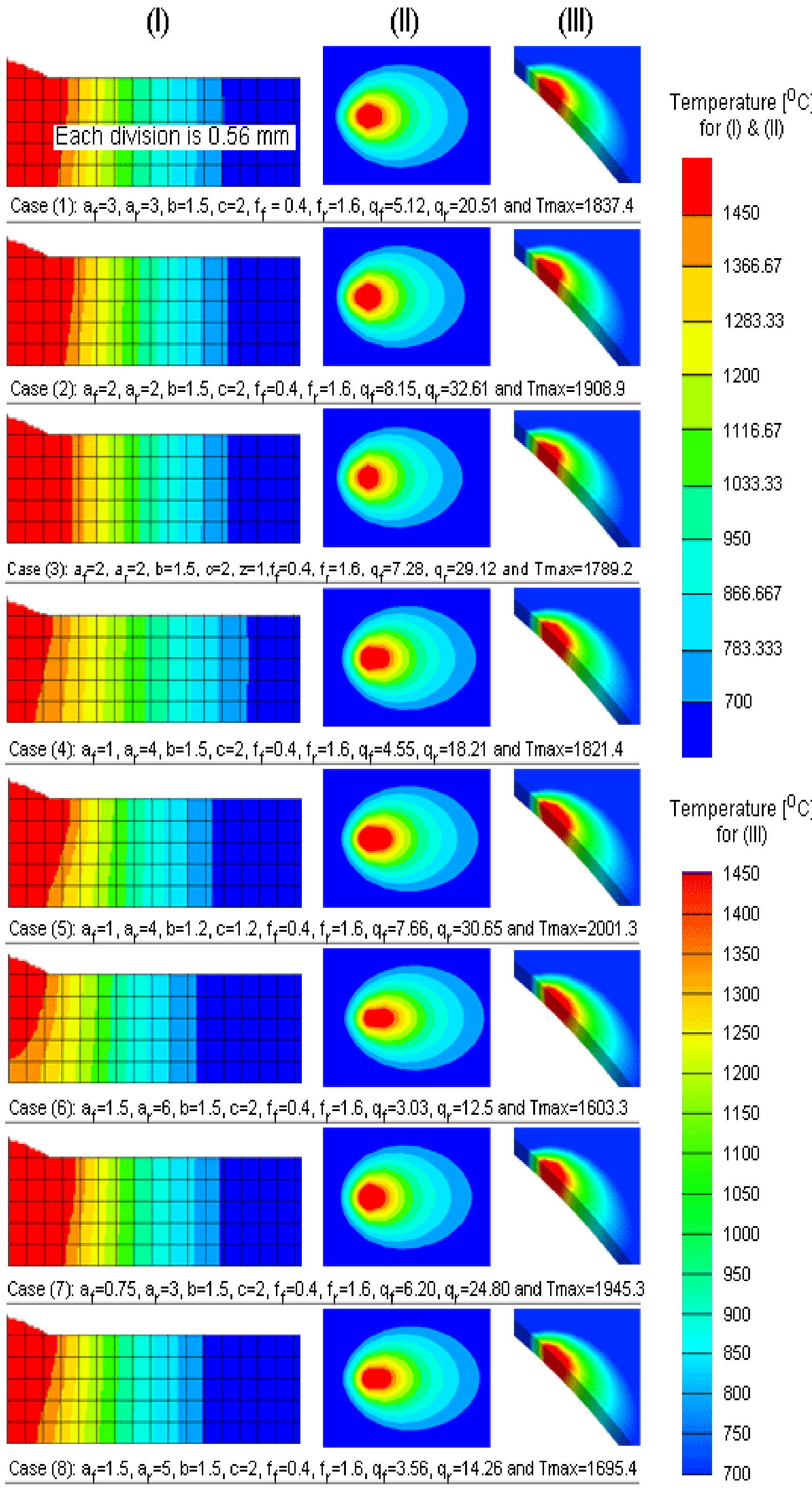

Fig. 4.5 Cases: 1-8. (I) Shape and size of fusion zone, (II) Temperature profile on the outer surface and (III) Volumetric heat flux distribution.

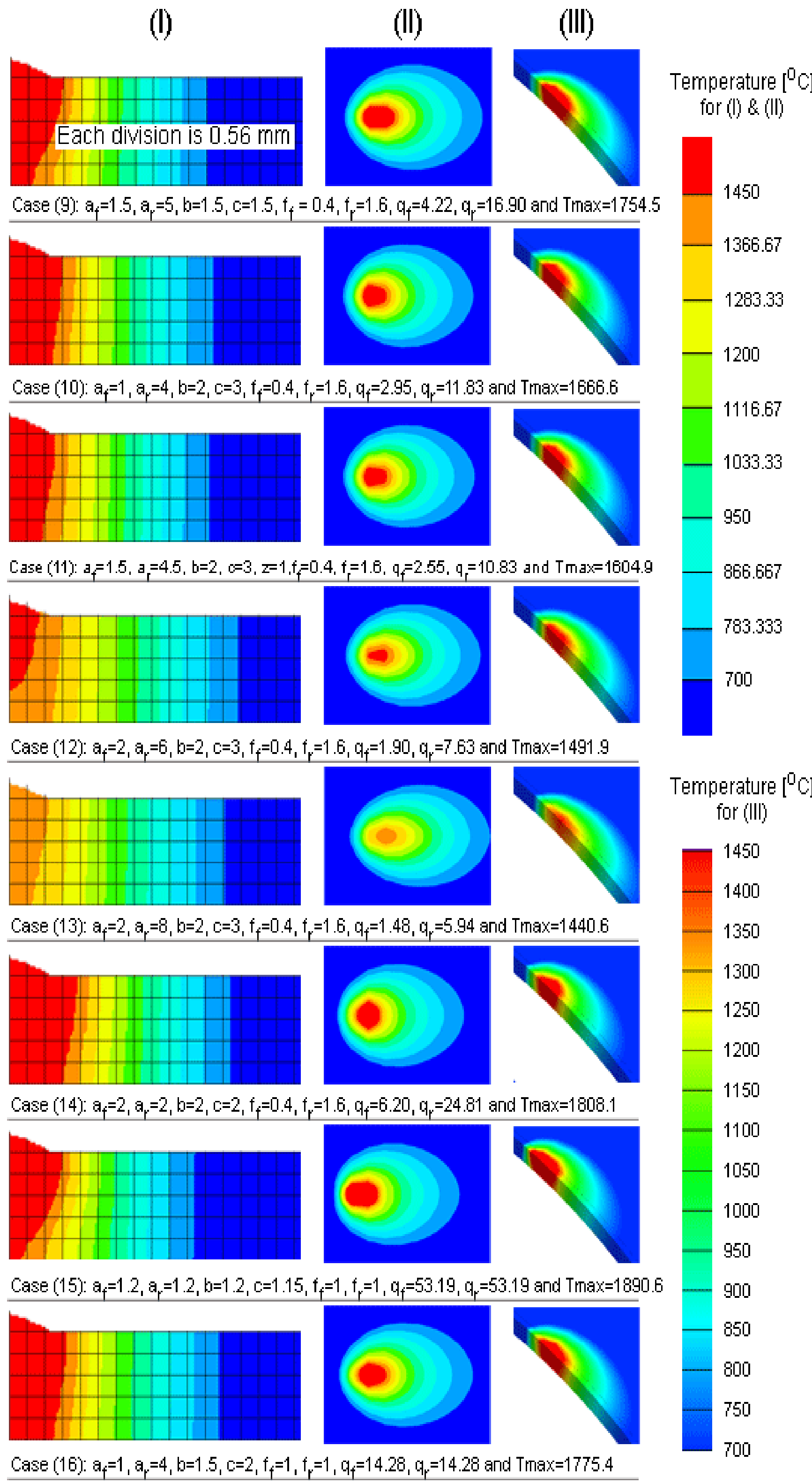

Fig. 4.6 Cases: 9-16. (I) Shape and size of fusion zone, (II) Temperature profile on the outer surface and (III) Volumetric heat flux distribution.

In case 3 and 11, z coordinate distance is considered as 1 mm, which represents the distance of moving heat source from the component surface. Whereas, for all remaining cases z coordinate distance is taken as zero. In case 2 and 3 all the geometric parameters are same except the z coordinate distance. Due to this in case 3, q_f, q_r and T_{max} values are less when compared to case 2. Cases 4 and 5 demonstrate the effect of heat source parameters b and c on weld pool size and shape while the other geometric parameters are kept unchanged. Case 6 and 7 reveal that as a_f and a_r increase the weld pool width and depth decreases, but its length increases. Also the same trend is observed for the cases of 10, 11, 12 and 13. Cases 8 and 9 reveal that the weld depth decreases as c decreases, consequently the weld width increases. The reason for the significant variation in FZ size and outer surface temperature profile is that the different values of volumetric heat flux densities as presented for sixteen different cases in Figs. 4.5 and 4.6. Also, it should be noted that the heat flux density is the function of moving heat source geometric parameters.

4.2.3. Welding temperature characteristics:

Numerical simulation of welding process, for the constant heat input of 375 J/mm at different combinations of moving heat source geometric parameters, is carried out for predicting the temperature distributions along the longitudinal direction of the cylindrical component. Figs. 4.7(a) and (b) depict the temperature distribution on the inner and outer surfaces, respectively and these are for three different cases of moving heat source geometric parameters at 180^o cross-section from the weld start position. For the cases of 6, 7 and 10, the front ellipsoid heat flux densities are 2.85, 6.20 and 3.28 W/mm^3 respectively; the rear ellipsoid heat flux densities are 11.40, 24.80 and 13.12 W/mm^3 respectively; and maximum temperatures are 1603.0^0C, 1945.3^0C and

1666.6^{0}C respectively. From Figs. 4.7(a) and (b), it is apparent that the peak temperatures at the WC line decrease on the both inner and outer surfaces as the moving heat source geometric parameters increase for the constant heat input.

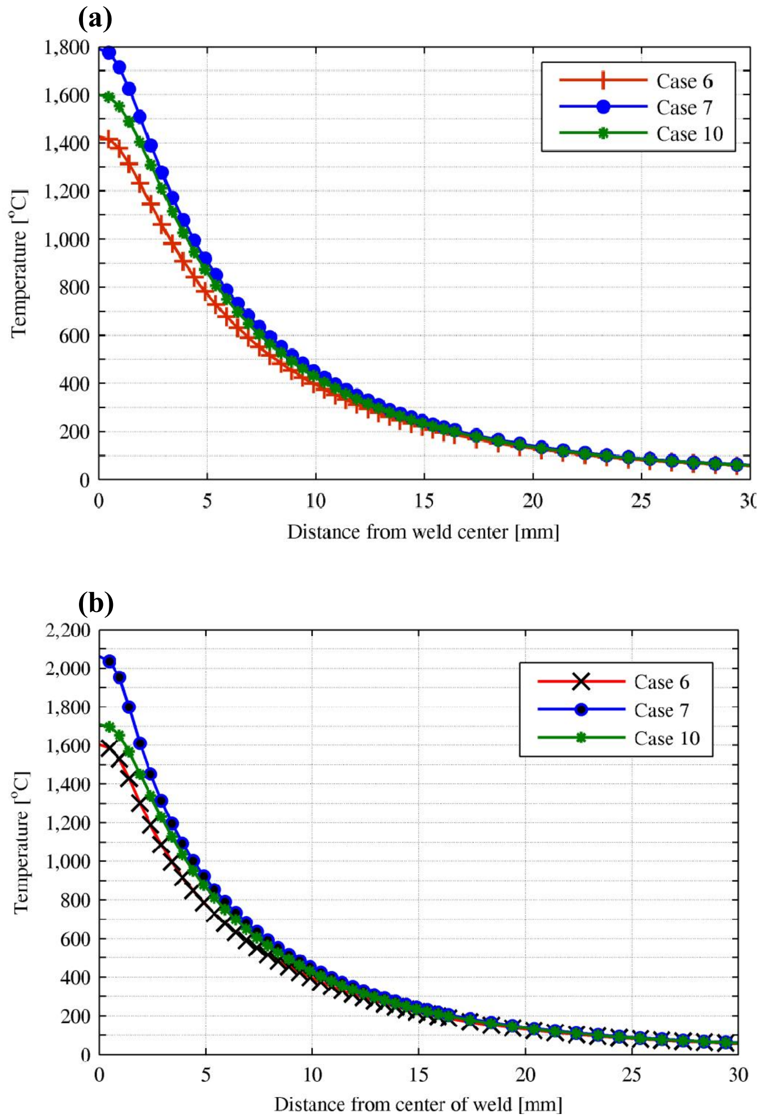

Fig. 4.7 Comparison between simulated thermal cycles for three different cases on the: (a) Inner surface and (b) Outer surface.

It is discerning to note that the variation in temperature distribution is noticed with in 3 mm from the WC line, beyond this no considerable variation is observed. The possible reason for this attribute could be that with the variation in heat flux densities and maximum temperatures for the three cases (7, 10 and 6) as shown in Figs. 4.5 and 4.6. This variation would also cause the localized heating at the FZ which changes the peak temperatures in FZ and has a noticeable effect on temperature distributions within the HAZ. Literature review reveals that a number of investigations have been undertaken by various authors to understand the effect of moving heat source geometric parameters. For instance, Gery et al. [25] described temperature distributions on the top surface of the weld plate along the longitudinal and transverse direction. Whereas, in this research temperature distributions are discussed for the SS 304 cylindrical component along the longitudinal direction and these results are in line with the earlier results by [25].

4.2.4. Residual stress distributions:

In the mechanical analysis axial, hoop and radial residual stresses are simulated on the outer and inner surface for three different cases of moving heat source geometric parameters. Figs. 4.8(a) and (b), Figs. 4.9(a) and (b), and Figs. 4.10(a) and (b) describe the axial, hoop and radial residual stress distributions respectively; on the inner and outer surfaces at 180^0 section from the weld start position. Each figure shows the stress distributions for three different simulation cases with constant heat input and weld speed.

In case of circumferentially butt joining of cylindrical components, residual stress normal to the direction of weld bead is called axial stress. Both tensile and compressive axial stress distributions are noticed along its length on the inner and outer surface as shown in Figs. 4.8(a) and (b). This is due to variable shrinkage patterns along its length by varying temperature gradients through its thickness and type of boundary constraints used to fix the component. On inner surface, high tensile axial residual stress is noticed at weld location (WL) diminish to zero and stress reversal from tensile to compressive is noticed beyond 15mm on both sides of WL as shown in Fig. 4.8(a). These compressive residual stresses reach to zero at about 50mm from WL on the both sides. Fig. 4.8(b) shows high compressive axial residual stresses at the WL on the outer surface.

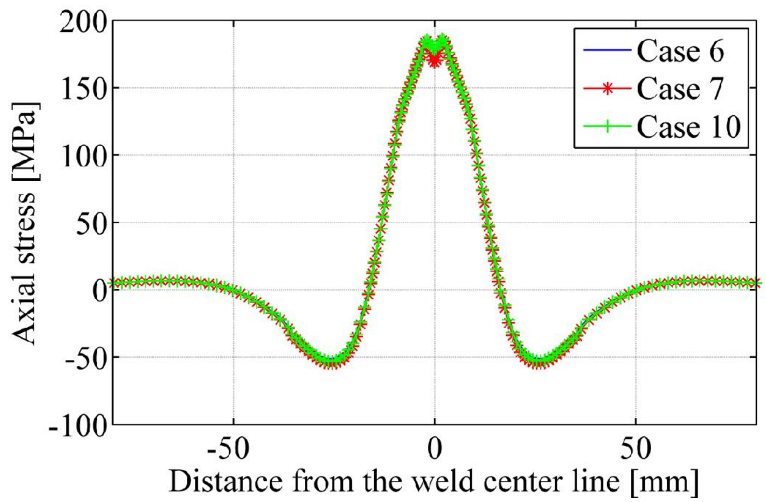

Fig. 4.8(a) Axial residual stress distributions for three different cases on the inner surface.

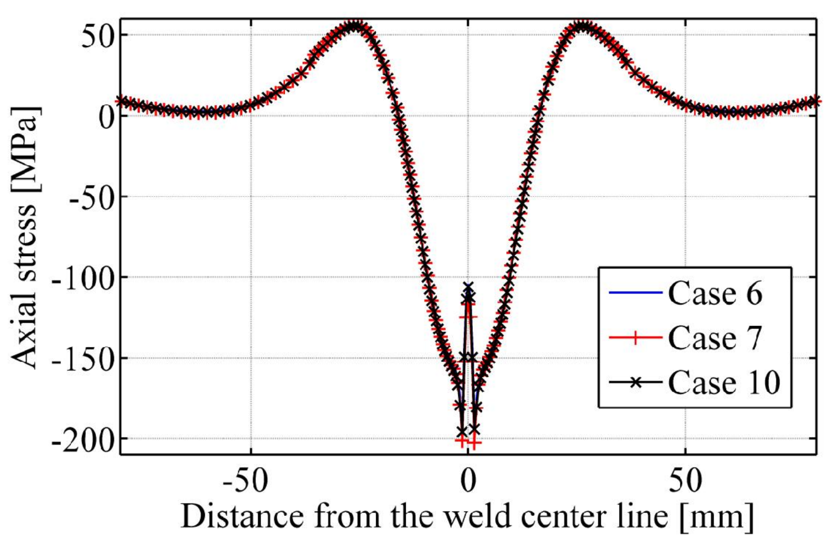

Fig. 4.8(b) Axial residual stress distributions for three different cases on the outer surface.

Residual stresses that are parallel to the direction of weld are called hoop residual stresses. Hoop residual stresses are generated due to expansion and contraction in radial direction during thermal cycling in the welding process. Also both tensile and compressive hoop stresses are observed along its length on the inner and outer surface as shown in Figs. 4.9(a) and (b). On the inner surface high tensile hoop residual stresses are observed at molten zone, and further stress reversal from tensile to compressive is noticed at about 10mm from the WL on both sides. Fig. 4.9(b) shows compressive hoop residual stresses on the outer surface within and adjacent to FZ and heat affected zone. Compressive residual stresses at the WL and at the HAZ are in Zig–Zag manner, reaches to zero at about 30mm from WL then stress reversal to tensile region on both sides of WL is observed. Lower compressive residual stresses are formed near the ends on both sides of WL. Based on the above observations, it can be concluded that the axial and hoop residual stress distributions are not influenced by heat source parameters.

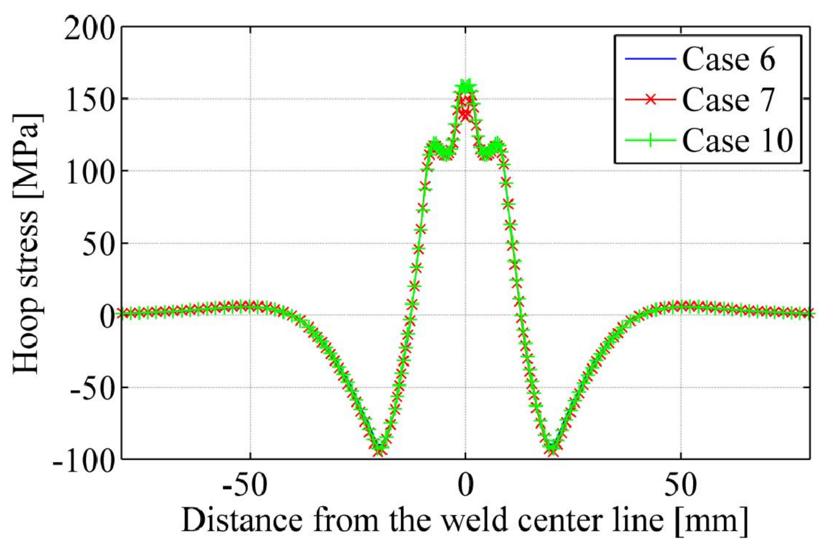

Fig. 4.9(a) Hoop residual stress distributions for three different cases on the inner surface.

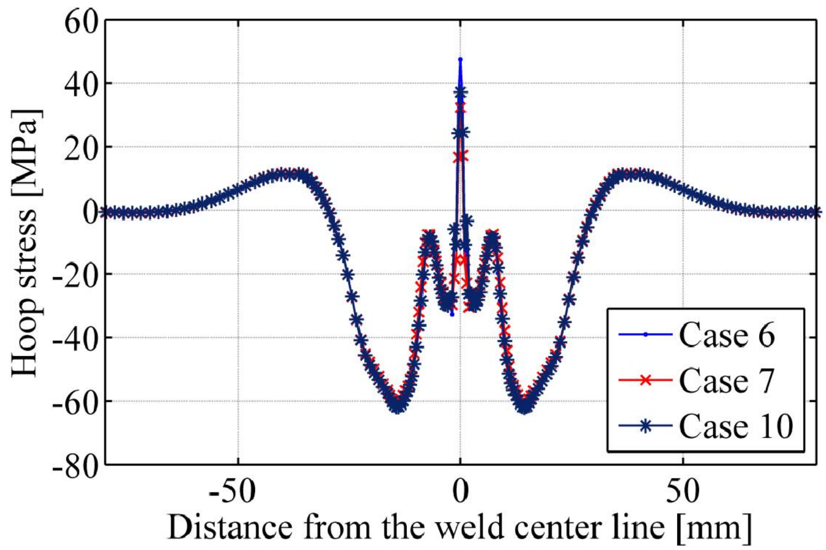

Fig. 4.9(b) Hoop residual stress distributions for three different cases on the outer surface.

Radial residual stress is the stress that acts towards or away from the central axis of a curved member. This is attributed to different temperature profiles through its wall thickness of the cylinders. Variable shrinkage patterns through the wall thickness occur due to different temperature gradients generates radial residual stresses on both sides of WL. Radial residual stress distributions on inner surface and outer surface along the length of the component are shown in Figs. 4.10(a) and (b). On the inner and outer surface, the magnitude of radial stresses is almost of zero along its length. At the ends, peak tensile radial stresses are observed due to boundary constraints during welding simulation as shown in Fig. 4.2. A significant research work has been undertaken to investigate the variation in residual stress distributions due to the influence of yield strength, different heat inputs, weld sequence, the effect of plasticity and groove configuration, dissimilar materials, sensitivity of analysis variables, preheating effect etc. Whereas, in this study it is very important to note that with the variation in moving heat source geometric parameters do not influence on the residual stress distributions. The probable reason for this could be that the heat input to the welded component is same (i.e. 375J/mm) for all the three cases. Also, as per the earlier literature, the variation of heat input influences the residual stress distributions. A careful consideration of the results, from Figs. 4.8-4.10, reveals that the trends for residual stresses also concur well with the observations recorded by the previous researchers [50, 110].

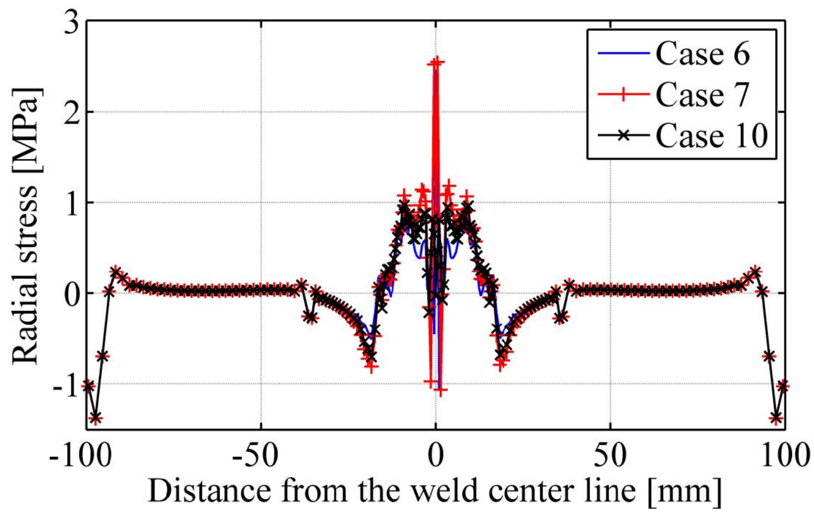

Fig. 4.10(a) Radial residual stress distributions for three different cases on the inner surface.

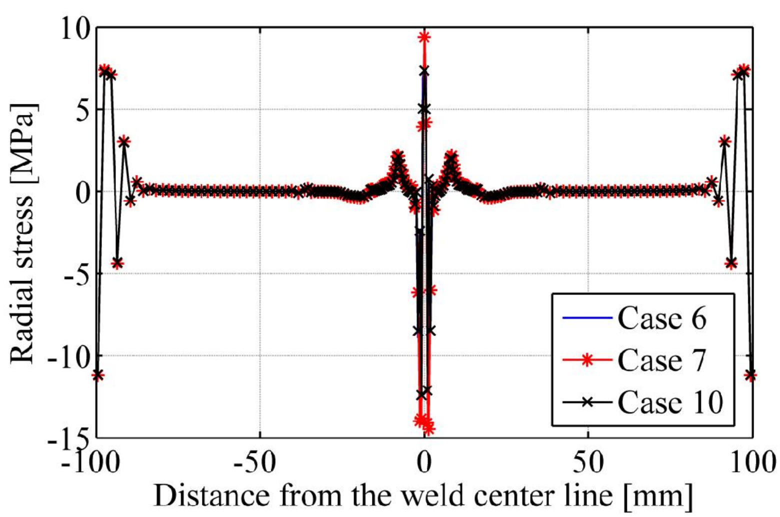

Fig. 4.10(b) Radial residual stress distributions for three different cases on the outer surface.

CHAPTER - 05

COMPARISON OF WELD CHARACTERISTICS BETWEEN L-SEAM AND C-SEAM BUTT WELD JOINTS OF CYLINDRICAL COMPONENTS

The control of weld induced residual stresses and distortions are very important in L-Seam and C-Seam butt joints of cylindrical components. It can be observed from the detailed literature survey that comparative study of weld characteristics between L-Seam and C-Seam butt weld joints has not been undertaken to study the effect of variation in temperature distributions and residual stresses on cylindrical components. Further, literature survey also reveals that comparative study has not been reported on the L-Seam and C-Seam welds of different r/t ratios for AISI 304 SS. Thus in-depth study of weld temperature characteristics, maximum temperature, weld pool (FZ and HAZ) shapes and sizes and weld induced residual stresses for the cases of L-Seam and C-Seam weld joints was carried out in this research. This resulted in improvement of fatigue life, reduction in SCC and fracture. In this investigation, similar groove geometry, BC, weld sequencing (progressive welding), wall thickness and the relatively constant heat input are used to compare the weld characteristics between L-Seam and C-Seam butt weld joints of cylindrical components by using numerical simulation and experimental validation. In this study, a 3D, sequentially coupled thermo-metallurgical-mechanical analysis was performed for L-Seam and C-Seam butt weld joints of AISI 304 cylindrical components to evaluate weld characteristics during GTAW process. Initially, weld experiments are carried out to obtain the heat input and the macrographs which are further validated with the predicted weld molten pool sizes during HSF analysis. The Goldak's double ellipsoid heat source function obtained in HSF analysis was employed in the thermal and mechanical analysis. The results reveal that there are significant differences in residual stress distributions between L-Seam and C-Seam butt joints. Full scale shop floor welding experiments are also performed to verify the effectiveness of the proposed numerical models and these are in good agreement with the experimental measurements.

5.1. Experimental strategy:

Based on the wall thickness, metal joining was commonly produced by using either single or double-V butt joint configuration and single or multi pass arc welding processes. Among different arc welding processes, GTAW was the obvious selection due to its (i) superiority in weld quality (ii) clean weld without impurities due to shielding gas (iii) very less weld spatter; and (iv) less weld defects. The material AISI 304 SS has excellent properties like drawing, forming, high ductility and better corrosion resistance. Hence, this material dominates in most of the engineering applications. Therefore, in this study single-V groove butt joint configuration, single pass GTAW process and AISI 304 SS as base material were considered for both L-Seam and C-Seam welds.

5.1.1. Consumables:

The filler material used was SS 308 having diameter of 1.6 mm and argon was used as shielding gas for all the experiments. Welding experiments for both the seam joints were carried out on 2.77 mm thick × 219.1 mm outer diameter cylindrical sections which were equivalent to 200 NB-SCH 5 standard pipe dimensions. The 2D line diagram with the dimensional details of cylindrical sections and the weld bead geometry was shown in Fig. 5.1. C-Seam weld experiments were carried out on two cylindrical components each of 100 mm length were initially tack welded together circumferentially and was shown in Fig. 5.2(a). Primarily 200 NB-SCH 5 standard pipe of 200 mm length was taken and sliced longitudinally prior to edge preparation and L-Seam welding as show in Fig. 5.2(b). Also the L-Seam weld component was initially tack welded at the start and end locations of weld. The chemical composition of 304 SS material used in this investigation was listed in Table 5.1.

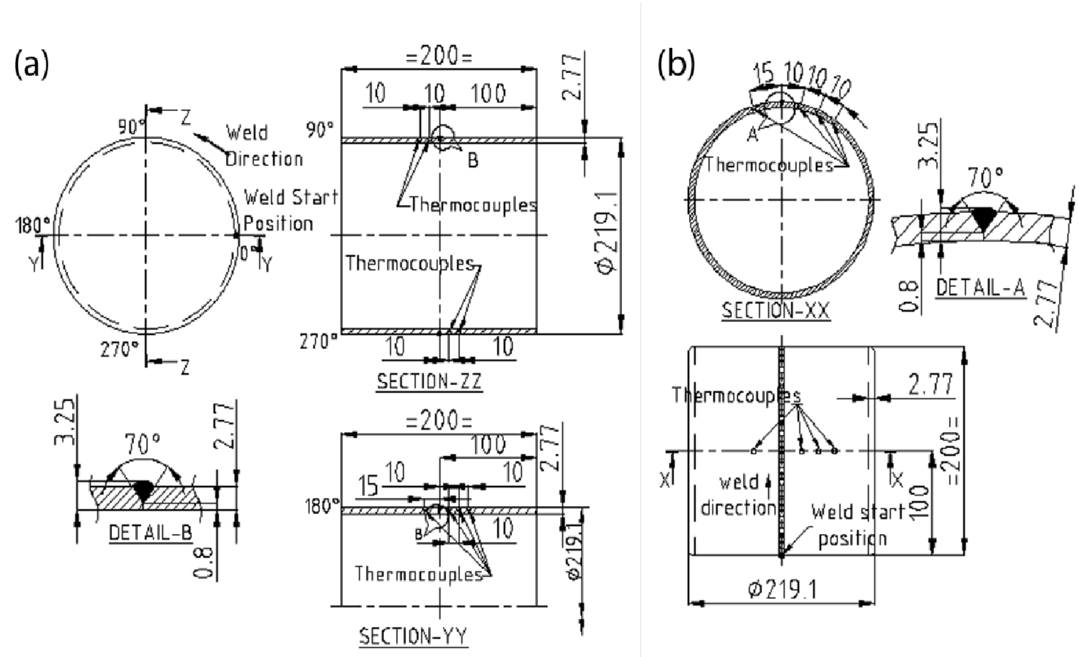

Fig. 5.1 2D line diagram of cylindrical sections: (a) C-Seam and (b) L-Seam.

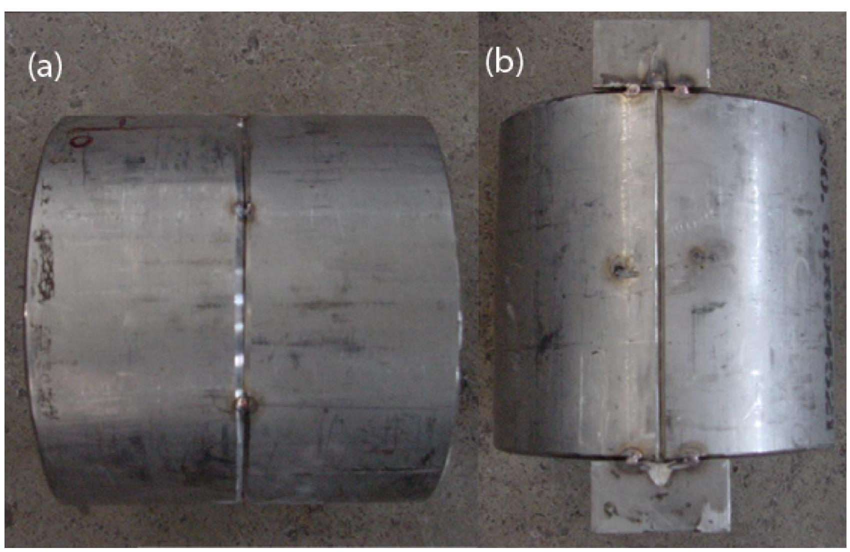

Fig. 5.2 Pipes with tack welds: (a) C-Seam and (b) L-Seam.

Table 5.1 Chemical composition (in Wt %) of AISI 304 SS.

C	Cr	Mn	Ni	Si	S	P	Fe
0.07	16-18	1.1-1.3	8.4-9.4	<= 1	<= 0.03	<= 0.045	Bal.

5.1.2. Welding procedure:

For the welding experiments of both L-Seam and C-Seam 200 NB-SCH 5, 55 A current and 10 V voltage, weld speed of 1 mm/s were considered to obtain proper bead shape which was further validated and described in Section 5.2.2. Fig. 5.3 shows the schematic for both L-Seam and C-Seam experimental weld setup with data logging system. Heat input in GTAW was a measure of energy transferred per unit length of weld. The heat input (Q) in J/mm was the ratio of weld power and speed (i.e. Q= $\eta VI/S$). Where η = weld efficiency, V= voltage, I= current and S= weld speed (mm/s). The above mentioned process parameters with an arc efficiency (η=0.7) give the heat input per unit length of weld was 385 J/mm which was equal to the heat input that was used in FE simulation.

5.1.3. Temperature, residual stress and microscopy:

Temperatures were measured using Chromel-Alumel (K-type) thermocouples connected at different locations on the outer surface of L-Seam and C-Seam cylindrical components by silver brazing. The location of thermocouples, weld start position and its direction were shown in Fig. 5.1. For L-Seam weld, six thermocouples (three on each side) were located at the mid plane in the axial direction. For C-Seam weld, total ten numbers of thermocouples were connected at 90^o, 180^o and 270^o planes from the weld start position. The transient thermal cycles were recorded with a data acquisition system for every one second interval. X- Ray

Diffraction (XRD) technique was used for measuring the residual stresses on the external surface. The details pertaining to determination of residual stresses using XRD were given in [116, 117]. Rossini *et al.* [118] classified different residual stress measurement methods and provided an overview of some of the recent advances in this area. To obtain microscopy of L-Seam and C-Seam welds, transverse sections of the weld sample were ground and polished up to 3 micron finish and etched in 2% Nital solution to measure the experimental weld pool shape.

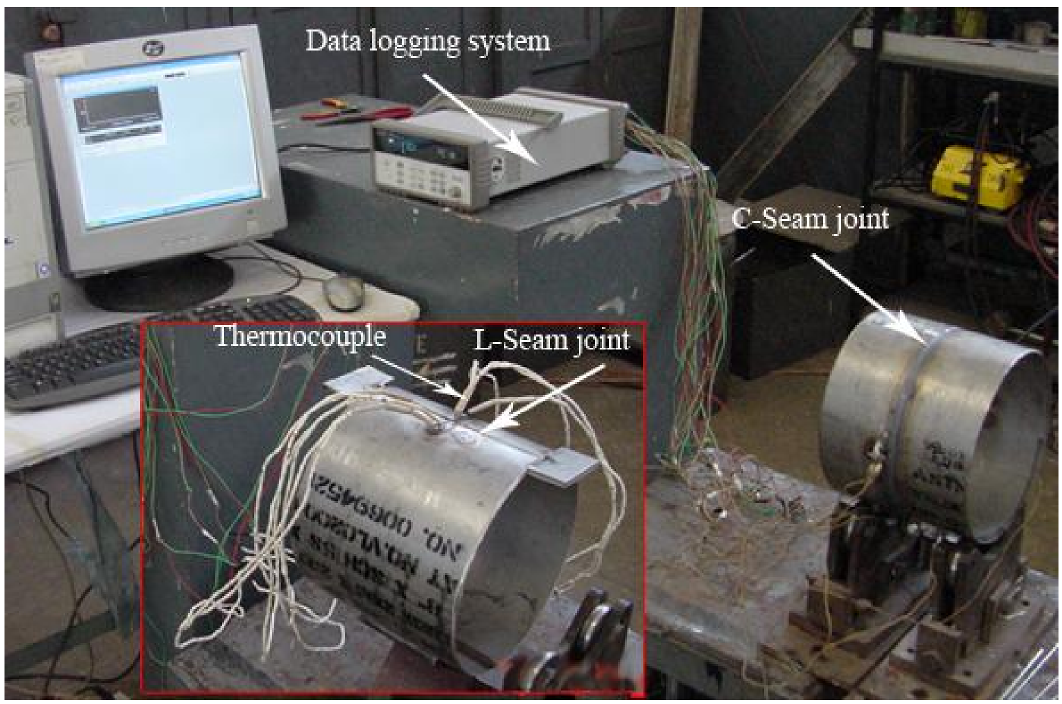

Fig. 5.3 Experimental and weld setup for the both L-Seam and C-Seam welds.

5.2. Numerical simulations:

During simulation, the initial temperature was assumed to be 25^{0}C (ambient temperature) and the material properties for both base and weld metal were assumed to have the same mechanical and thermal properties. Temperature dependent thermal and mechanical properties of AISI 304 SS material were considered for the FE simulation. The temperature dependent thermo-physical and thermo-mechanical properties were shown in Figs. 3.1 and 3.2 respectively and the temperature independent material properties and constants were described in the Section 3.5.1.

5.2.1. FE model:

In order to accurately measure the thermal cycles and residual stresses, full 3D FE models for both L-Seam and C-Seam welds of cylindrical components were developed and these were shown in Fig. 5.4. Initially two separate 2D meshes were generated for both the L-Seam and C-Seam welds. Then the 2D mesh of L-Seam was extruded by translation in longitudinal direction for a length of 200 mm to create a 3D mesh which was used for L-Seam welding simulation. Also the 2D mesh of C-Seam was extruded by rotation in circumferential direction for an angle of 360^o to create a 3D mesh of C-Seam weld. The dimensions of cylinder for simulation model and for experiments were same and these were given in Fig. 5.1. In the process of FE meshing, three types of elements were used such as One Dimensional (1D) linear elements, 2D and 3D quadrilateral elements. 1D linear elements were used to represent the weld trajectory and reference lines. Weld trajectory was a line along which the pre-defined heat source moves and the reference line was defined as a group of linear elements parallel to the weld trajectory line. The weld trajectory and the reference lines have same length and same number of elements. Element sizes of 3 mm for C-Seam and 2 mm for L-Seam were used along the trajectory and the reference lines. 2D quadrilateral elements were used to mesh the surfaces which were subjected to heat loss during welding process. 3D quadrilateral elements were used to mesh the weld bead and the parent metal. It can be observed from Figs. 5.4(a) and (b), that different element sizes were used during meshing to reduce the computation time.

The mesh density was higher in the HAZ when compared to parent metal. For the C-Seam weld, in longitudinal direction, the element size within and adjacent to HAZ was kept constant equal to 1 mm and at longitudinally away from HAZ, it was kept at constant value of 3 mm. In radial direction the material wall thickness (i.e. 2.77 mm) was divided into five segments within and adjacent to the HAZ. In the parent metal of C-Seam weld wall thickness was divided into three segments. In circumferential direction, the element size was kept constant (i.e. 3 mm uniformly) as shown in Fig. 5.4(b). For the L-Seam weld, in circumferential direction, the element size within 45^{o} from the WC line was 1 mm and beyond 45^{o} mesh size was 3 mm as shown in Fig. 5.4(a). In radial direction, the material wall thickness (i.e. 2.77 mm) was divided into three segments in HAZ and parent metal. In longitudinal direction, the element size was kept constant equal to 2 mm uniformly.

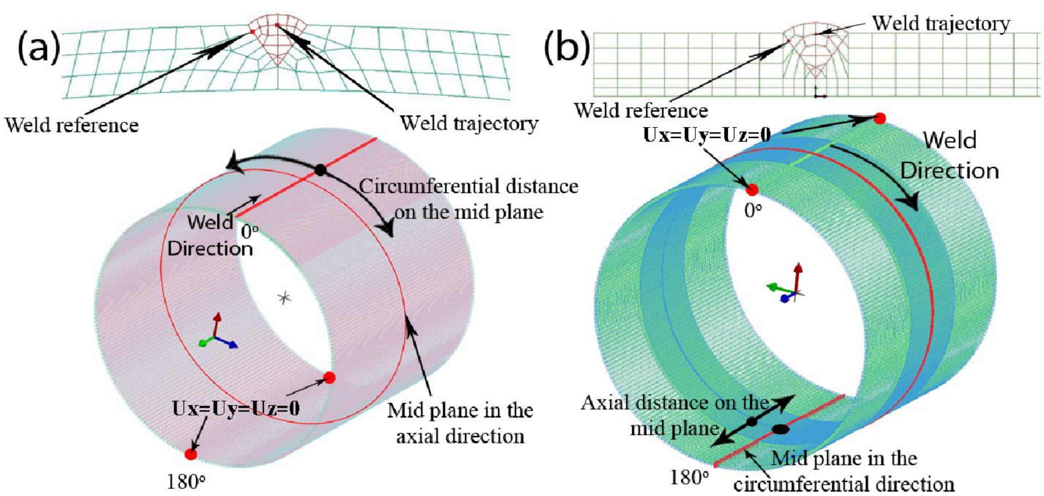

Fig. 5.4 FE 2D and 3D mesh with boundary conditions: (a) L-Seam and (b) C-Seam.

5.2.2. Heat source fitting analysis:

The amount of heat input plays an important role because it affects the mechanical properties and metallurgical structure of the weld and HAZ. Hence the HSF analysis was carried out to find out the best choice of heat input. In SYSWELD, the heat source model parameters can be adjusted by using HSF tool. HSF was a steady state thermal analysis, which takes relatively a shorter computational time. The fusion boundary profile was an output of this analysis. During this analysis, the initial temperature of the component was considered at 25^0C. The front and rear fractions of the heat source f_f and f_r were considered as 0.4 and 1.6 respectively. The double ellipsoid heat source parameters and the amount of heat input were iteratively adjusted till the FZ shape was similar to macrograph. The energy input with the weld speed of 1 mm/s for both L-8 and C-8 cases was 385 J/mm, whereas for both L-6 and C-6 cases it was 375 J/mm and these were mentioned in Table 5.2. The Gaussian parameters for the double ellipsoid heat source were chosen as a_f = 1 mm, a_r = 4 mm, b= 0.75 mm and c=0.9 mm. These parameters were selected after iterative adjustment of Gaussian heat source parameters during HSF analysis and the predicted FE simulation weld molten pool sizes were compared with the experimental macrograph cross sections. The methodology followed is described below. The front (q_f) and rear (q_r) volumetric heat flux densities (w/mm^3) based on the considered heat input, Gaussian parameters and the velocity were obtained as q_f = 16.64 w/mm^3 and q_r = 66.56 w/mm^3 for both L-8 and C-8 cases. Similarly, for both L-6 and C-6 cases q_f = 15.76 w/mm^3 and q_r = 63.07 w/mm^3 were attained.

Table 5.2 Different FE simulation cases.

Case	**Weld description**	**Pipe size**	**Pipe O.D and wall thickness (mm)**	**Weld power = V×I (W)**	**Heat input (J/mm)**	**Inner radius to wall thickness ratio (R_i/T)**
L-8	L-Seam-8 inch Dia.	200 NB-SCH 5	219.1 and 2.77	385	385	38.5
C-8	C-Seam-8 inch Dia.	200 NB-SCH 5	219.1 and 2.77	385	385	38.5
L-6	L-Seam-6 inch Dia.	150 NB-SCH 5	168.3 and 2.77	375	375	29.37
C-6	C-Seam-6 inch Dia.	150 NB-SCH 5	168.3 and 2.77	375	375	29.37

In this investigation, on the basis of the parameters defined by the HSF tool, a transient thermal analysis was carried out by using numerical simulations for four different cases (L-8, C-8, L-6 and C-6) as described in Table 5.2. Temperature distributions and weld molten pool sizes for all the four cases were shown in Fig. 5.5. Further, the HAZ was found to be a series of contours ranging from 700^{0}C to 1450^{0}C. From Fig. 5.5, proper shape and boundaries of FZ were found; this reveals to give better weld penetration for all the four cases.

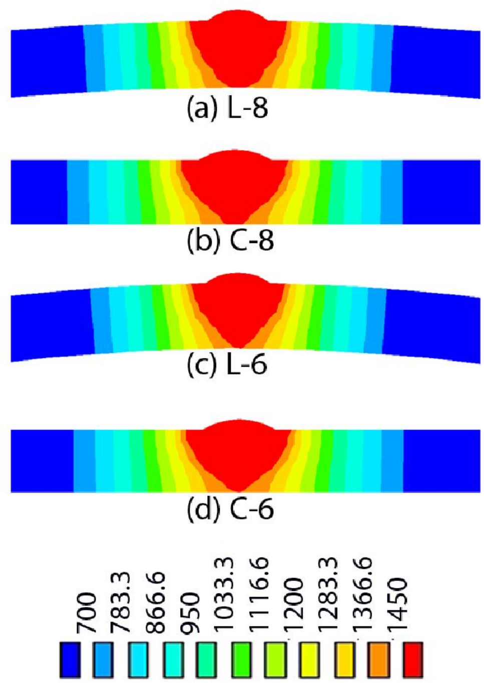

Fig. 5.5 FE weld molten pools obtained in the HSF analysis.

During GTAW experiments, for L-8 and C-8 cases, 55 A current and 10 V voltage were supplied for the considered weld speed of 1 mm/s. As explained in Section 5.1.2, these weld process parameters give the heat input per unit weld length equal to the heat input that was used in FE simulation. Figs. 5.6(a) and (b), confer an overview of the comparison between macrograph and the FE simulation weld pool dimensions. The comparison of experimental macrograph cross section and the predicted FE simulation weld molten pool for L-8 and C-8 cases were shown in Figs. 5.6(a) and (b) respectively; and it could be observed that the results were in good agreement with each other. The results obtained after iterative adjustment of heat sources were then saved to a function database for further used in the thermal and mechanical analysis.

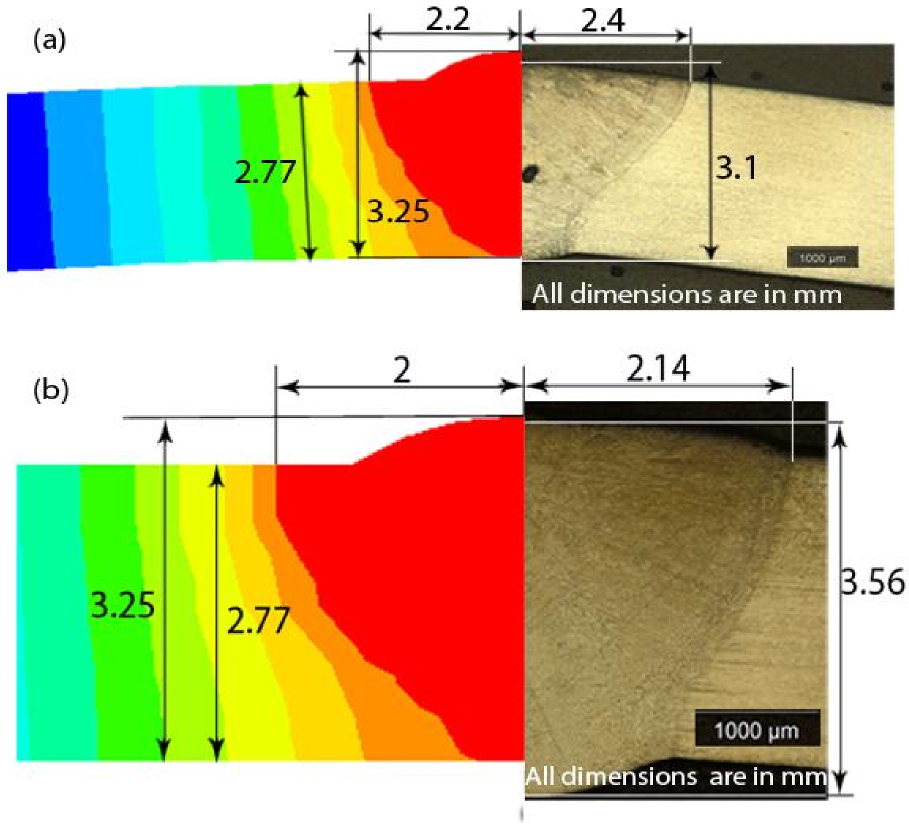

Fig. 5.6 Validation of experimental macrograph and the FE weld molten pool sizes for the cases of: (a) L-Seam and (b) C-Seam.

During L-Seam and C-Seam weld experiments, parent material was not clamped. To match the experimental BC, minimum clamping was applied as the artificial boundary condition in order to prevent rigid body motion in the numerical simulation. The detailed BC used in the FE model were shown in Fig. 5.4.

For L-Seam numerical simulation case, two nodes at the 180^{o} section (i.e. mid plane in the circumferential direction) were constrained in X, Y and Z directions. For the case of C-Seam numerical simulation, two nodes at 0^{o} section were constrained in all the three directions. These BC do not affect the stress magnitudes for both the L-Seam and C-Seam FE simulation.

5.3. Experimental validation of predicted temperature and stress fields:

To ensure the reliability of the developed FE model, both the temperature profiles and residual stresses from the numerical simulation were validated with the experimental measurements. The temperature profiles from the numerical simulation for L-8 and C-8 cases were validated as shown in Fig. 5.7. The locations 10, 15 and 20 mm away from the WC line were considered along the circumferential and axial direction for L-8 and C-8 respectively. The thermocouple locations, circumferential and axial directions were shown in Figs. 5.1 and 5.4. From Fig. 5.7, it can be observed that the experimental and the predicted FE results match well at 10 mm location. Whereas, at 15 and 20 mm locations, variation of predicted and measured temperatures were observed and were reasonably comparable. During heating, the rate of increase in temperature was in correspondence with each other. However, during cooling the experimental values were slightly higher than the predicted results. This temperature difference between experiments and simulations could be due to the different heat losses between experiments and simulations. The maximum difference in peak temperatures between experimental and FE simulation was observed to be 8% at 15 mm location for the L-8 case. The observations and the trends seen during heating and cooling in this study were found to be in agreement with those obtained by other investigators [37, 110].

Based on the simulation results, the peak hoop stresses were noticed for L-Seam weld joint and the peak axial stresses were observed for C-Seam weld joint. Hence, in this section, the measured data of hoop stresses and axial stresses for L-8 and C-8 were compared with the numerical simulation results and were plotted in Fig. 5.8 with error bars for the experimental data. XRD technique was used for measuring the residual stresses on the outer surface. The hoop stresses and the axial stresses were measured on the outer surface at seven different locations, viz. at WC and at 8, 16 and 24 mm away from the WC on the both sides of weld. These locations were considered along the circumferential direction and the axial direction for L-8 and C-8 respectively. Fig. 5.8 illustrates that the axial stresses of C-8 case and the hoop stresses of L-8 case predicted by the FE model match the trend of the corresponding measured data. It could be seen that the results of axial stresses for the C-8 case were in reasonable agreement with each other in addition to the close match of trend.

Meanwhile, Fig. 5.8 also indicates that the hoop stresses for the L-8 case by the FE simulation were considerably higher than the measured data. Some of the reasons for the discrepancy produced between predictions and the measurements of hoop stresses for the L-8 case can be described as follows. In general, the origins of discrepancy may be due to the inaccuracies of FE model and the errors caused by measurement methods. In this study, for L-Seam welding, pipe was sliced longitudinally before the edge preparation. Due to this, the diameter of the pipe was enlarged with the tensile residual stresses trying to hold the pipe slit open. Further, the pipe was pressed till the ends were overlapped in order to completely close the gap between the ends. During this process, the compressive residual stresses might have been generated in the pipe. Then the fit up pads were welded at the weld S/E locations as shown in Fig. 5.2(b). In addition to this, manufacturing operations for the edge preparation may cause redistribution of residual stresses that may significantly modify the weld residual stresses. Overall, on the aspect of FE model, the initial residual stresses which were generated due to manufacturing process and the machining before welding were ignored. Based on the above discussion, it was identified that the predicted results and the experimental measurements were aligning, thus the developed FE models were experimentally validated. The trends for stress distributions were concur with the observations recorded by the previous researchers [38, 39, 110].

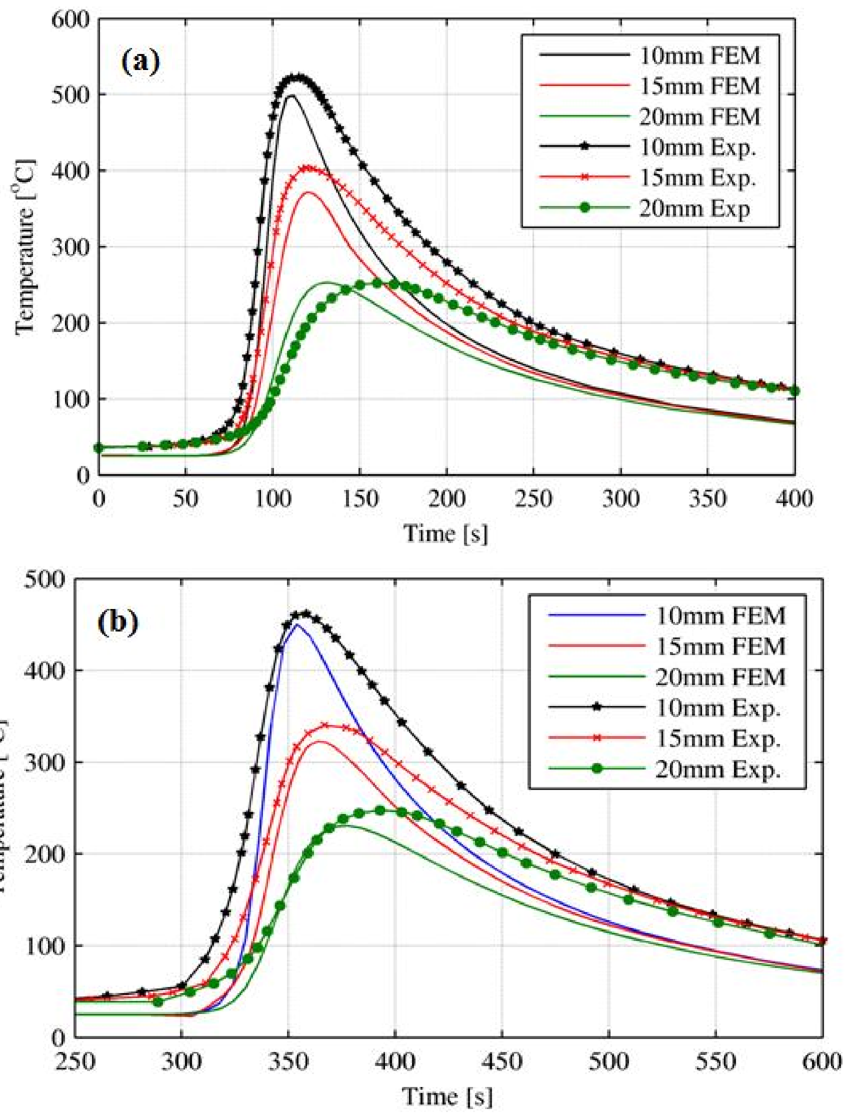

Fig. 5.7 Validation of predicted and measured transient temperature profiles at different locations: (a) L-Seam-8 inch and (b) C-Seam-8 inch.

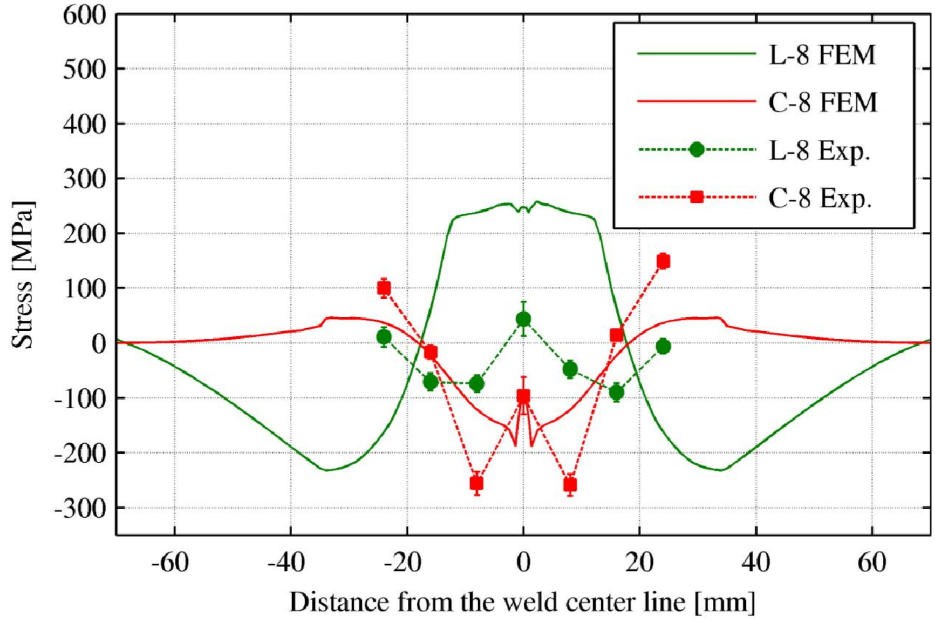

Fig. 5.8 Comparison between experimental data and FE simulation residual stresses on the external surface.

5.4. Results and discussions:

To ascertain the influence of L-Seam and C-Seam butt weld joints of cylindrical components on weld temperature characteristics and residual stresses, four different numerical simulation cases were studied and the corresponding results were described in the following sections. These four cases were shown in Table 5.2. The weld speed was considered as 1 mm/s and the simulation was run for a time period of 10,000 s.

5.4.1. Weld temperature cycles:

Temperature distributions were predicted for the four different FE simulation cases such as 200 NB-SCH 5 (L-Seam and C-Seam) and 150 NB-SCH 5 (L-Seam and C-Seam) as given in Table 5.2. The 3D temperature profiles on the outer surface obtained for L-Seam-200 NB at 108 s and C-Seam-150 NB at 186 s were shown in Figs. 5.9 and 5.10 respectively.

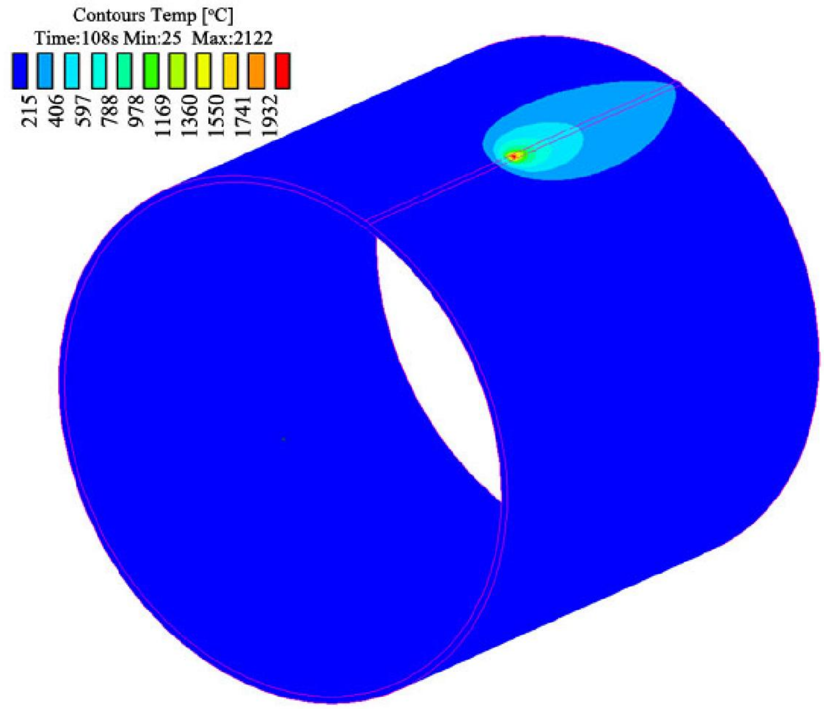

Fig. 5.9 3D temperature profile on the outer surface for L-Seam-8 inch at 108 s.

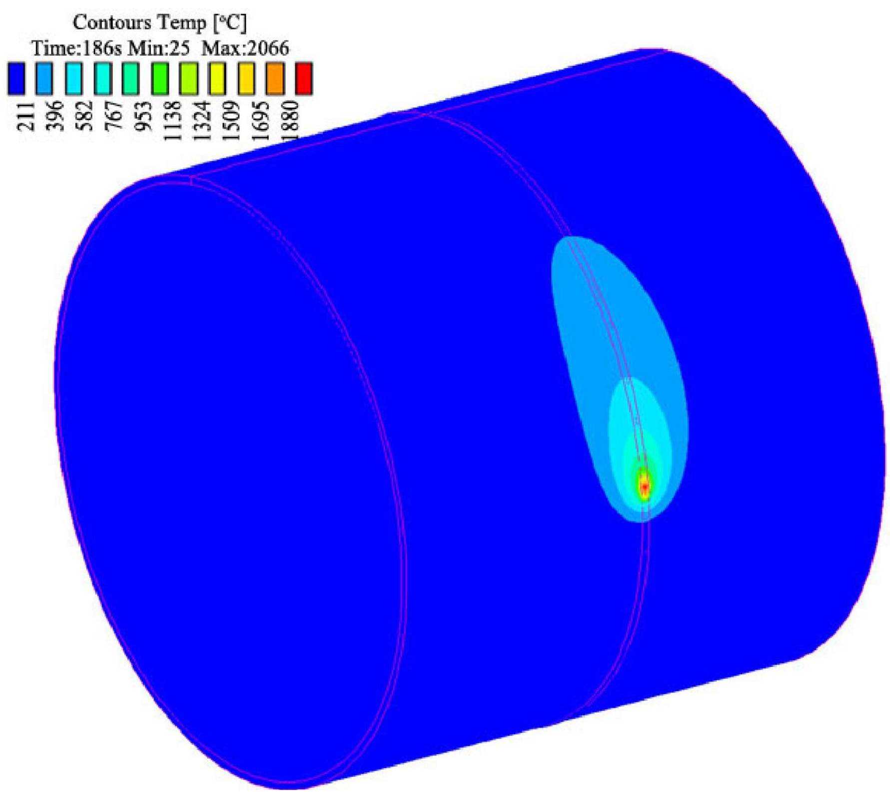

Fig. 5.10 3D temperature profile on the outer surface for C-Seam-8 inch at 186 s.

As anticipated the peak temperatures were observed at the WC line. The figures clearly show the steep temperature gradients ahead of the heat source, because of less heat flow in front of the weld torch. The gradients trailing the weld torch indicate the cooling phenomenon of the work pieces after peak temperature was achieved. Also, the elliptical shaped temperature profiles were observed for both L-Seam and C-Seam welds and these were in agreement with previous results by [37, 105, and 110].

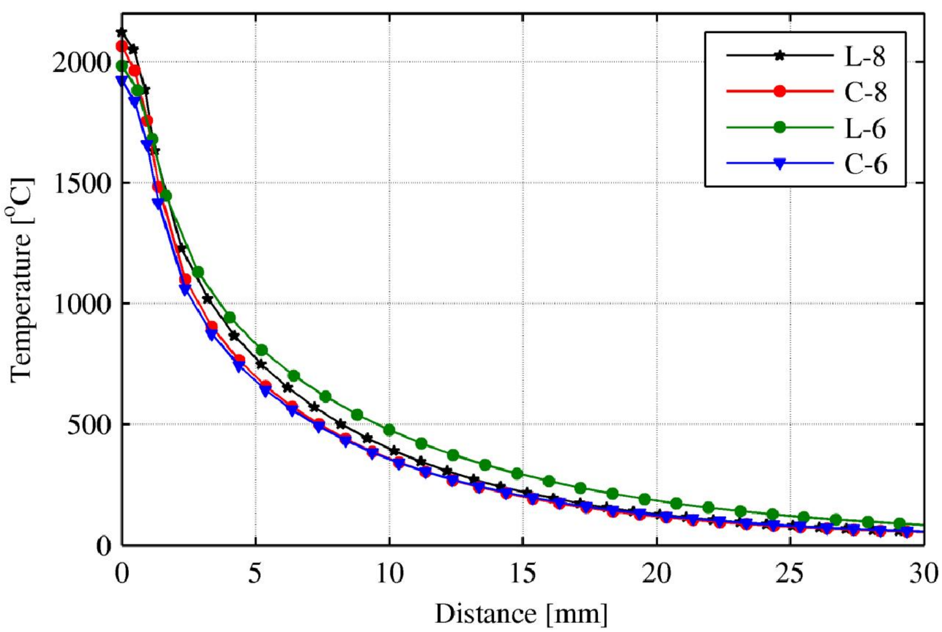

Fig. 5.11 Temperature distributions: Axial distance for C-Seam and circumferential distance for L-Seam weld.

Figs. 5.11-5.13 show the temperature distributions on the outer surface during welding process for four different cases (L-8, C-8, L-6 and C-6). It was illustrated in Table 5.2. Fig. 5.11 depicts temperature versus axial distance for C-Seam and circumferential distance for L-Seam welds. Figs. 5.12 and 5.13 illustrate the transient thermal cycles for the locations at the WC and at 7.5 mm away from the WC line. For C-Seam welds, the locations WC (i.e. 0 mm) and 7.5 mm were considered along the axial direction at 180° cross-section (i.e. mid plane in the circumferential direction) from the weld start position. For L-Seam welds, the locations WC and 7.5 mm were considered along the circumferential direction at 100 mm cross-section (i.e. mid plane in the axial direction) from the weld start position.

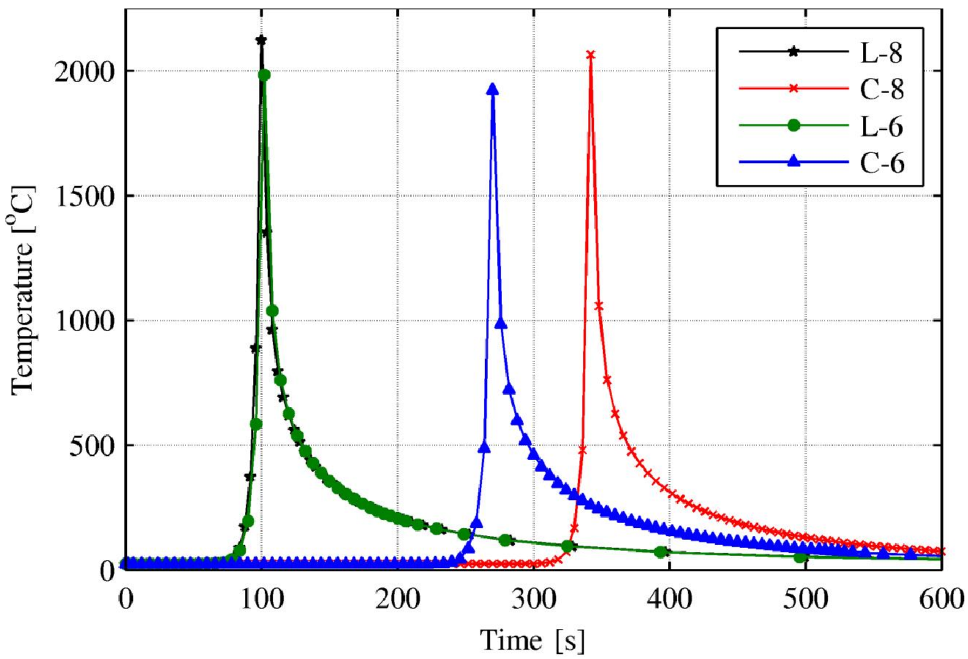

Fig. 5.12 Temperature distributions: Transient thermal cycles at WC.

From Fig. 5.11, it can be observed that for L-8 and C-8 the maximum temperature at the weld pool was 2122^0C and 2064^0C respectively. Similarly, for L-6 and C-6 the maximum temperature at the weld pool was 1983^0C and 1923^0C respectively. From Figs. 5.12 and 5.13, it was apparent that the peak temperatures were observed at sections when heat source crosses the section. For example, in case of L-Seam weld with weld speed of 1 mm/s over a length of 200 mm, the weld torch reaches the 100 mm section at 100 s. Similarly, for the cases of C-Seam weld (C-8 and C-6) with the weld speed of 1 mm/s, when the weld torch travels around the circumferences ($\pi \times D$) of 3.14 × 219.1 mm= 687.9 mm and 3.14 × 168.3 mm= 528.4 mm, the weld torch reaches the 180° section at 343.9 s and 264.2 s respectively. From Figs. 5.11-5.13, it can be concluded that the peak temperatures at the WC and at the locations away from the weld centre for the cases of L-Seam welds were slightly higher than C-Seam welds. The difference in peak temperature between L-Seam and C-Seam welds was around 60^0C.

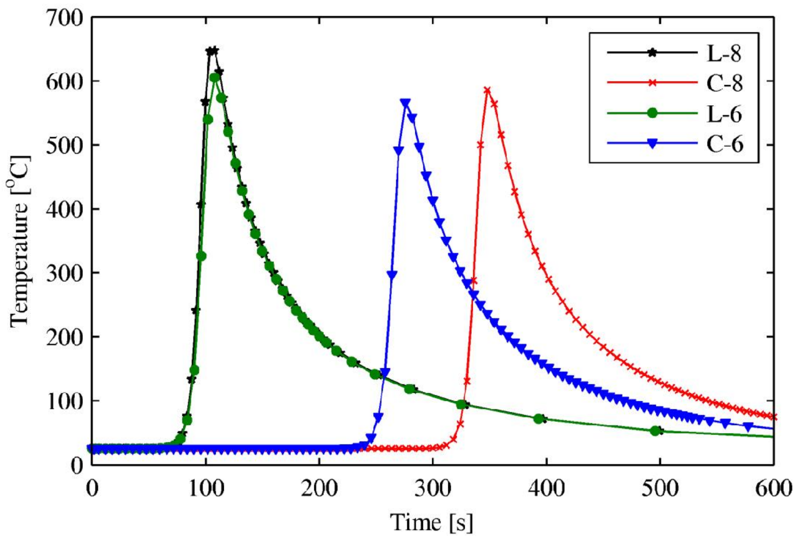

Fig. 5.13 Temperature distributions: Transient thermal cycles at 7.5 mm away from WC.

5.4.2. Residual stress distributions:

In case of C-Seam butt weld joints of cylindrical components, stress normal to the direction of the weld bead is the axial residual stress and the stress parallel to the direction of weld bead is hoop residual stress. Whereas in case of L-Seam butt weld joints of cylindrical components, stress normal and parallel to the direction of weld bead were known as hoop and axial residual stresses respectively. Figs. 5.14 and 5.15 illustrate the contour plots of Von Mises stress distribution for the cases of L-6 and C-6 respectively at element nodes at 10,000 s. Figs. 5.14 and 5.15 depict the maximum Von Mises stresses were 374 MPa and 343 MPa respectively. It was to be noted that the maximum Von Mises stress for L-6 case was higher than C-6 case by 31 MPa.

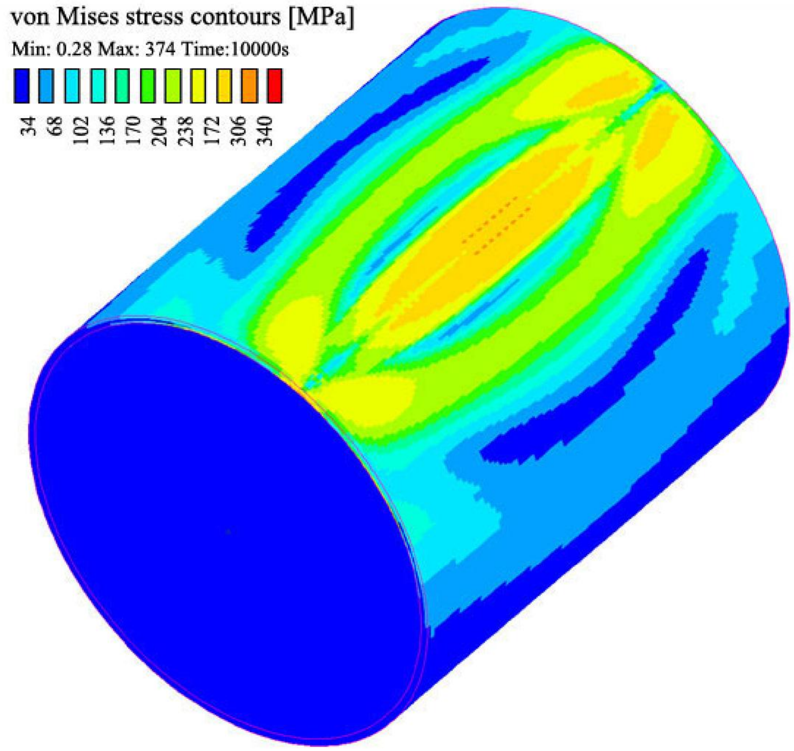

Fig. 5.14 Contours of Von Mises stress for L-6 case of Table 5.2.

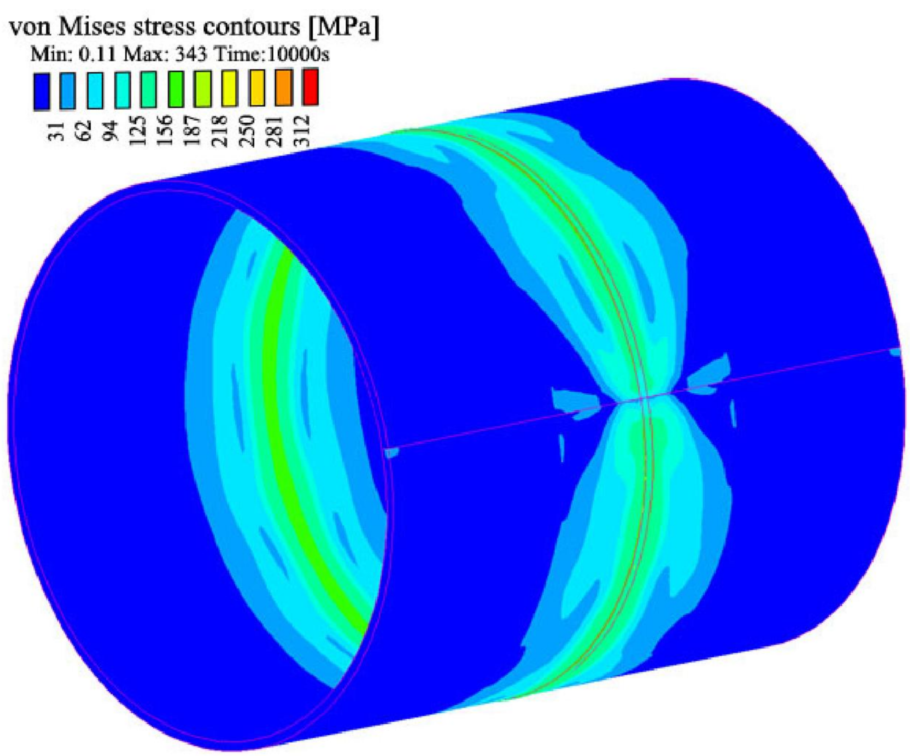

Fig. 5.15 Contours of Von Mises stress for C-6 case of Table 5.2.

Based on the FE simulation, residual stresses in circumferential and longitudinal directions were obtained on the inner and outer surface for the four different cases such as L-8, C-8, L-6 and C-6 as specified in Table 5.2. It was very important to note that these four different FE simulation cases were carried out with the same groove geometry, BC, weld sequencing (progressive welding), wall thickness and the relatively constant heat input between L-Seam and C-Seam butt weld joints of cylindrical components. Figs. 5.16 and 5.17 exhibit the hoop stress distribution on the inner and outer surfaces, respectively at 180^{o} cross-section for C-Seam welds and at 100 mm cross-section for L-Seam welds as described in Section 5.4.1. Similarly, axial stress distribution on the inner and outer surfaces was presented in Figs. 5.18 and 5.19. It should be noted that these stress distributions were along the circumferential and axial distance from the WC line for L-Seam and C-Seam welds respectively as shown in Fig. 5.4. A detailed study was carried out on the above results to understand the influence of L-Seam and C-Seam butt weld joints of cylindrical components on the residual stress distribution and was summarised as follows.

From the simulated results, it can be shown that in the vicinity of weld area, the predicted hoop residual stresses were tensile for L-Seam weld joints on the inner and outer surfaces. Whereas, for C-Seam weld joints, within and near the weld area, tensile hoop stress was observed on the inner surface and on the outer surface it was wavy in nature. From Figs. 5.16 and 5.17, it can also be found that even though the stress profiles on the inner and outer surfaces were similar to some extent, the magnitudes were different among L-Seam and C-Seam weld joints of cylindrical components. The high tensile hoop stresses for L-Seam weld joints on both the inner and outer surfaces at the Weld Location (WL) approaching to zero and then reversing to lower compressive stresses at around 20 mm, again increasing to almost constant value of zero on both sides of WL as shown in Figs. 5.16 and 5.17.

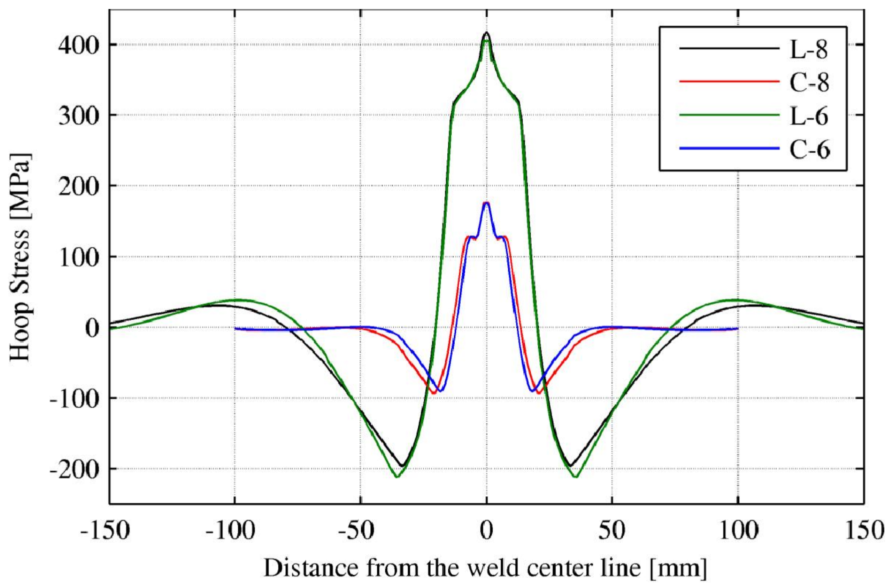

Fig. 5.16 Hoop residual stress distribution for four different cases at the mid plane in the circumferential and longitudinal direction on the inner surface.

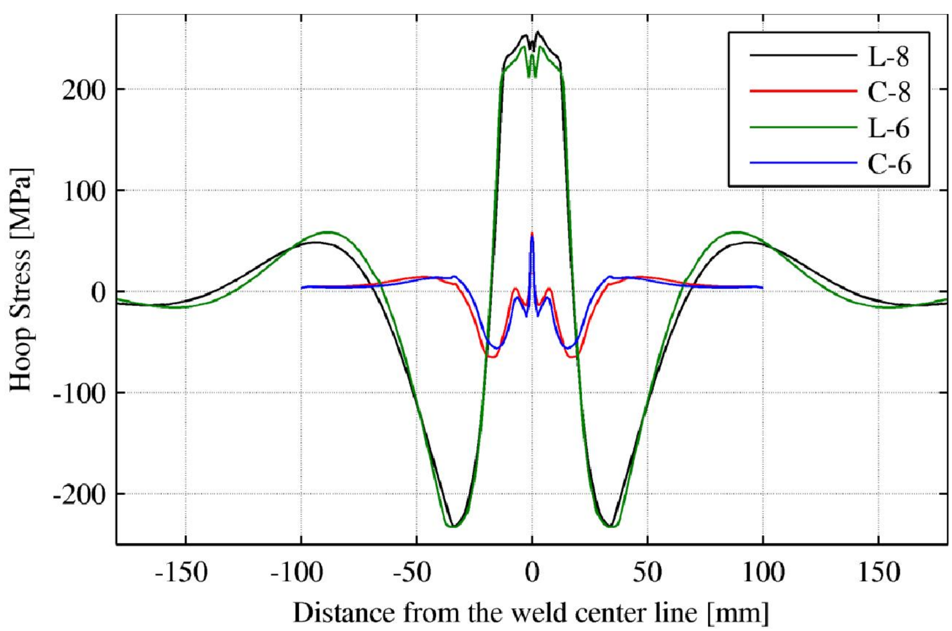

Fig. 5.17 Hoop residual stress distribution for four different cases at the mid plane in the circumferential and longitudinal direction on the outer surface.

Also the tensile hoop stresses for C-Seam weld joints on the inner surface at the WL diminishing to zero at around 13 mm on the both sides of WL. Beyond this the low magnitude compressive stresses again approach to zero value almost 50 mm away from the WL. The observations and trends for hoop residual stresses of C-Seam weld joint seen in this study were found to be in close analogy with the previous research by [38, 46 and 110].

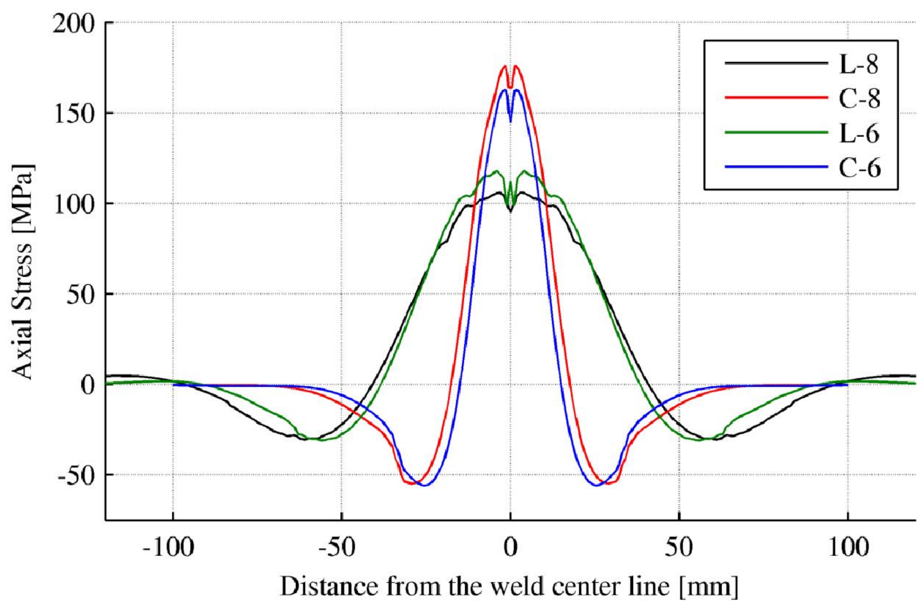

Fig. 5.18 Axial residual stress distribution for four different cases at the mid plane in the circumferential and longitudinal direction on the inner surface.

Figs. 5.18 and 5.19 show that the tensile and compressive axial stresses at the WL on inner and outer surfaces respectively, for both the cases of L-Seam and C-Seam weld joints of cylindrical components. The transition in stress reversal was found to occur at around 16.5 mm and at around 39 mm from the WC for the cases of C-Seam and L-Seam welds, on the inner surface. Whereas it was at 18 mm and around 42 mm for the cases of C-Seam and L-Seam welds on the outer surface. Similar trends of stress distribution and reversal were observed for axial residual stresses of C-Seam weld joint in previous research by [38, 46 and 110]. It indicates that the hoop and axial residual stresses change with respect to L-Seam and C-Seam weld joint on the inner and outer surfaces.

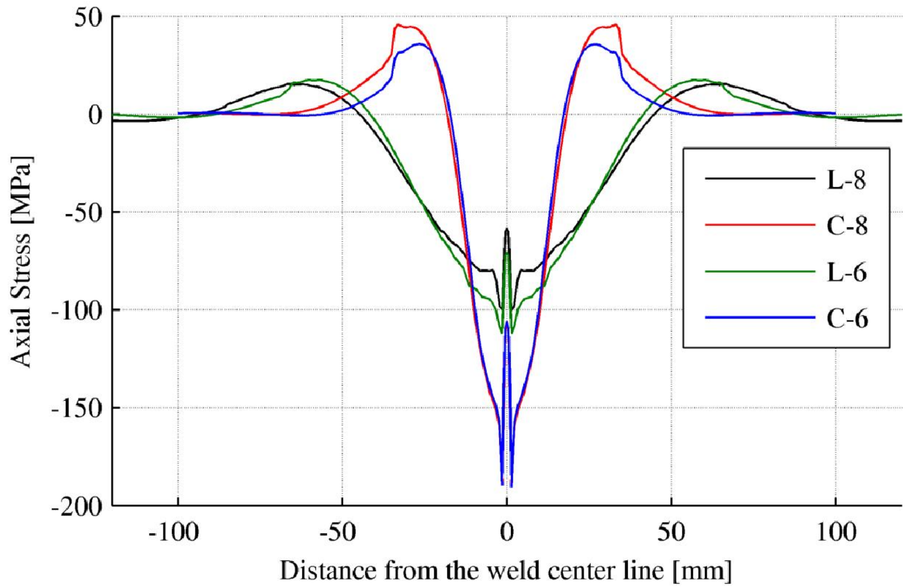

Fig. 5.19 Axial residual stress distribution for four different cases at the mid plane in the circumferential and longitudinal direction on the outer surface.

For the analysis, two different pipe diameters with constant wall thickness and having two different inside radius to wall thickness ratios (R_i/T) of 38.5 and 29.37 were used as shown in Table 5.2. A careful consideration of the results reveals that residual stresses within and near the weld area were slightly increased with increasing the R_i/T ratio. The trend shows close correlation with the previous research by [36].

5.4.2.1. Influence of L-Seam and C-Seam weld joints:

Figs. 5.16 and 5.17 describe that the hoop stress values increase for L-Seam weld joint irrespective of the locations along the distance from WC line. The increase in hoop stresses at the WC was found to be very significant with the increase in tensile stresses as 225 MPa on the inner surface, and 180 MPa on the outer surface. Also, the same increasing trend in compressive stresses was noticed away from the WC line on both inner and outer surfaces of L-Seam weld joint. Further, the results (Figs. 5.18 and 5.19) show that for the case of C-Seam weld joint, axial stresses increase on both the surfaces; and this increase was found to be less significant when compared to hoop stress increase for the L-Seam weld joint. On the inner surface at the WL, the magnitude of increase in tensile residual stresses was approximately 60 MPa; whereas, it was about 80 MPa for compressive stresses on the outer surface.

Based on the results of the residual stresses, the weld residual stress distribution characteristics for the L-Seam and C-Seam weld joints can be described as follows. During the welding process of both the L-Seam and C-Seam joints, the plastic deformation is prone to occur in the WZ and its vicinity. This indicates that on both the surfaces diameter of the component in the weld region reduces after welding. The shrinkage due to welding induces bending moments in addition to axial force, circumferential force and shear force. The schematic representation of expansion and shrinkage in circumferentially welded pipes and the free body diagram of the weld joint were given in the previous study by [119]. Hence, it was very interesting to note that the bending moment was generated in the axial and circumferential directions for C-Seam and L-Seam welds respectively as shown in Fig. 5.20. Therefore, the peak hoop stresses were observed for L-Seam weld joint on both the surfaces. Similarly, the peak axial stresses were observed for C-Seam weld joint.

It is well known fact that when a vessel was subjected to internal pressure, the induced hoop stress was twice in magnitude when compared to axial stress. This hoop stress due to internal pressure adds vectorially with the weld induced hoop stresses. Based on the above observation, it can be concluded that the L-Seam weld joints were not advisable to use while fabricating cylindrical components such as annular tanks, vent pots, waste transfer containers and pressure vessels in order to improve the service life of cylindrical components.

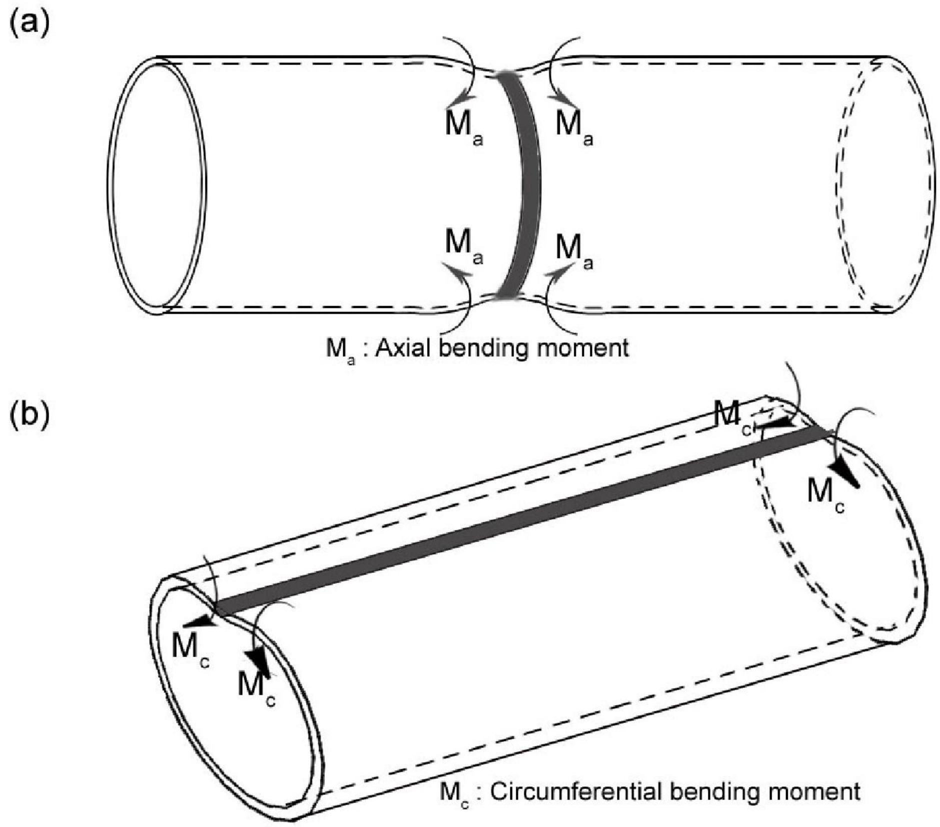

Fig. 5.20 Schematic representations of bending moments: (a) C-Seam and (b) L-Seam.

CHAPTER - 06

WELD CHARACTERISTICS OF N-A BUTT WELDED BP-T-JOINTS

The quantitative characterisation of the residual stress distribution in the vicinity of BP weld joint junctions is quite important; to assess how such stresses will affect the service life and integrity of components, and also to understand the mechanism of development on the evolution and distribution of residual stresses. In this study, welding experiments were performed for the 50 NB: BP-T-Joint in order to validate the developed FE models. Further, 3D sequentially coupled thermo-metallurgical-mechanical analysis method is developed to simulate the GTAW process for joining the different cases of AISI 304L BP-T-Joints in order to capture the thermal and residual stress distributions for the BP welded T-joint. In this investigation, similar wall thickness, BC, weld sequencing (progressive welding), similar welding process and parameters were considered for the two different pipe sizes such as 50 and 150 NB. In-depth analysis is performed to compare the weld temperature characteristics, maximum temperature and weld induced residual stress distributions at different locations and sections for the butt welded BP-T-Joints. Significant differences in 3D temperature profiles, temperature distributions and residual stress states were noticed between run and branch pipes for different pipe sizes along different sections.

6.1. Specimen description and material properties:

The present investigation considers same size run and branch pipes which were joined by N-A GTAW butt welding process. The thickness of both the run and branch pipes was 2.77 mm and their outer diameter was 60.3 mm. Fig. 6.1 shows schematic drawing and relevant dimensions considered in the experimental work. Fig. 6.1 also includes the details of RP, BP, weld bead geometry, thermocouple locations, weld start position, weld direction, etc. The fabrication of BP-T-Joint specimen was divided into two stages. In the first stage, 50 NB-SCH 10 pipe cut into 300 mm and 150 mm long for the preparation of run and branch pipes respectively. During the second stage, cut out was prepared at the middle location of run pipes and end edge cutting was performed on the branch pipes. Further, edge preparation was carried out and both the run and branch pipes were tack welded prior to welding process. The material of construction for both the run and branch pipes was AISI 304L.

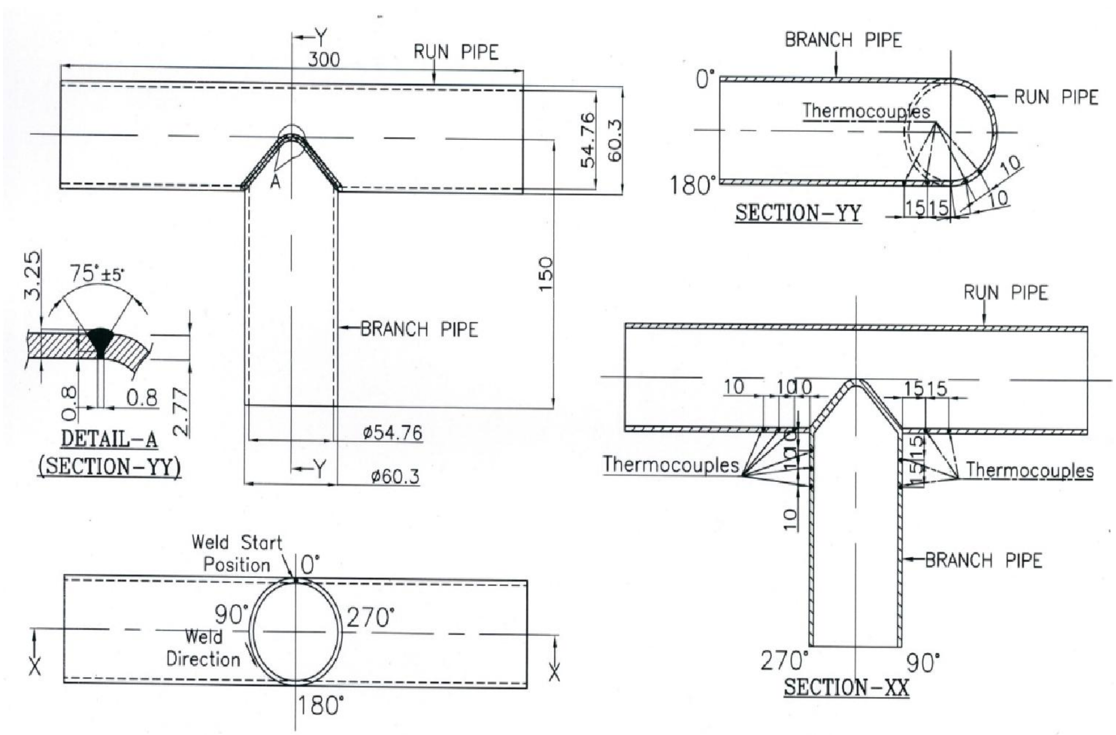

Fig. 6.1 Schematic diagram of BP-T-joint specimen.

In the present work, while performing the weld simulation, temperature dependent material properties of AISI 304L were considered and these were shown in Figs. 3.3 and 3.4. The chemical composition of AISI 304L material used in this study was listed in Table 3.2. The temperature independent material properties and constants which were used in this investigation were specified in Table 3.1 and described in the Section 3.5.2. During this analysis, the initial temperature of both the run and branch pipes was considered at 25^0C.

6.2. 3D model and FE mesh:

3D geometrical models of 50 and 150 NB: BP-T-Joint assemblies were created prior to the FE mesh generation. For instance, the 3D model of the 50 NB branch pipe joint was shown in Fig. 6.2. The dimensions of the simulation model and for experiments were same except length of pipes and these were shown in Fig. 6.1. For the 50 NB simulation case, the length of RP was 200 mm and the length of BP was 100 mm. The reduction in pipe lengths when compared to experiments was to reduce the computational time and cost. Whereas, for the case of 150 NB simulations, the length of RP was 400 mm and BP was 200 mm.

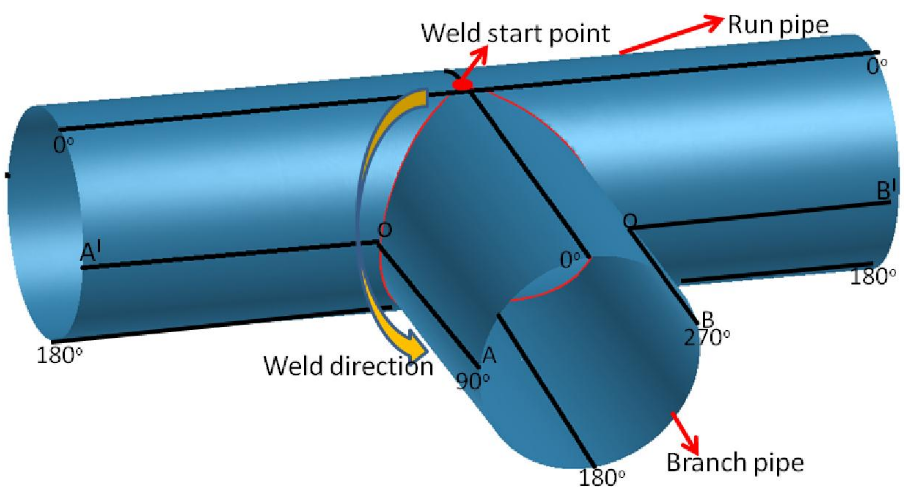

Fig. 6.2 3D model of the 50 NB: BP-T-Joint.

During FE meshing, two types of elements were used such as 1D linear elements and Quad-Tria layered elements. The Quad-Tria layered elements were also called as 3D shell elements with no thickness. 1D linear elements were used to represent weld trajectory line. Element sizes of 2 mm for 50 NB and 3 mm for 150 NB were used for 1D linear elements along the trajectory line. Quad-Tria layered elements were used to mesh the both run and branch pipes as surfaces with no thickness. The material wall thickness i.e. 2.77 mm was mentioned while specifying the material properties for both the 50 and 150 NB: BP-T-Joints. The complete FE mesh with 1D linear elements and Quad-Tria elements after meshing weld trajectory line and branch pipes were shown in Fig. 6.3(a) and (b). The Quad-Tria layered element size was 2 mm and 3 mm for 50 NB and 150 NB branch pipes respectively and these were kept constant throughout its RP and BP lengths. In order to justify the simulation time and the accuracy of results course mesh was used with the element size of 3 mm in the 150 NB case compared to 50 NB branch pipe analyses. It can be observed from Fig. 6.3(a) and (b) that the BP-T-Joint surface mesh consists of combination of both the quadrilateral and triangular shaped elements. The quadrilateral element has 4 nodes, triangular element has 3 nodes and each node has three translational and three rotational degrees of freedom. For both the thermal and mechanical analysis same element types were used. The welding arc travel direction and welding start point were shown in Fig. 6.2. Also the nomenclature used in this study i.e BP-0^0, BP-90^0, BP-180^0 and BP-270^0; and RP-0^0 and RP-180^0 were mentioned in Fig. 6.2.

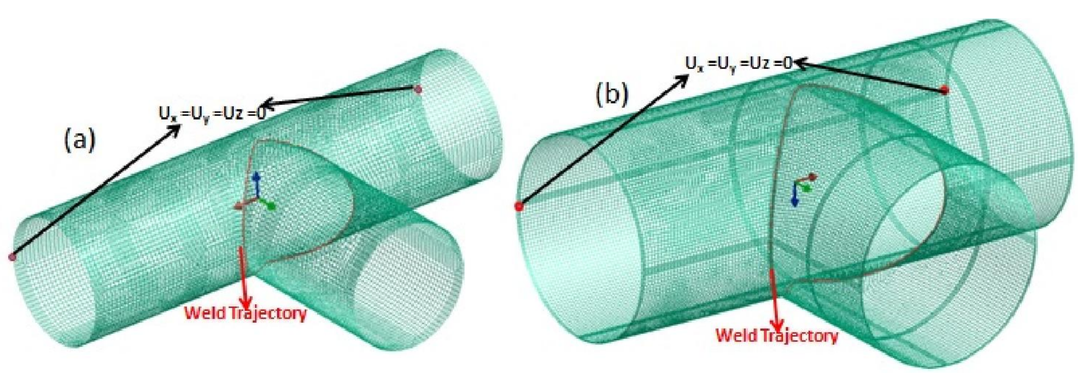

Fig. 6.3 FE mesh of BP-T-Joint: (a) 50 NB and (b) 150 NB.

6.3. Heat source modeling and FE simulation:

The energy input with the weld speed of 1 mm/s for both 50 and 150 NB branch pipe joint cases was 375 J/mm and these were further illustrated in Table 6.1. In order to obtain the proper FZ for the considered pipe sizes, the Gaussian parameters for the double ellipsoid heat source were taken as $a_f = 1$ mm, $a_r = 4$ mm, $b = 0.75$ mm and $c = 0.9$ mm. The front (q_f) and rear (q_r) volumetric heat flux densities (w/mm^3) were attained as $q_f = 15.76$ w/mm^3 and $q_r = 63.07$ w/mm^3 respectively based on the considered weld parameters and Gaussian parameters for both the 50 and 150 NB cases. The above described values of the parameters were also similar to the values considered in the previous study of comparison of weld characteristics between L-Seam and C-Seam butt weld joints of cylindrical components for the 2.77 mm thick pipe. The results obtained for the double ellipsoidal heat source model which moves along the weld trajectory was saved to an in-built function database for further use in the prediction of thermal and stress fields during welding process simulation. In the first step, the temperature history was computed by the heat conduction analysis. The second step of the current analysis involves the use of temperature histories predicted in the previous thermal analysis as an input for a mechanical analysis.

Table 6.1 Different FE simulation cases.

Case	Pipe size	Pipe O.D and wall thickness (mm)	Weld power= V×I (W)	Heat input (J/mm)	Inner radius to wall thickness ratio (R_i/T)
1	50 NB-SCH 10	60.3 and 2.77	375	375	9.88 **(Thick Cylinder)**
2	150 NB-SCH 5	168.2 and 2.77	375	375	29.36 **(Thin Cylinder)**

During weld experiments, both the branch and run pipes were not constrained. Hence during numerical simulation, for the FE model, minimum constraints were applied as the artificial boundary condition in order to prevent rigid body motion and to match the experimental BC. The details of BC used for the cases of 50 NB and 150 NB branch pipe weld joint simulations were shown in Fig. 6.3. For both the cases, two nodes which were away from the weld joint were constrained in X, Y and Z directions. These BC do not affect the stress magnitudes for the branch pipe N-A weld joint simulation.

6.4. Experimental procedure and validation of numerical models:

Numerical simulation methodology was one of the potential technique to predict and obtain weld induced residual stress distributions and distortions for all types of complex engineering structures. However, prior to a numerical simulation approach was used to predict weld characteristics, related FE models shall be validated with experiments.

6.4.1. Experimental procedure:

The results obtained from FE simulation of 50 NB: BP-T-Joint were validated with GTAW experiments with the similar geometric dimensions and weld bead geometry as shown in Fig. 6.1. For all the experiments, AISI 308 was used as a filler material having diameter of 1.6 mm and argon was used as shielding gas. Fig. 6.4 shows the experimental weld setup used for the 50 NB: BP-T-Joint with the data acquisition system connected with thermocouples. In the welding process, amount of heat input plays an important role and it mainly depends on the base metal thickness, melting point and its thermal conductivity. In this study, for the welding of 50 NB-SCH 10: BP-T-Joint, 55 A current and 10 V voltage, 1 mm/s weld speed were considered. In order to validate the heat input that was used in this investigation, macroscopy was obtained for 50 NB: BP-T-Joint at transverse section of the weld sample. The transverse section for the macrograph was taken approximately at 45^0 from the weld start position. The cut piece of the weld sample was ground and polished up to 3 micron finish and etched in 2% Nital solution to measure the experimental weld pool shape.

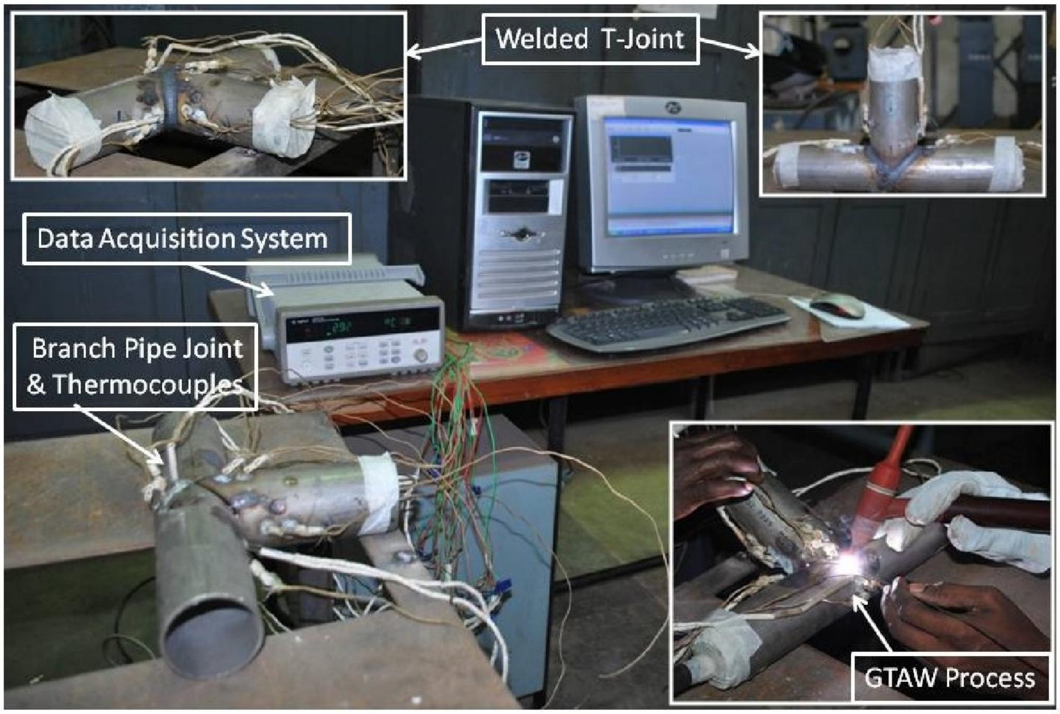

Fig. 6.4 Experimental weld setup for the 50 NB BP-T-Joint.

The macrograph of the weld molten pool shape for the 50 NB: BP-T-Joint was shown in Fig. 6.5. It could be seen that the experimental macrograph cross-section dimensions were in good agreement with the weld groove dimensions which were shown at 'Detail-A' of Fig. 6.1. The above mentioned process parameters with a GTAW arc efficiency of 0.7 gives the weld heat input per unit length was 375 J/mm. It can also be observed that in the previous study of comparison of weld characteristics between L-Seam and C-Seam butt weld joints of cylindrical components used same amount of heat input for the 2.77 mm thick ASS. Hence, in this investigation for FE simulations, 375 J/mm weld heat input was considered for 1 mm/s weld speed. Transient temperatures were measured using Chromel-Alumel (K-type) thermocouples connected at different locations on the outer surface of BP-T-

Joint by using silver brazing. The transient thermal cycles were recorded for every one second time interval. The location of thermocouples at 90^0, 180^0 and 270^0 from the weld centre (WC) on both the RP and BP were shown in Fig. 6.1. For the validation of residual stresses with numerical simulations, XRD technique was employed for measuring the residual stresses on the BP-T-Joint external surface. In this technique, the estimated strains which were measured by the shift in the position of diffraction peak were then converted into stresses [110].

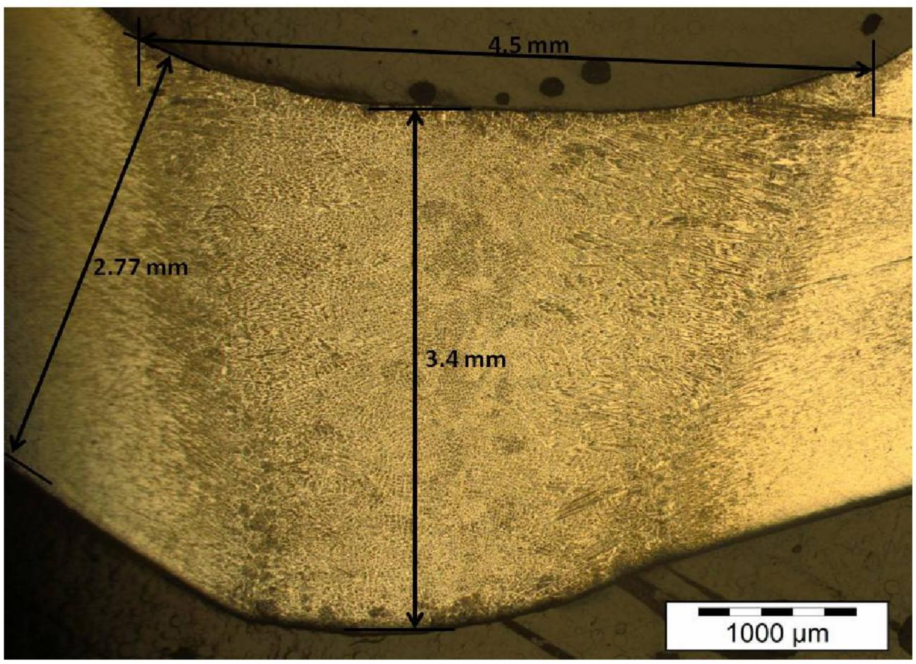

Fig. 6.5 Experimental macrograph of the weld molten pool.

6.4.2. Comparison between experiments and numerical simulations:

Welding induced residual stresses and distortions can result directly from the non-uniform temperature distribution and they were highly sensitive to the transient thermal cycles. Hence, an accurate welding simulation process was an important pre-requisite that ensures the reliability of FE weld models. In this investigation, to validate the reliability of N-A butt welded BP-T-Joint FE weld models for the temperature profiles and weld induced residual stresses, both the transient temperatures and residual stresses from the FE simulation were compared with the experimental measurements. The comparisons of the temperature profiles between the experimental measurements and 3D numerical simulations for the 50 NB: BP-T-Joint at different thermocouple locations were plotted in Fig. 6.6. Fig. 6.6(a) shows the temperature distributions for the 90^0 and 270^0 sections, and the temperature distributions for the 180^0 section was recorded as shown in Fig. 6.6(b). It was important to emphasize that the experimental data presented correspond to particular thermocouple locations. The locations were at 15 mm away from the WC on the both RP and BP for the 90^0 section. The locations at 10 mm on the BP and 20 mm on the RP for the 270^0 section were shown as section ‘XX’ in Fig. 6.1. Whereas, for the 180^0 section, 10 and 20 mm on the RP and 15 mm on the BP were considered and as shown in section ‘YY’ of Fig. 6.1. It could be noticed that the simulation results and experimental measurements show a good agreement at locations 15 mm for the 90^0 section. From Fig. 6.6(a), the locations at 10 and 20 mm for the 270^0 section variations were observed and were reasonably comparable. Whereas, at the locations 10 and 20 mm for the 180^0 section on the RP, the experimental measurements were marginally higher than that of simulation results. The differences in peak temperatures between experiments and 3D numerical simulations were observed to be 11.8%, 10.4% and 14.4% at 270^0 section-20 mm, 180^0 section-10 mm and 20 mm respectively as shown in Fig. 6.6(a) and (b). The possible reason for the variations was envisaged that during experiments the thermocouple locations were taken exactly at 10, 15 and 20 mm from the WC line and for the simulations these locations were not exactly at the above indicated points. For instance, during FE meshing, node was generated involuntarily at 20.6 mm location in place of 20 mm for the 270^0 section and was shown Fig. 6.6(a). Similarly, for the 180^0 section, nodes were generated at 10.5 and 20.8 mm in place of 10 and 20 mm respectively. This could be the probable cause for the marginal increase in experimental peak temperature when compared with the simulation results. The trends for the comparison of the temperature distributions between the experiments and numerical simulations were concur well with the results by the previous researchers [54, 110, 120]. The rate of increase in temperature was in correspondence with each other. However, during weld cooling the experimental measurements were slightly higher than that of simulation results and this could be due to the heat losses during experiments were different from those predicted by the simulation. From Fig. 6.6(b), for the 180^0 section, it was important to notice that the peak temperature at 15 mm on the BP was greater than the peak temperature at 10 mm on the RP. The possible reason for such an observation could be that on the outer surface the temperature gradients of elliptical shaped temperature profiles covers more surface area over the BP than the RP. This was due to dissimilar geometrical conditions on the both sides of the WC line at 180^0 section. The 3D temperature profile on the outer surface obtained for BP-T-Joint was described from the Fig. 6.9(a) in the Section 6.5.1.

The hoop and axial stresses were measured at different locations on the outer surface along the 180^0 line of the BP and along the 180^0 line of the RP. The 180^0 line on the RP and BP of 50 NB T-joint was shown in Fig. 6.2. Along the BP-180^0 section line, the locations were at the WC, at 6 mm away from the WC on the RP and at 5, 10 and 20 mm away from the WC on the BP. Along the RP-180^0 line, hoop stresses were measured at five different locations, viz. at WC and at 10 and 20 mm away from the WC on the both sides of the weld. The measurements along the BP-90^0 and 270^0 lines (i.e. along AOA[1] and BOB[1] lines) were practically not possible to carry out and therefore the measurements were not performed along these lines.

(a)

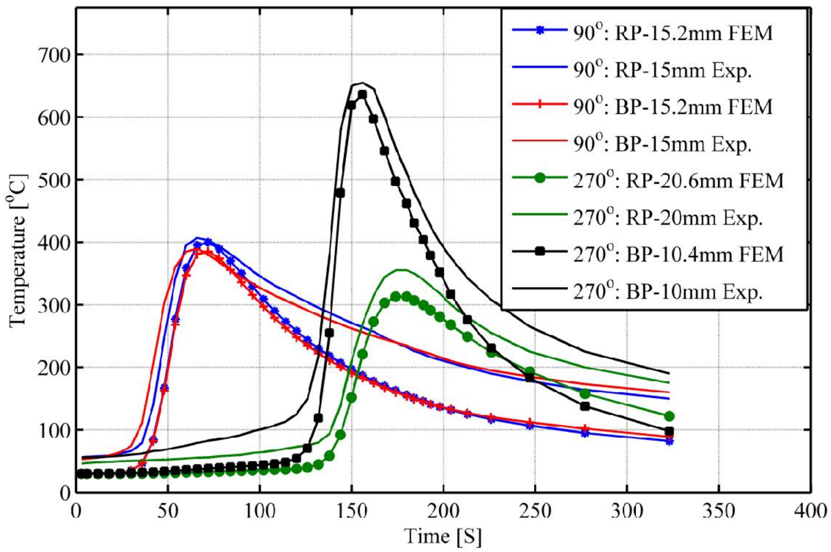

(b)

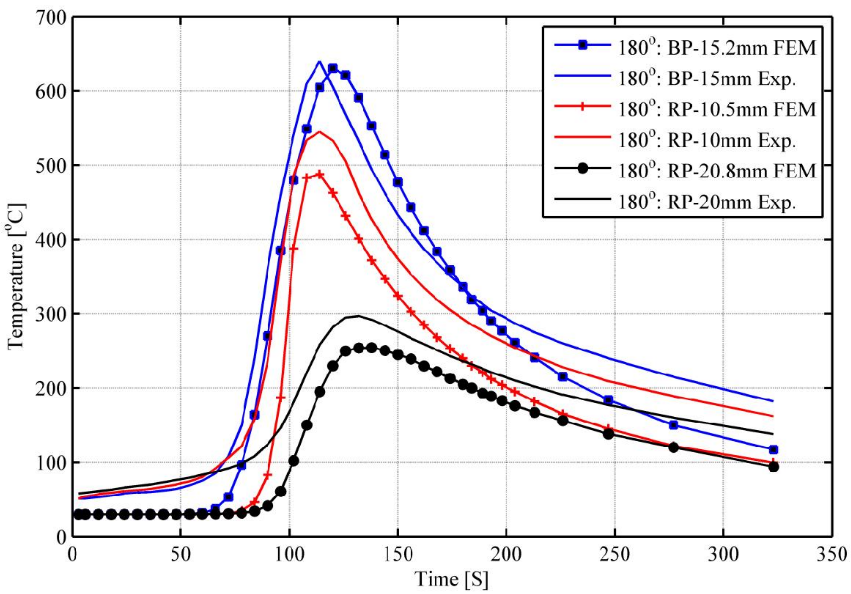

Fig. 6.6 Comparison between predicted and measured transient temperature profiles at different locations: (a) Along 90^0 and 270^0 and (b) Along 180^0.

The experimental measurements along with those from numerical simulation results were plotted in Fig. 6.7 with error bars for the experimental data. The location, i.e. at the WC along the BP-180^0 line, numerical simulation results were not indicated and the reason for the non availability of the results was described in the Section 6.5.2. Hence, for the cases of hoop and axial along the BP-180^0 line by the FE simulation discontinuity was plotted at the WC. It could be noticed that the results of hoop and axial stress measurements for the locations along the BP-180^0 line were in reasonable agreement with each other in addition to the close match of trend. Meanwhile, Fig. 6.7 also indicates that the hoop stresses for the locations along the RP-180^0 line have slight discrepancies on the both sides of the weld. However, both the FE simulation results and the experimental measurements have a similar increasing and decreasing trend on the both sides with in the WZ and its vicinity. The experimental results suggest that initial residual stresses were introduced by the machining process during edge preparation.

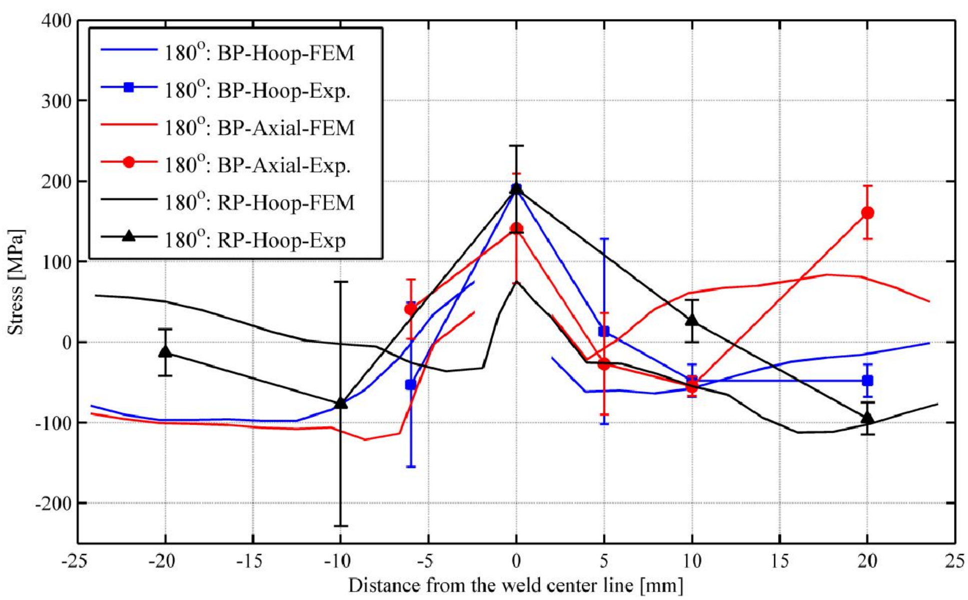

Fig. 6.7 Validation of numerical simulation residual stresses and the experimental measurements.

Overall, although the initial residual stresses which were generated due to manufacturing process and the machining before welding were not considered in the numerical simulations, the developed FE models predict a good result.

6.5. Simulation results and discussions:

This section deals with the corresponding results of thermal and mechanical analysis acquired through the numerical simulations for the 50 and 150 NB N-A butt welded BP-T-Joint cases as shown in Table 6.1. During simulations the weld speed was considered as 1 mm/s and the simulation was run for a time period of 4,000 s. The weld temperature characteristics and residual stress distributions obtained from the analysis were described in the following sections.

6.5.1. Temperature history:

The 3D distributions of temperature fields predicted on the outer surface for the 50 and 150 NB simulation cases were shown in Figs. 6.8.(a)-(c) and 6.9.(a)-(c) respectively. Figs. 6.8 and 6.9 also present the weld trajectory and direction which was used in the FE simulation models of the BP-T-Joints. The contours of temperature profiles were shown at 60, 189 and 205 s for 50 NB and at 330, 450 and 904 s for 150 NB: BP-T-Joints. These different time segments were considered to show the temperature distributions of the BP-T-Joints at various locations in the welding direction. The elliptical shaped temperature distributions were observed on the external surface of the component. The same profiles and trends were observed in the previous research by [110, 111]. With the moving heat source model during GTAW process, the cooling rate was different at various points on the model.

(a)

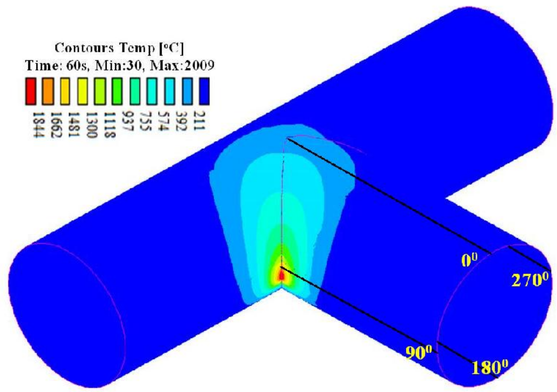

(b)

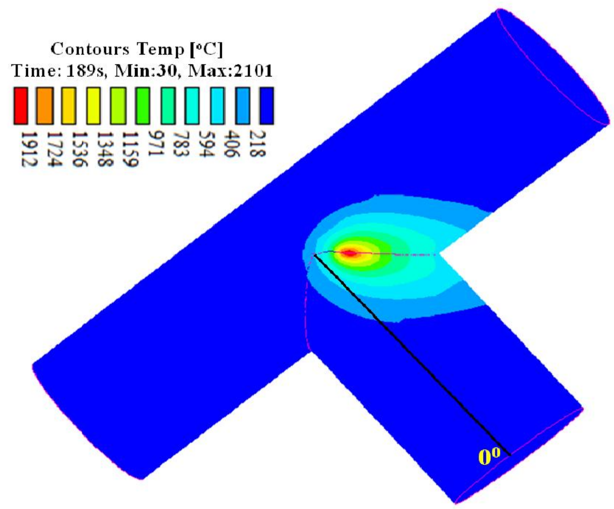

(c)

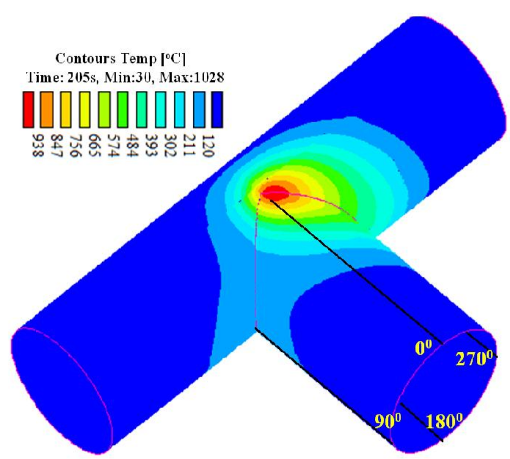

Fig. 6.8 3D temperature profiles on the outer surface: (a) 50 NB at 60 s (b) 50 NB at 189 s and (c) 50 NB at 205 s.

(a)

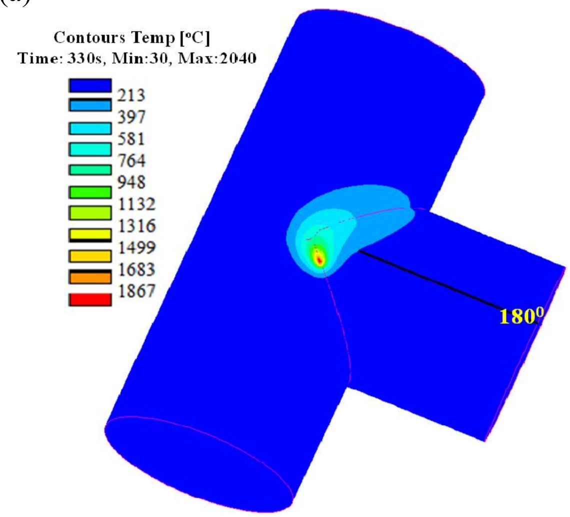

(b)

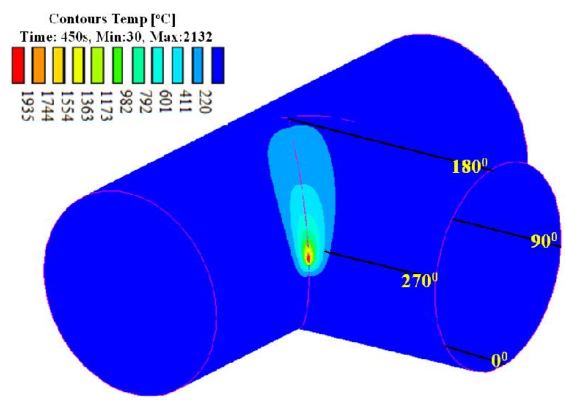

(c)

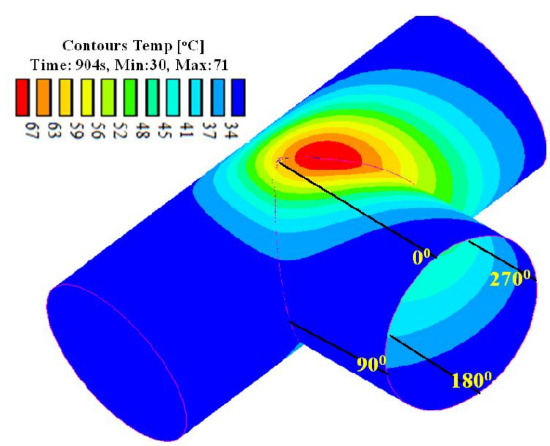

Fig. 6.9 3D temperature profiles on the outer surface: (a) 150 NB at 330 s (b) 150 NB at 450 s and (c) 150 NB at 904 s.

As shown in Figs. 6.8(c) and 6.9(c), after completion of welding process, the temperature distribution of FE model gradually become stable to room temperature followed by some more time steps further simulating the cooling phase. As anticipated, the peak temperature during welding was within the FZ and has the value above 2000^0C, which was much higher than the melting temperature (i.e. 1450^0C) of AISI 304L. It was apparent that the weld torch preheats a very small area in front of the torch where the heat source is going to pass. The heat input generated by the heat source model along the weld trajectory was uniformly transferred in all the directions except when the weld torch passes the 180^0 section from the weld start point as shown in Fig. 6.9(a). The probable reason for this observation was due to dissimilar geometrical conditions on the both sides of the WC line (i.e. the geometry of RP and BP).

Figs. 6.10-6.13 depict the temperature distributions on the outer surface for the 50 and 150 NB: BP-T-Joint simulation cases at the BP-90^0, 180^0 and 270^0 section lines as shown in Fig. 6.2. Results pertaining to temperature versus distance from the WC line on the both run and branch pipes were illustrated in Fig. 6.10. In the Fig. 6.10, negative and positive coordinates represent the distances from the WC line along the RP and the BP respectively. It was very important to note that at the 90^0 and 270^0 section lines temperature distributions were quite similar on the both run and branch pipes for the both 50 and 150 NB cases. Whereas, at the 180^0 section from the weld start position, noticeable difference in temperature distributions were observed in between run and branch pipes and it was shown in Fig. 6.10. It should be noted that the temperatures on the BP were almost 200^0C higher than the RP temperatures for the locations 10 mm away from the WC line. The similar discrepancy in temperature distribution between RP and BP at 180^0 section was also found during experimental measurements and it was shown and described in Fig. 6.6(b) and Section 6.4.2. This can be explained by the fact that the different geometries on the both sides of the WC line at 180^0 section from the weld start position. This can also be observed in the distribution of elliptical shaped temperature profiles at 180^0 section on the outer surface as shown in Fig. 6.9(a).

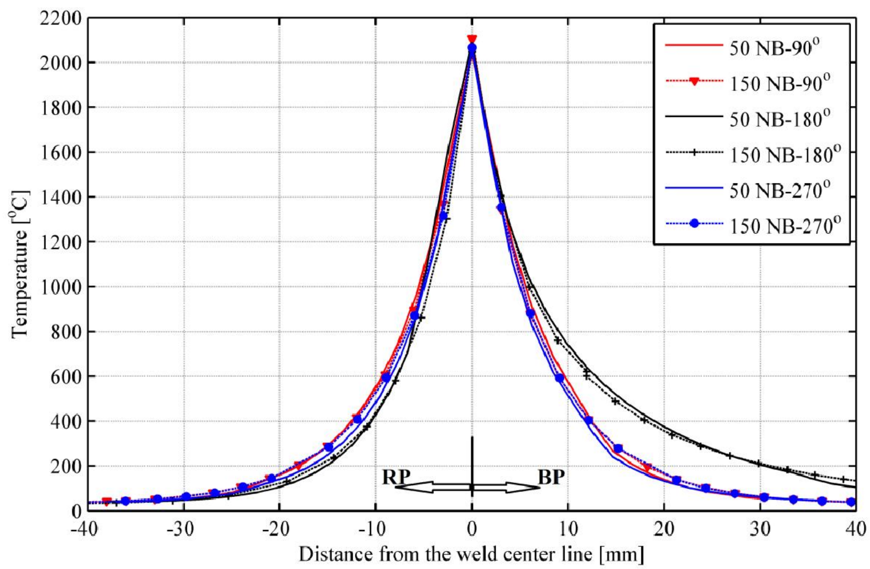

Fig. 6.10 Temperature distributions: Vs distance from the WC line on the RP and BP.

Fig. 6.11 compares the transient thermal cycles at the WC for the 50 and 150 NB cases along the BP-90^0 and 270^0 section lines (i.e. along AOA^l and BOB^l lines) from the weld start position as shown in Fig. 6.2. The thermal cycles show that peak temperature points correspond to times when the weld torch crosses the corresponding section. Fig. 6.12 shows the transient thermal cycles along the 180^0 section line at the WC for the both 50 and 150 NB cases, for the locations at 14.3 mm on the 150 NB-RP and at 14.9 mm on the 150 NB-BP. It was also evident from Figs. 6.11 and 6.12 that at 90^0 and 270^0 sections from the weld start positions, peak temperatures for 150 NB case was higher than the 50 NB case and vice versa at 180^0 section. The similar phenomenon can also be observed in 3D temperature profiles as shown in Figs. 6.8 and 6.9. Also, it was very important to notice that the peak temperature at 14.3 mm on the 150 NB-RP was less than that of at 14.9 mm location on the 150 NB-BP and it was shown in Fig. 6.12. The peak temperature at 14.3 mm on the RP was 396^0C and at 14.9 mm location on the BP it was 632^0C. The reason for the discrepancy of the peak temperature at almost same locations from the WC line was also described from Fig. 6.6(b) in the Section 6.4.2.

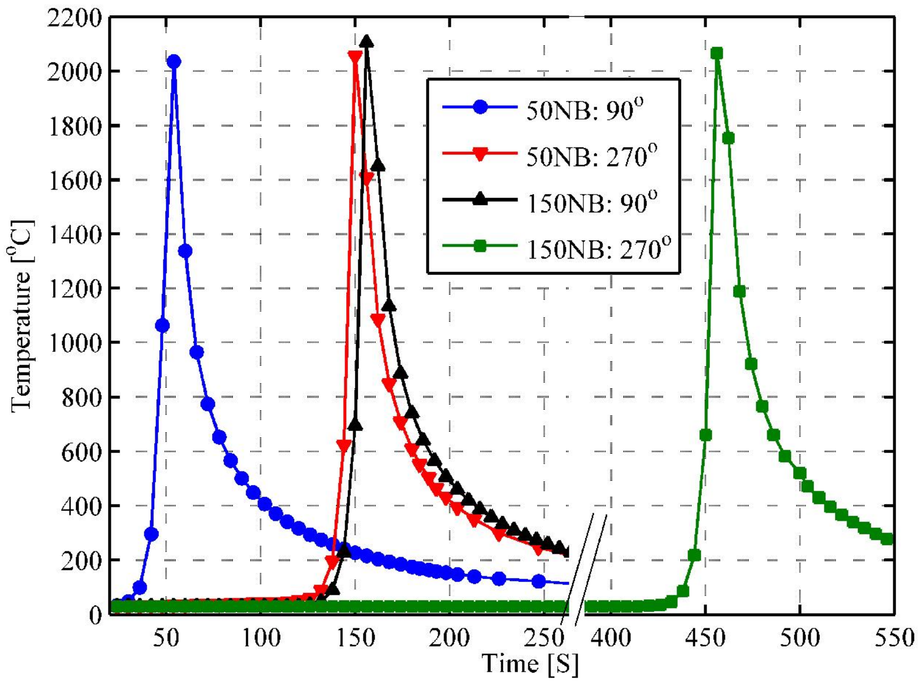

Fig. 6.11 Transient thermal cycles at the WC.

Fig. 6.13 illustrates the transient thermal cycles at the locations 9 mm away from the WC for the 150 NB case along the 90^0 and 270^0 section lines (i.e. along AOA^1 and BOB^1 lines) from the weld start position. From the figure, it was very clear that the temperature histories at the location 9 mm away from the WC line where θ was 90^0 were slightly lower than those at the corresponding location where θ was 270^0 on the both run and branch pipes. Fig. 6.13 also confirms that the temperature distributions were very similar on the both run and branch pipes at 90^0 and 270^0 sections from the weld start position. Therefore, it can be concluded that the temperature distributions were very steady when the weld torch moves along the BP-T-Joint weld trajectory.

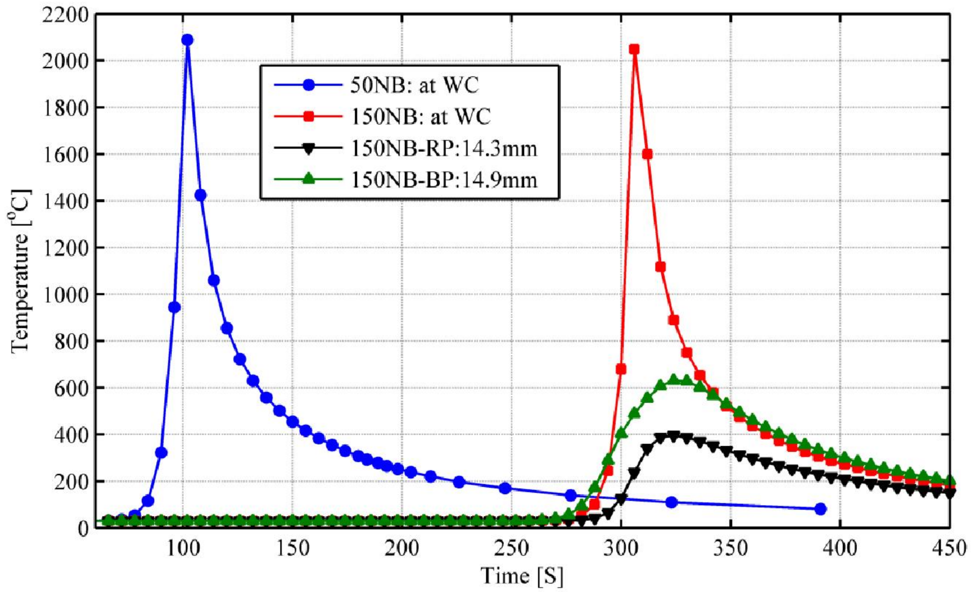

Fig. 6.12 Transient thermal cycles along the BP-180^0 section.

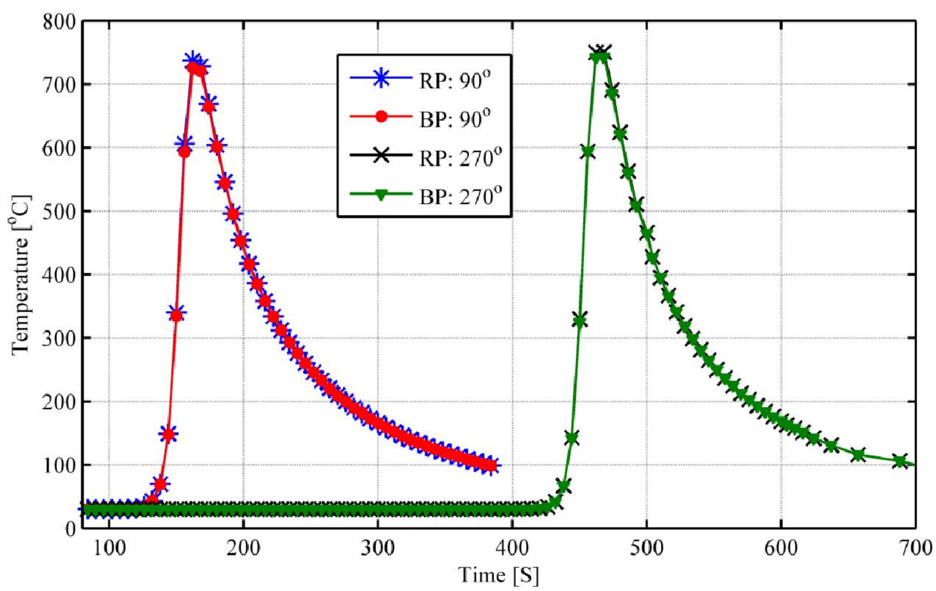

Fig. 6.13 Transient thermal cycles for 150 NB at 9 mm away from the WC.

6.5.2. Weld induced residual stresses:

Figs. 6.14(a) and (b) illustrate the contour plots of Von Mises stress distribution for the N-A butt welded BP-T-Joint of 50 and 150 NB cases respectively at element nodes at 4,000 s on the middle surface. Through careful observation of these figures, it can be observed that the Von Mises stress distributions at the weld S/E location and its vicinity were slightly different from the other locations. Except at the weld S/E location, the stress around the weld direction almost has a homogeneous distribution. The reason for the discrepancy in stress distribution between weld S/E location and the other locations can be that the weld S/E location experiences two thermal cycles. Figs. 6.14(a) and (b) show the maximum Von Mises stresses were 325 MPa and 360 MPa respectively. It was to be noted that the maximum Von Mises stress for 150 NB: BP-T-Joint cases was higher than 50 NB case by 35 MPa.

In this section, results were presented for the investigation of weld induced residual stresses in the 50 and 150 NB: BP-T-Joint cases on the inner, middle and outer surfaces by using the FE procedure demonstrated in the Section 6.3. To portray welding residual stress distributions in order to examine the 3D effects (i.e. circumferential variations of residual stresses) and the influence of R_i/T ratio, different sections and locations were considered. The different locations which were used in this study were along the BP-0^0, 90^0, 180^0 and 270^0 section lines and along the RP-180^0 section line as shown in Fig. 6.2. Based on the numerical simulations, residual stresses in the hoop, axial and radial directions were obtained and compared for different cases at different locations were given in Figs. 6.15-6.20.

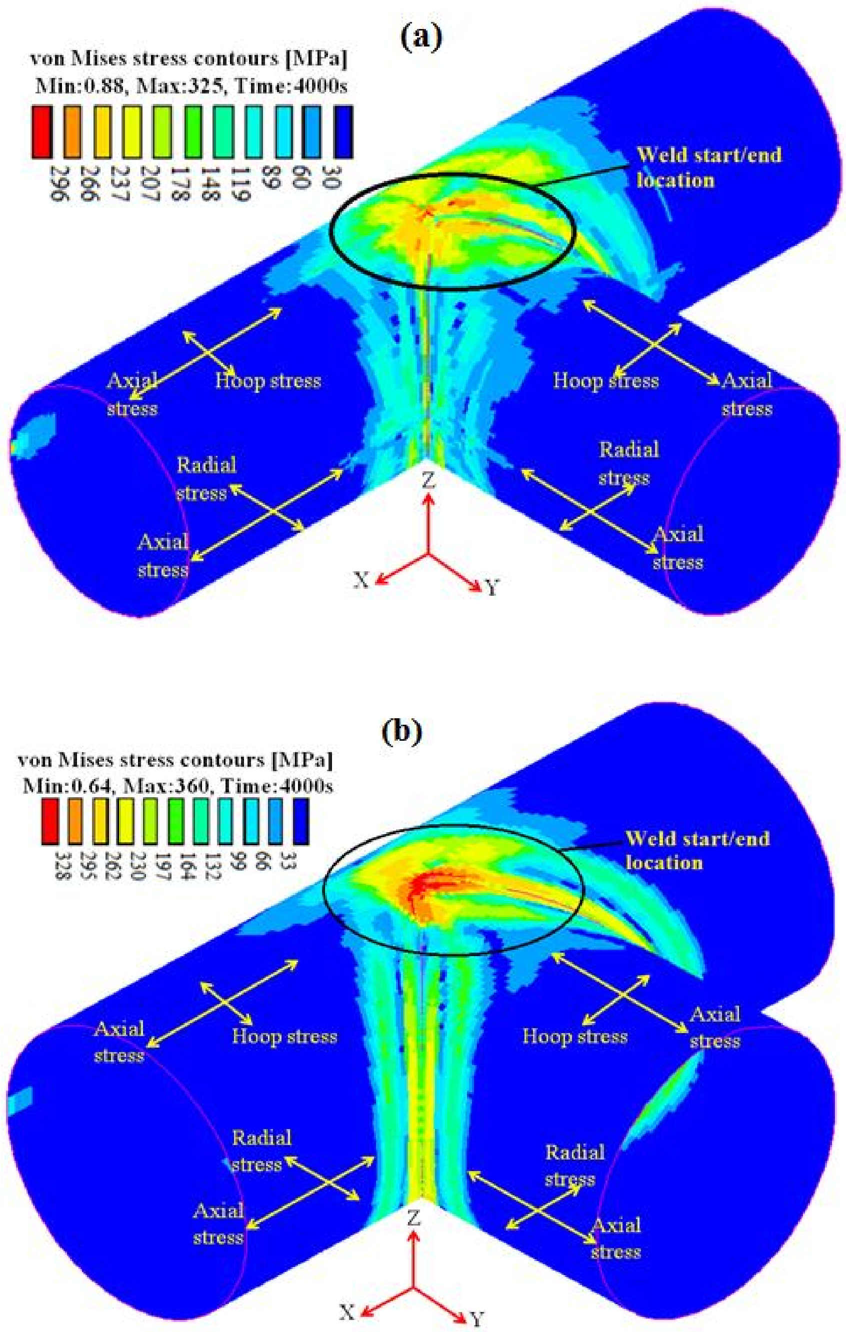

Fig. 6.14 Contours of Von Mises stress: (a) 50 NB and (b) 150 NB pipe T-joint.

Each figure from 6.15-6.20, has its own significant importance to describe the salient features of this research work. In case of BP welded T-joints, stress directions were different for run and branch pipes. For instance, different stress directions for the RP and BP along 0^0 and 90^0 section lines were shown in Figs. 6.14(a) and (b). These figures illustrate that stress directions were different for the corresponding stress components. From Figs. 6.15-6.19, it was very important to note that the stresses at the WC were not shown and the reason for this was described as follows. During the BP-T-Joint simulation, it can be observed that the WC line was the intersection line of the RP and BP. Therefore, the stresses at particular node along the WC line denote for the RP or BP cannot be defined. For example, a node at the weld start location gives the stresses in all the three (X, Y and Z) directions. The stress component along the x direction indicates both the axial stress for the RP and hoop stress for the BP. Hence, for the Figs. 6.15-6.19, stress magnitudes were not represented at the WC. Whereas, for the Fig. 6.20, stress magnitudes were also shown at the WC because it shows stress distributions along RP-180^0 section line. Along RP-180^0 section line, stress in X, Y and Z directions indicate clearly axial, hoop and radial stresses respectively for the RP. In the Figs. 6.15-6.19, negative and positive coordinates represent the distances from the WC line along the RP and the BP respectively.

Figs. 6.15(a) and (b) depicts the both hoop and axial stress distributions on the outer and inner surfaces respectively along BP-90^0 section line (i.e. along AOA^l) for the cases of 50 and 150 NB pipes. Figs. 6.16(a) and (b) qualitatively compares the both hoop and axial stress distributions on the outer and inner surfaces respectively along BP-270^0 section line (i.e. along BOB^l) for the cases of 50 and 150 NB pipes on the run and branch pipes. From Figs. 6.15(a) and 6.16(a), at the WZ and its vicinity, both the hoop and axial stresses were tensile on the RP and compressive on the BP for the 150 NB case. Whereas, it was opposite for the 50 NB case. Similarly, from Figs. 6.15(b) and 6.16(b), at the WZ and its vicinity, both the hoop and axial stresses were compressive on the RP and tensile on the BP for the 150 NB case. Whereas, it was opposite for the 50 NB case.

(a)

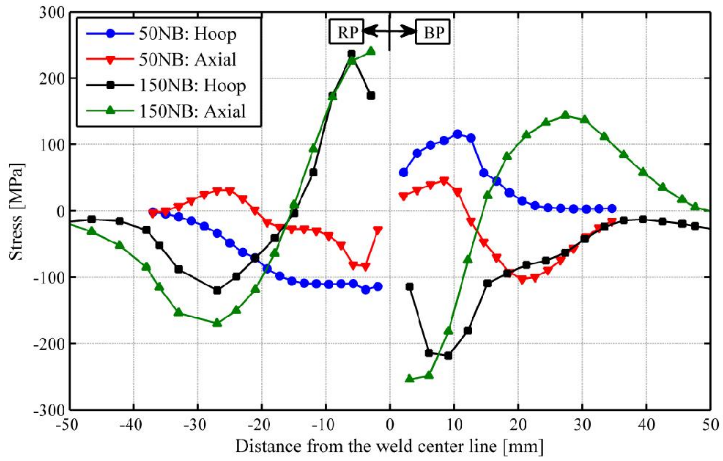

(b)

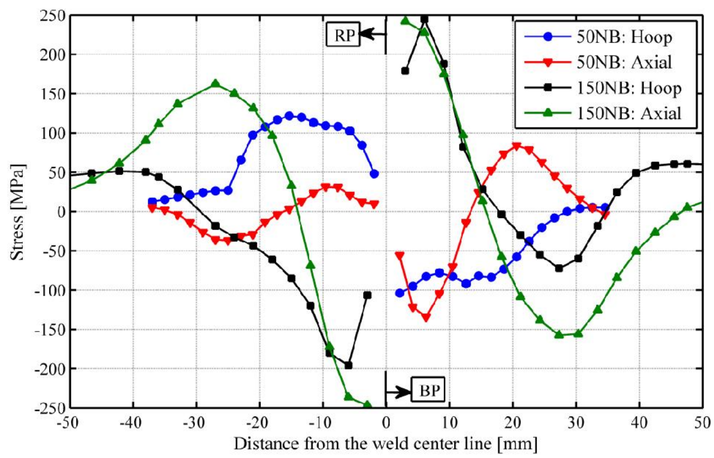

Fig. 6.15 Hoop and axial residual stress distributions for 50 and 150 NB cases along the BP-90^0 section line: (a) On the outer surface and (b) On the inner surface.

Above observations, clearly reveal that both the hoop and axial stress distributions portray reverse trend in between RP and BP along the both 90^0 and 270^0 section lines. Also the reverse trend was noticed in the corresponding stress distributions between 50 and 150 NB cases on the both outer and inner surfaces along the both 90^0 and 270^0 section lines as shown in Figs. 6.15 and 6.16. The high tensile hoop and axial stress for 150 NB case on the RP outer surface at the weld location (WL) change over to compressive stress at around 15 mm, again increasing to almost a constant value of zero as shown in Figs. 6.15(a) and 6.16(a). Also, the reverse trend in stress distribution was observed for 150 NB case on the BP outer surface. The simulation results shown in Figs. 6.15 and 6.16 clearly demonstrate that both the hoop and axial stress magnitudes were different between BP-90^0 and 270^0 section lines. Carefully comparing Figs. 6.15(a) and 6.16(a); and 6.15(b) and 6.16(b), stress magnitudes along 90^0 section line were lesser compared to the stress magnitudes along 270^0 section line for both the cases of 50 and 150 NB pipes.

(a)

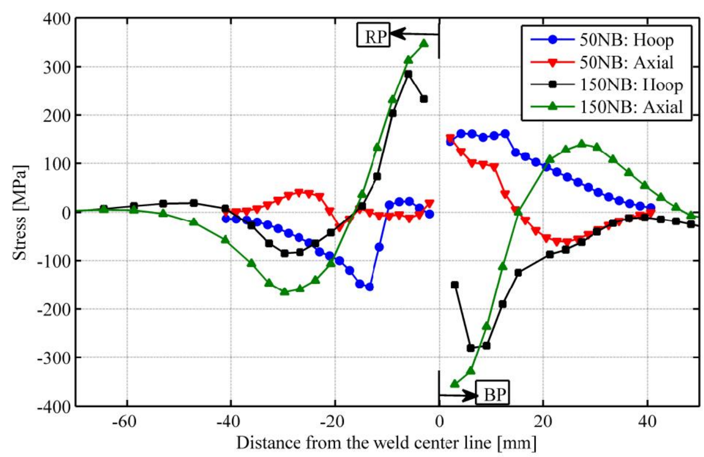

(b)

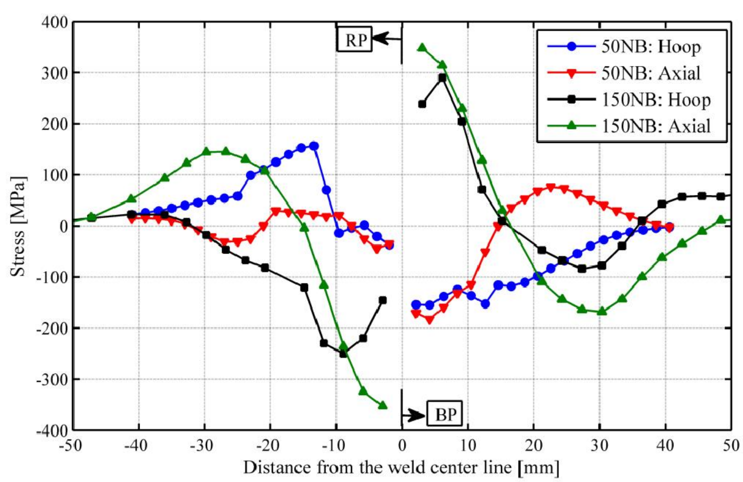

Fig. 6.16 Hoop and axial residual stress for 50 and 150 NB cases along the BP-270^0 section line: (a) On the outer surface and (b) On the inner surface.

Figs. 6.17(a) and (b) depicts the residual stress distributions on the outer and inner surfaces respectively along the BP-180^0 section line for the cases of 50 and 150 NB pipes. From the close observation, it can be seen in Figs. 6.17(a) and (b) that both the hoop and axial stress distributions show similar trend of increasing and decreasing but the stress magnitudes were different between the RP and BP at the corresponding locations away from the WC line.

(a)

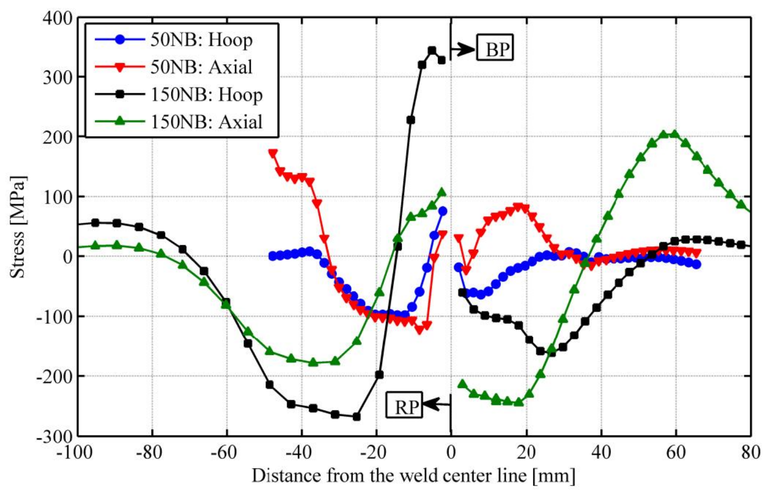

(b)

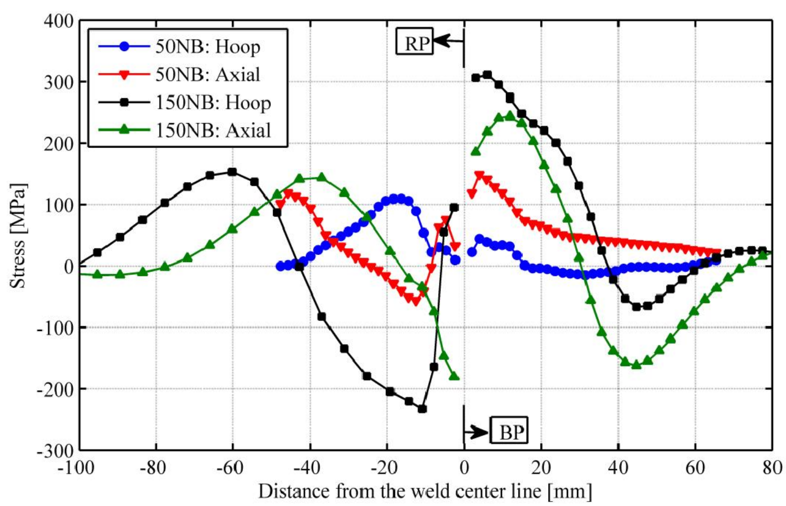

Fig. 6.17 Hoop and axial residual stress for 50 and 150 NB cases along the BP-180^0 section line: (a) On the outer surface and (b) On the inner surface.

For instance, from Fig. 6.17(a), the hoop stresses for the 150 NB case decreases at the WZ and its vicinity. Beyond this the low magnitude compressive stresses again approach to zero value at almost 60 mm away from the WL. Also the similar trend was noticed in the corresponding stress distributions between 50 and 150 NB cases on the both outer and inner surfaces along the 180^0 section line as shown in Fig. 6.17. By comparing Figs. 6.15(a) and (b); 6.16(a) and (b); and 6.17(a) and (b), it was discerned to note that both the hoop and axial stresses were oppositely distributed between the outer and inner surfaces for the both 50 and 150 NB cases. For example, from Figs. 6.15(a) and (b), for the 150 NB case, hoop and axial stresses were tensile at the WL on the RP outer surface and compressive was noticed on the RP inner surface.

Figs. 6.18(a) and (b) compare the hoop and axial stress distributions on the outer and inner surfaces, respectively. In these two figures, stress distributions at two different section lines such as along the BP- 0^0 and 180^0 were compared for the case of 150 NB pipe T-joint. These two figures indicate that although the profiles of both the hoop and axial stress distributions between 0^0 and 180^0 section lines were similar, the stress magnitudes on the both outer and inner surfaces along the 0^0 section line were significantly higher than those along the 180^0 section line with in and near the WL.

The reason for the difference in stress magnitudes between 0^0 and 180^0 section lines can be that the 0^0 section line (i.e. weld S/E location) experiences two thermal cycles during the BP-T-Joint welding. This similar trend was also observed for the C-Seam butt weld joint of cylindrical components in the previous research by [42, 46, 66]. From the same figures, it can also be observed that the reverse trend of hoop and axial stress distribution between the outer and inner surfaces.

(a)

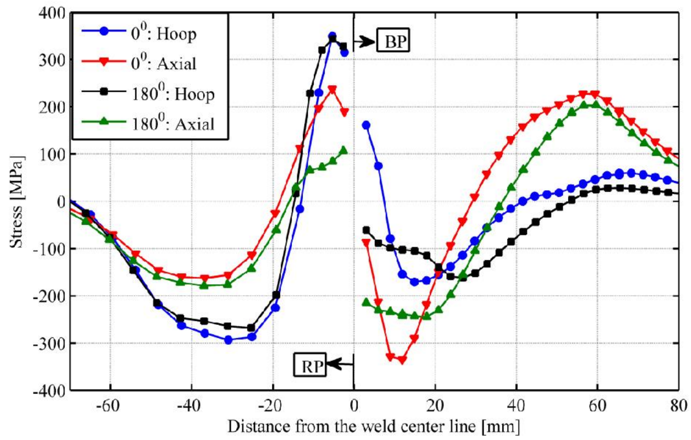

(b)

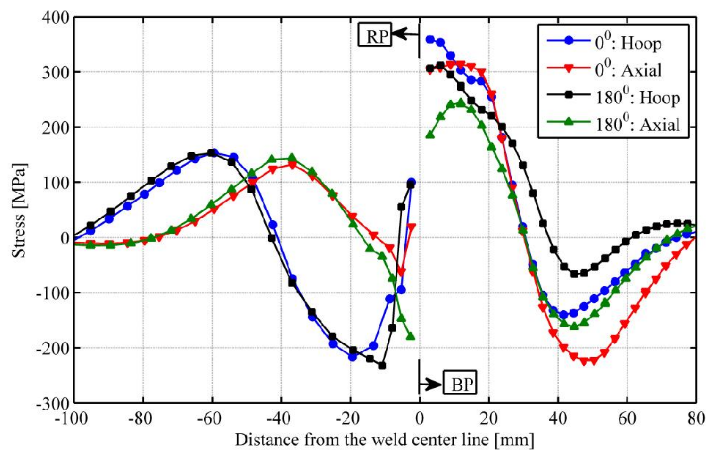

Fig. 6.18 Comparison between hoop and axial residual stresses along BP-0^0 and 180^0 section lines for 150 NB pipe T-joint: (a) On outer and (b) Inner surface.

To clarify the features of welding residual stress distribution for the investigation of pipe diameter effects (i.e. different R_i/T ratios) during BP-T-Joint weld, the middle surface along the BP-0^0 section line was considered in this study. Both the hoop and axial stress distributions for the both 50 and 150 NB cases on the middle surface were shown in Fig. 6.19. In this study, two different pipe diameters with constant wall thickness and having two different R_i/T ratios were considered as shown in Table 6.1. As shown in the Fig. 6.19, the residual stresses at the WL were tensile on the both run and branch pipes. It was very significant to note that after a careful consideration of the results as shown in Figs. 6.15-6.17 and 6.19, both the hoop and axial stress magnitudes for the 50 NB case (i.e. thick cylinder) were lesser than 150 NB case (i.e. thin cylinder). Based on the above observation, it can be concluded that increasing the R_i/T ratio leads to an increase in the both hoop and axial stress. Generally, the hoop residual stresses were induced by the radial expansion and subsequent contraction during welding. Also, the axial residual stresses were mainly determined by the axial expansion and subsequent contraction. For the thick cylinder, the expansion and contraction in the both radial and axial directions were smaller compared to the thin cylinder. In this investigation also, with the lower R_i/T ratio (i.e. thick cylinder) stress magnitudes were less compared to those with the higher R_i/T ratio (i.e. thin cylinder). The observations and trends for the influence of R_i/T ratio on the residual stress distribution were coincide with the results for the C-Seam butt weld joint of cylindrical components recorded by the previous researchers [36]. Fig. 6.19 shows that similar trends of hoop and axial stress distribution and reversal were observed between the RP and BP. Also the similar trend was noticed in the corresponding stress distributions between 50 and 150 NB cases.

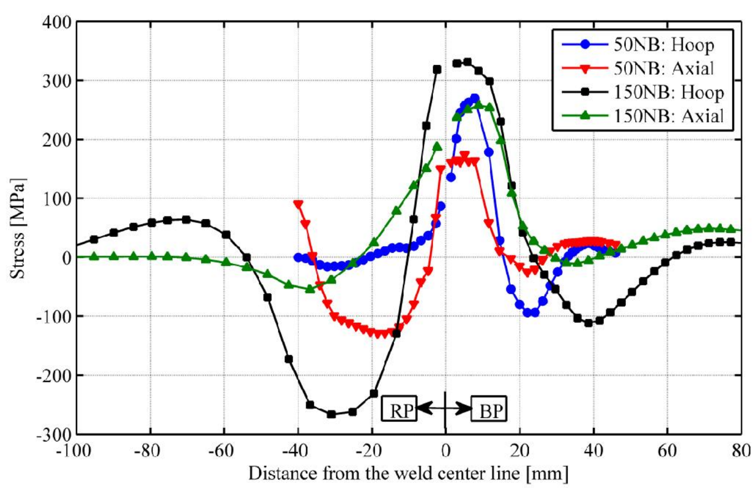

Fig. 6.19 Hoop and axial residual stress distributions for 50 and 150 NB cases along the BP-0^0 section line on the middle surface.

Figs. 6.20(a)-(c) show the hoop, axial and radial stress distributions respectively, on the outer, inner and middle surfaces for the 150 NB pipe case along RP-180^0 section line. The RP-180^0 section line was shown in Fig. 6.2. In the Fig. 6.20, negative and positive coordinates represent the distances from the WC to the left and right side of the BP-180^0 section line. A detailed study was carried out on the above results shown in Figs. 6.20(a)-(c), to understand the residual stress distributions on the outer, inner and middle surfaces along the RP during N-A welded joint. The predicted hoop residual stress in the vicinity of weld area was tensile and compressive on the outer and inner surfaces respectively as shown in Fig. 6.20(a). Similarly, the axial stress at the WL was tensile and compressive on the outer and inner surfaces respectively as shown in Fig. 6.20(b). Figs. 6.20(a) and (b) also illustrate that the hoop and axial stress distributions respectively on the middle surface. Moreover, it can also be found that the hoop and axial stress profiles on the middle surface were similar, but the magnitudes were different. A literature survey [36-38, 42, 46, 110] reveals that a significant research work has been carried out for the cases of C-Seam butt weld joints of different steel cylindrical components. It can be observed from the above literature that the axial stresses on the inner and outer surfaces were tensile and compressive respectively, at the WL. Whereas, the hoop stress on the inner surface was tensile and on the outer surface it was zig-zag in pattern within the HAZ. Based on the above observations between C-Seam butt welding and N-A pipe T-joint, it can be described that the hoop and axial stress distributions on the outer and inner surfaces during BP joint portray opposite trend with those generated during C-Seam butt welding. The results of the radial stress distributions on the outer, inner and middle surfaces along the RP-180^0 section line were shown in Fig. 6.20(c). An interesting observation to note was that unlike the hoop and axial stresses, the radial stresses were not induced during the welding of BP-T-Joint. It can also be seen that the stresses were negligible on both sides of the WL as shown in Fig. 6.20(c). Further, the trends for radial stresses also concur well with the observations recorded by the previous researcher [110].

(a)

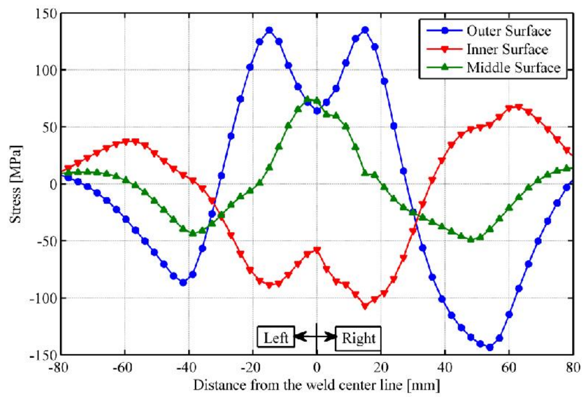

(b)

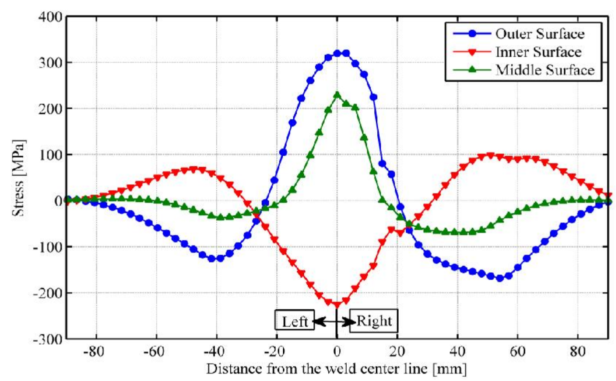

(c)

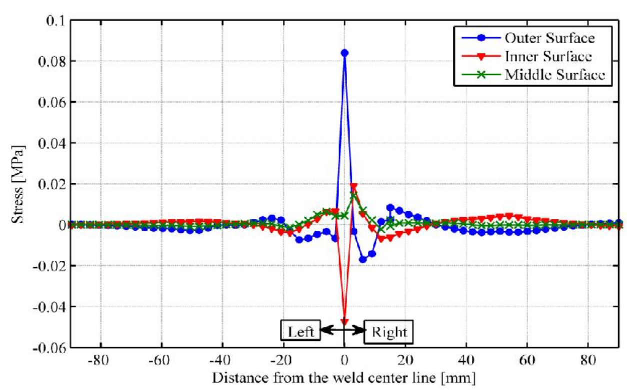

Fig. 6.20 Comparison of stress distributions on the outer, inner and middle surface along RP-180^0 section line for 150 NB case: (a) Hoop stress, (b) Axial stress and (c) Radial stress.

CHAPTER - 07

EFFECT OF WELD INDUCED RESIDUAL STRESSES AND THE INFLUENCE OF WELD SEQUENCING ON CE ROTATING BOWL

This study presents a computational procedure for the evaluation of weld induced residual stresses and distortions for a typical GTAW welded three-plane C-Seam butt joint of CE rotating bowl. In this study, the total work executed was divided in to two parts. First part highlights the importance of weld sequencing by using the FE code weld planner in order to control distortions. Second part discusses the distribution of residual stresses in CE rotating bowl by carrying out sequentially coupled thermo-matallurgical-mechanical analysis using SYSWELD. The GTAW process was simulated using a moving double ellipsoidal heat source model. The axial and hoop residual stresses on the inner and outer surfaces were computed. Tensile residual stress on the inner surface and compressive residual stress on the outer surface are observed and their impacts on the CE rotating bowl are discussed. Also, the present work was undertaken to study distribution of residual stresses during and after the welding process of CE rotating bowl using FE simulation. Further, the welding distortion has negative effects on the accuracy of assembly, geometrical tolerances and unbalance mass [16]. The importance of weld sequencing and its inference was investigated.

7.1. Approach to this study:

During the first part of this study, different cases of weld sequences are considered to study the variation in welding distortions based on numerical simulations. Three cylindrical components with an external diameter of 42 mm, wall thickness of 2 mm and total length of 130 mm are considered for the simulation. A full 3D model was used in the weld planner and their meshes with BC are shown in Figs. 7.1(a) and (b) respectively. The analysis was performed using the FE code weld planner in SYSWELD. The effects of tack welds on distortions are neglected in the analysis.

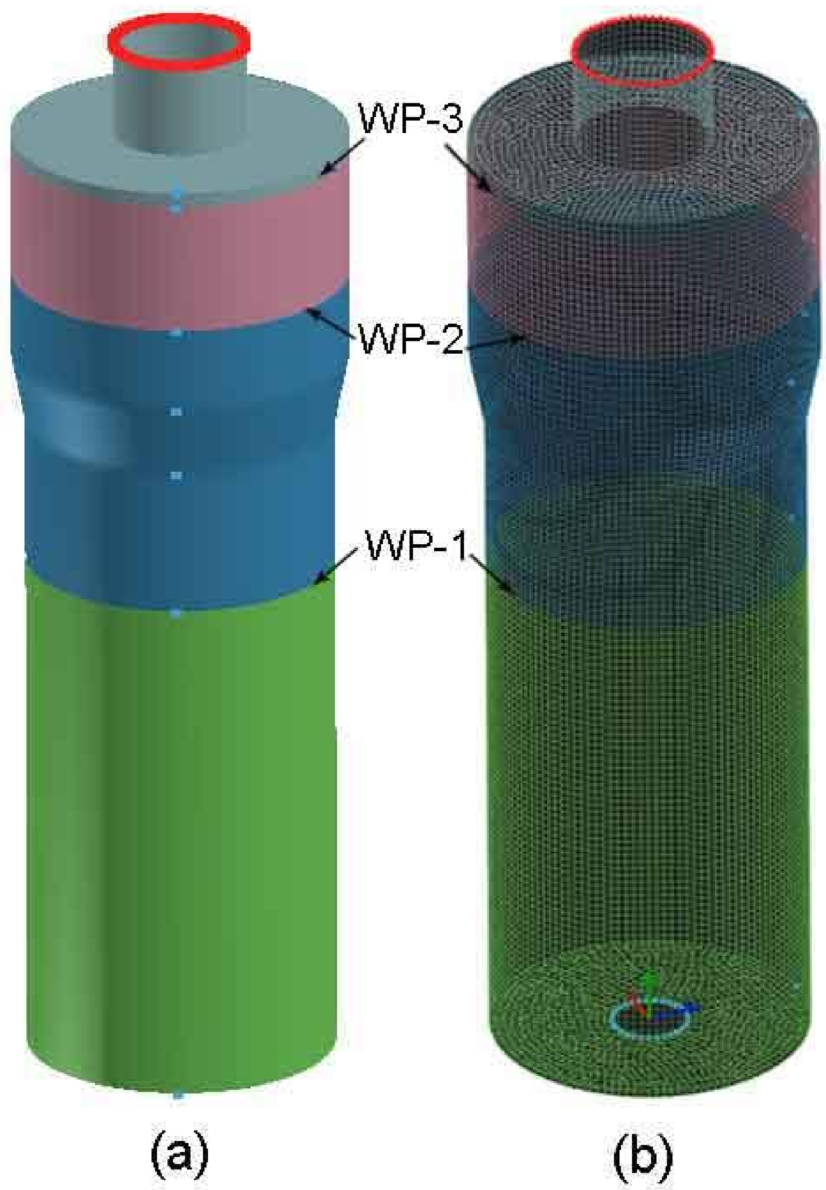

Fig. 7.1 (a) 3D model and (b) FE mesh.

During the second part of the study, 3D heat conduction analysis was performed in order to obtain the temperature distribution history at all the nodes of the weld model.

Further, the same thermal loads are employed in the subsequent mechanical analysis for the evaluation of weld distortions and residual stresses. The chemical composition, temperature dependent thermo-mechanical and thermo-physical properties of ASS (i.e. AISI 304L) that are used for numerical simulation are discussed in the Section 3.5.2. FE analysis was performed applying same material properties for both the base and weld metal. The ambient temperature was assumed to be 25^0C. The 3D model and FE mesh which was used for residual stress analysis was shown in Fig. 7.2. The element type used was Quard-3D solid with three translational degree of freedom at each node.

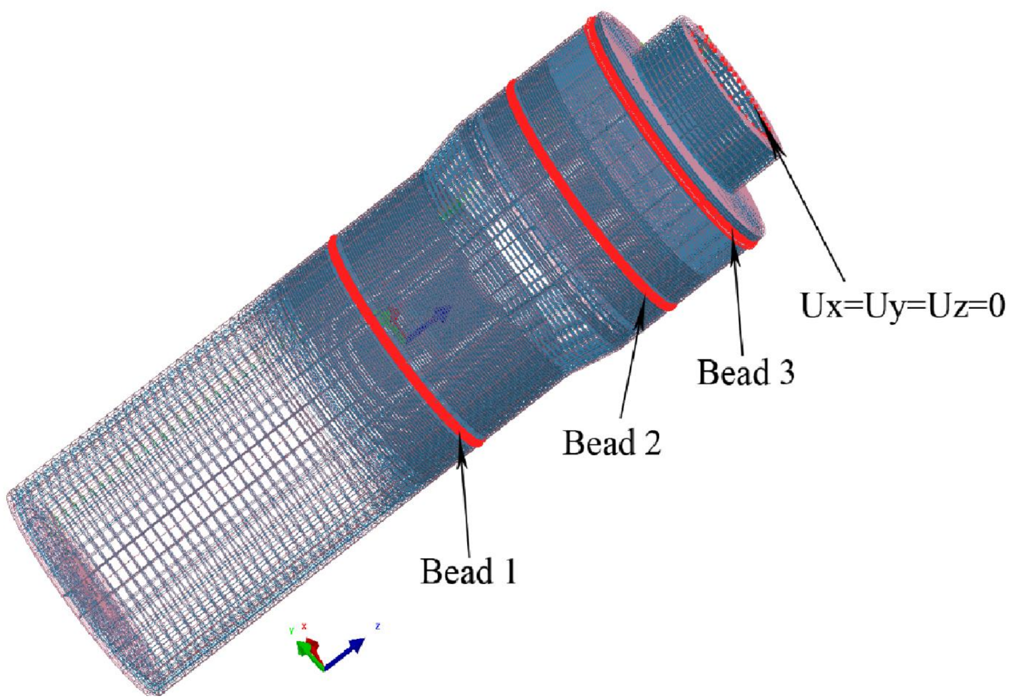

Fig. 7.2 FE mesh with boundary conditions.

7.2. Simulation results and discussions:

This section deals with the results of effect of weld sequencing and the distributions of residual stresses in a three plane circumferentially butt welded CE rotating bowl.

7.2.1. Influence of weld sequencing:

Well planned weld sequencing involves weld starting at different points so that, as the component shrinks at one place, it counter acts the weld shrinkage forces where welds were already made. Five different weld sequences have been considered in this study and these are obtained based on the experience during fabrication of CE rotating bowl. These sequences are single and four steps of forward welding at each plane. As shown in Fig. 7.3, the continuous weld at each plane was represented in case 1 and the four step different sequence welds are shown in cases 2-5. In the case 1, weld was conducted entirely in each plane as one segment from the weld start location to the end location. For the remaining four cases, each weld plane was divided into 4 segments and the total of 12 segments was considered for this investigation as shown in Fig. 7.3. Fig. 7.4 shows the diameter variation/ distortion distribution and also compares the total distortion for five different cases of weld sequencing analyzed by the numerical simulation. The diameter variation gives a value of the ovality of the component due to welding. This indicates that, the diameter of the component in the weld metal region and its vicinity reduces after welding. This bending deformation in the component generates stresses through the component thickness. The observations and the trends seen on the weld induced distortions in this study are found to be in agreement with the results reported in the literature [43]. Results of case-1 reveal that continuous welding in each plane gives higher radial distortion than the weld sequencing by four segments for each plane. It can be seen that there was considerable variation in distortions within the HAZ for the different cases as shown in Fig. 7.4. For the cases 2 to 5, total of twelve segments are considered and with different weld sequencing weld distortion ranges from 186 microns to 162 microns are observed. Fig. 7.4 reveals that welding according to cases 2 to 5 are good consequence to minimize welding distortion. This finding tells that increasing number of sequences in the C-Seam welding process always leads to decrease in weld distortions.

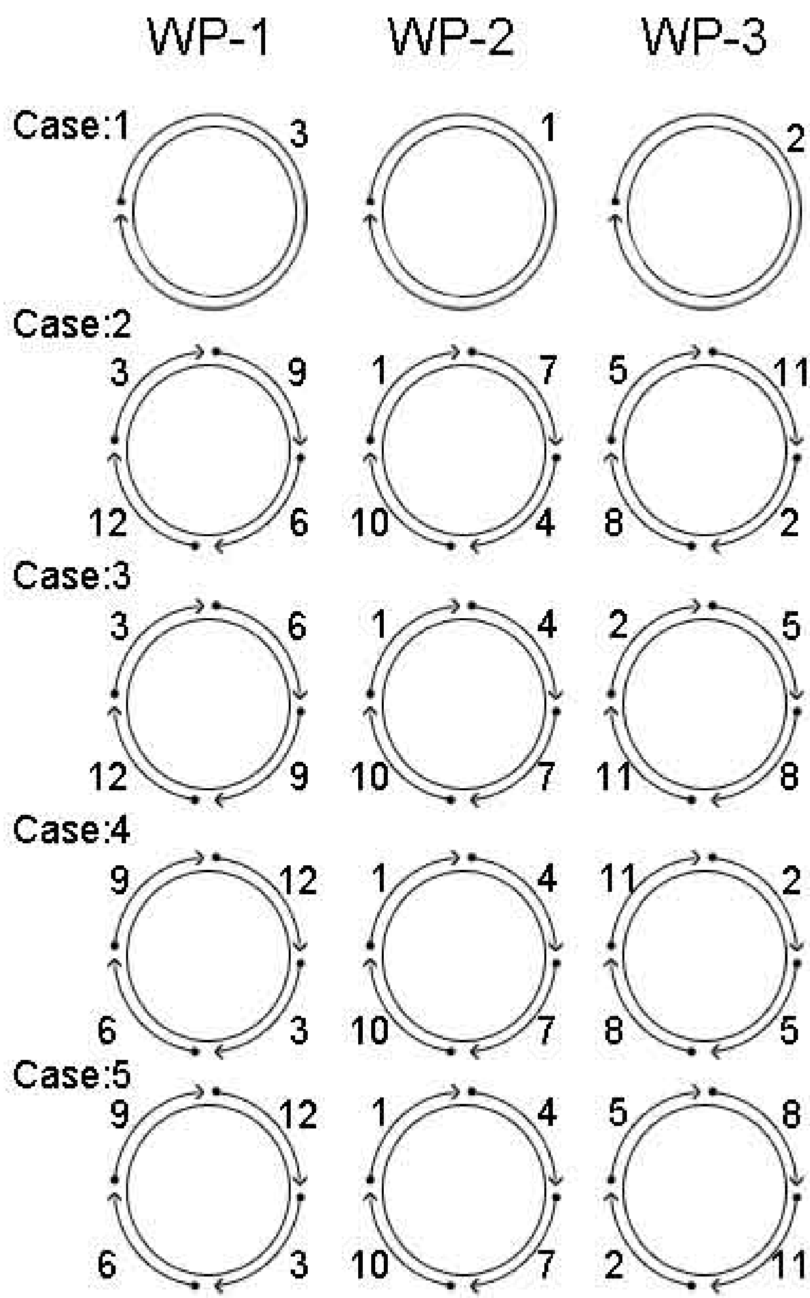

Fig.7.3 Five different cases of weld sequencing.

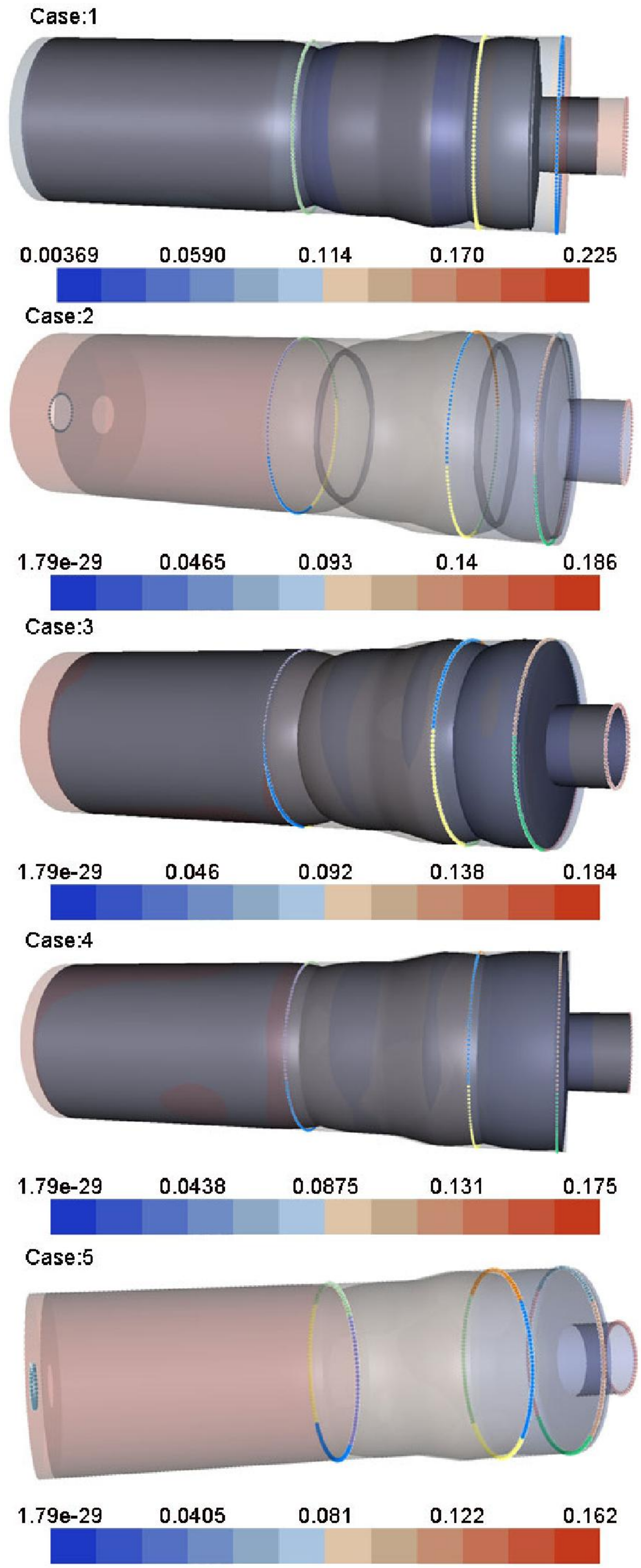

Fig. 7.4 Distortion contour plots of CE rotating bowl.

7.2.2. Welding residual stress distribution on CE rotating bowl:

During the analysis, three C-Seam butt weld joints are considered to develop a CE rotating bowl and it was necessary to provide the weld joint totally from outside. These three butt weld joints are represented as bead 1, bead 2 and bead 3. It was proposed to divide each bead in to three segments, spacing 120° each. The FE model was run for one pattern of weld sequencing. The beads, segments and weld sequencing are shown in Fig. 7.5. To ascertain the influence of weld sequencing on the distribution of residual stresses thermo-matallurgical-mechanical analysis was performed and the weld speed was considered as 0.5 mm/s. Simulation was run for a time period of 10,000 s.

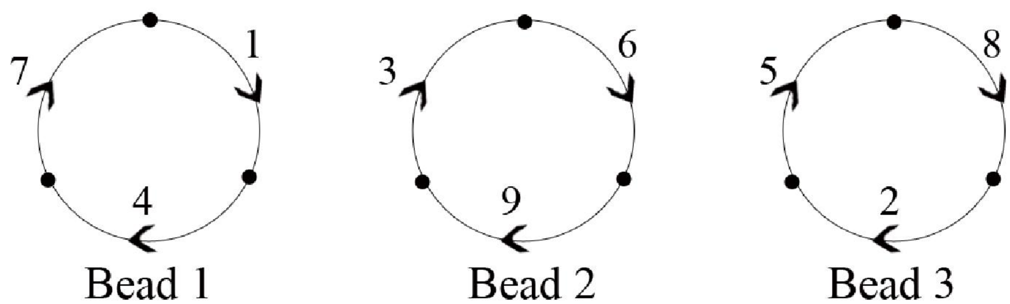

Fig. 7.5 Sequence of welding for all three beads.

In case of butt weld joints of cylindrical components, stress normal to the direction of the weld bead was the axial residual stress, stress parallel to the direction of weld bead was the hoop residual stress and stress that acts towards or away from the central axis of a curved member was called the radial stress. The hoop residual stresses are generated due to expansion and contraction in radial direction during thermal cycling in the welding process. Variable shrinkage patterns through the wall thickness occur due to different temperature gradients generates radial residual stresses on both sides of WL. The contour plot of Von Mises stress distribution at 500 s was shown in Fig. 7.6 and its maximum value was 298.3 MPa.

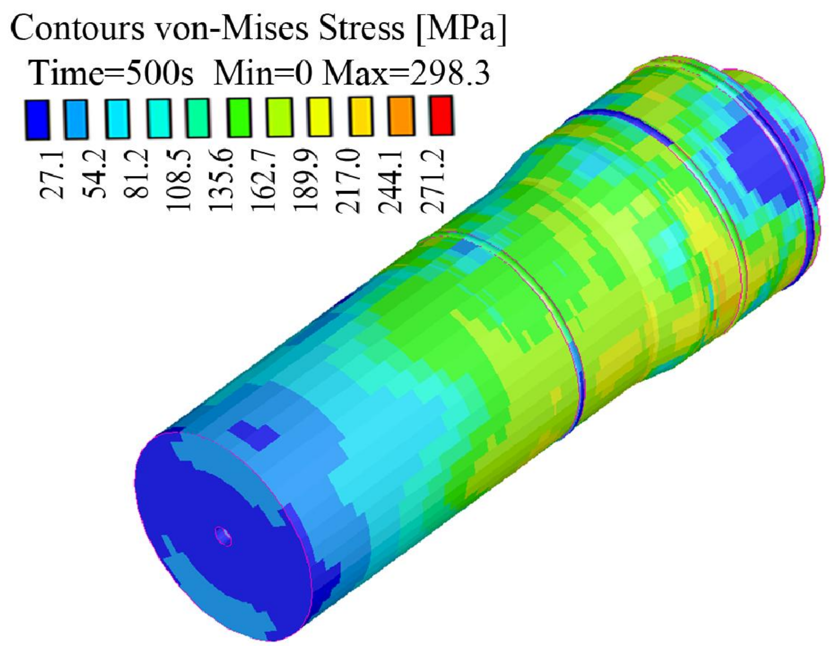

Fig. 7.6 Contours of von Mises stress.

The weld process takes about 1100 s to complete all the three plane circumferential butt welds. In the mechanical analysis axial, hoop and radial residual stresses are simulated on inner and outer surfaces for cases immediately after completion of weld (i.e., at 1100 s) and after cooling the work piece to 10000 s. Figs. 7.7 and 7.8 show the axial, hoop and radial residual stress distributions on the inner surface after completion of weld (i.e., at 1100 s) and after cooling the work piece to 10000 s respectively. Figs. 7.9 and 7.10 depict stress distributions on the outer surface at 1100 s and at 10000 s respectively. Stress distributions on the inner and outer surfaces were taken at 180^{o} cross-section from the weld start position.

From these figures, it can be seen that the stresses are both tensile and compressive due to temperature gradients, uneven shrinkage and the type of BC. On the inner surface, at bead 1, compressive axial stress field was noticed near the high temperature region. Whereas, a tensile stress was formed in the low temperature region. The reason for this could be, as the time progresses the temperature in the WZ decreases; whereas in the surrounding region, temperatures start to increase due to law of conduction from weld bead. This causes the weld metal close to bead to contract, and away from bead to expand. Figs. 7.7 and 7.8 illustrate that at bead 1, compressive hoop stresses are predicted at the HAZ at t = 1100 s, while tensile hoop stresses (comparatively) emerge in the newly solidified metal at t = 10000 s for hoop stress. In general, the trend for the axial and hoop stresses at the WZ on the inner surface was tensile which are in line with the results published in [16,37]. In this study, tensile hoop and axial stresses are observed at bead 2 and these are in the range of 100 to 150 MPa. Bead 3 was very close to the top plate and nearer to the boundary condition as shown in Fig. 7.2. Hence, at bead 3 compressive axial and hoop stresses are generated which are negligible and localized.

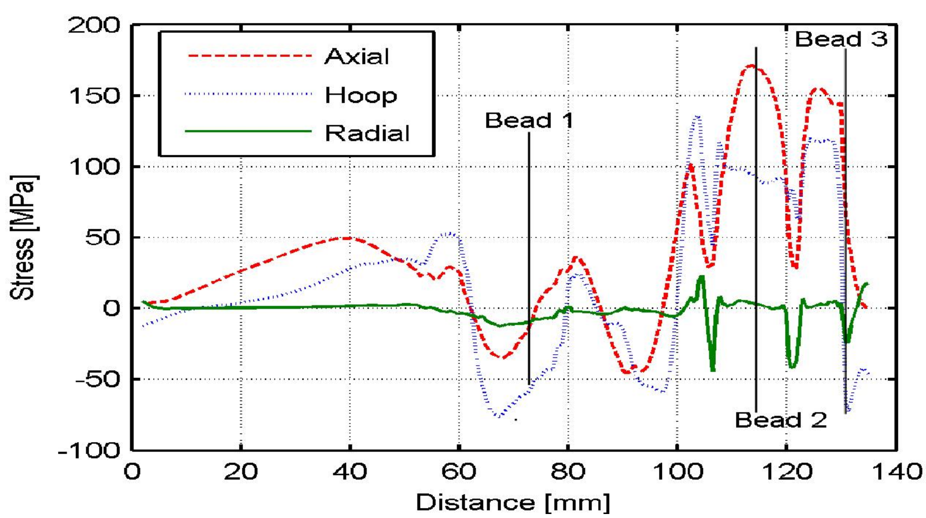

Fig. 7.7 Stress distribution at t=1100 s on the inner surface.

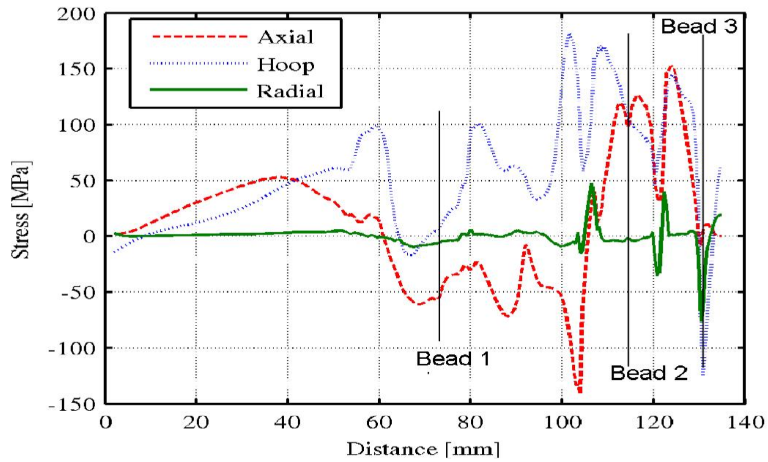

Fig. 7.8 Stress distribution at t=10,000 s on the inner surface.

On the other hand, the results of axial and hoop stresses on the outer surface show an opposite trend at bead 2. Figs. 7.7-7.10, also exhibit the radial stress distribution on the inner and outer surfaces at times t = 1100 s and t = 10000 s. An interesting observation to note is that unlike the hoop and axial stresses, the radial stresses are not influenced by time. It can also be seen that the radial stresses are negligible on both sides of the WL on the inner and outer surface. At bead 2, the transition of axial and hoop stresses from compressive to tensile was obtained near the HAZ at t = 1100 s, where as the transition from compressive to tensile was observed away from the HAZ at t = 10000 s as shown in Figs. 7.9 and 7.10.

The trends for axial and hoop stresses at bead 2 also concur well with the observations recorded by the previous researchers [16, 37, 38]. The magnitude of hoop and axial stresses at bead 1 on the inner and outer surfaces are very less and that may be attributed to reasons such as no constraints at the bottom side of the CE rotating bowl and weld sequencing for all three C-Seam butt joints.

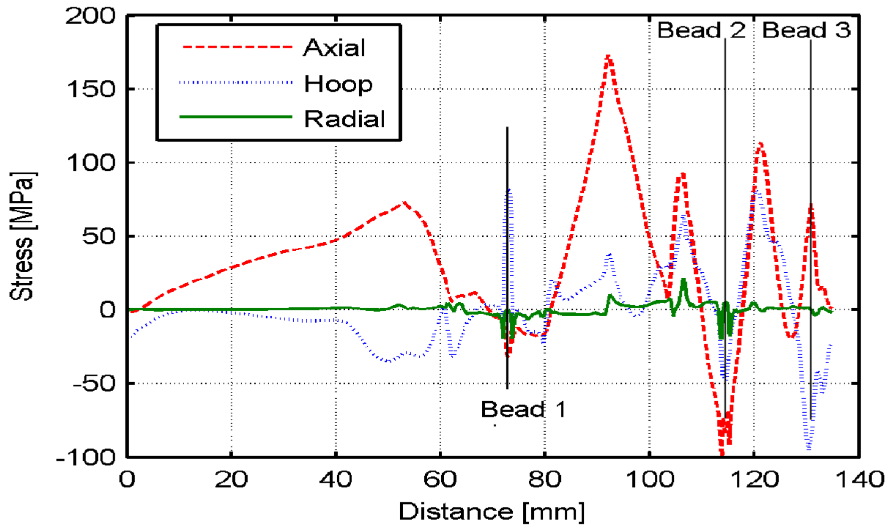

Fig. 7.9. Stress distribution at t=1100 s on the outer surface.

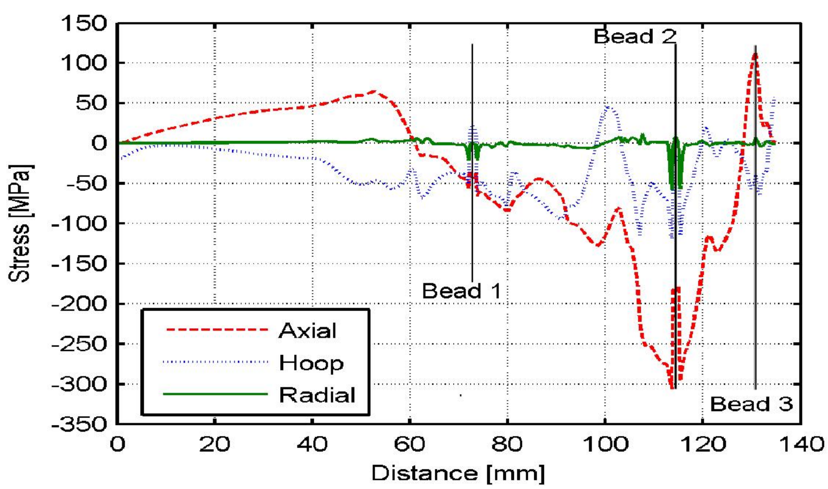

Fig. 7.10. Stress distribution at t=10,000 s on the outer surface.

7.3. Experimental validation:

To ensure the reliability and for comparison with numerical simulation results, GTAW experiments are conducted and was shown in Fig. 7.11. The experiments are performed for one pattern of weld sequencing as shown in Fig. 7.5. The three cylinders and an end plate are initially joined by four tack welds (each 90^0 apart) at each bead. Experimental residual stress measurement was performed using XRD method and it was described in the Section 5.1.3.

Fig. 7.11 Experimental setup for the CE rotating bowl

Axial residual stresses are measured at the weld centers of bead 1 and 2 at the 180° plane and 300° plane respectively. Similarly, hoop stresses are also measured at the same locations. The quantitative comparison of measured values and simulated nodal residual stresses at the WC was shown in Fig. 7.12. It was evident that simulated results are in a good agreement with the experimental data, thus the numerical simulations are experimentally validated.

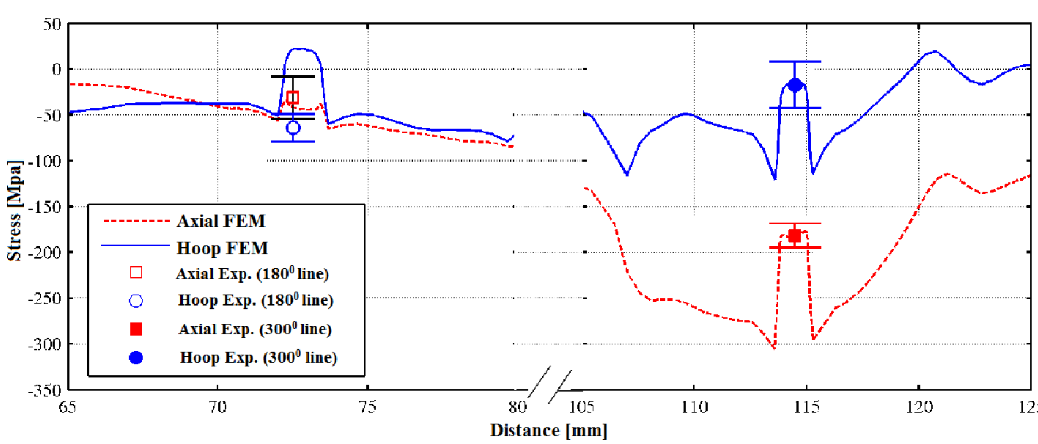

Fig. 7.12 Experimental validation of residual stresses.

CHAPTER - 08

CONCLUSIONS AND FUTURE SCOPE

CONCLUSIONS:

3D sequentially coupled thermo-metallurgical-mechanical analysis has been performed to investigate the effect of different heat source parameters on the influence of shape and boundaries of FZ and HAZ, transient temperature distributions and volumetric heat flux distribution. Also, to produce the weld characteristics: (i) between L-Seam and C-Seam butt weld joints of cylindrical components; (ii) for the 50 and 150 NB N-A butt welded BP-T-Joints; and (iii) the weld induced imperfections in the AISI 304 L stainless steel CE rotating bowl with different weld sequences in a three plane axisymmetrical circumferentially butt welded joint. The following are the major conclusions from the present study.

1) Characterization of heat source parameters:

(i) Maximum temperature is different for all the sixteen different cases of geometric parameters. Also, high value of geometric parameters a_f, a_r, b and c diminish the volumetric heat flux densities (q_f and q_r) and the temperatures; that ultimately causes reduction in weld pool dimensions and vice-versa is observed.

(ii) Peak temperatures at the weld centre line decrease on the both inner and outer surfaces as the moving heat source geometric parameters increase for the constant heat input. Moreover, considerable effect on temperature distributions within the HAZ is noticed due to the fact that the localized heating at the FZ.

(iii) The results of the FE simulation revealed that there is no influence on the residual stress distributions with the variation in moving heat source parameters.

The most important contribution of this investigation is to conclude that the variation in moving heat source geometric parameters is negligible on the mechanical characteristics. Hence, the assessment of heat source geometric parameters prior to numerical simulation studies may be ignored in order to reduce cost and time by avoiding weld experiments.

2) Weld characteristics between L-Seam and C-Seam butt weld joints:

(i) During HSF analysis, the energy input for L-8, C-8, L-6 and C-6 cases were obtained based on the proper shape and boundaries of FZ and HAZ. The experimental macrograph and the predicted FE simulation weld molten pool sizes are in reasonable agreement with each other.

(ii) The peak temperatures at the WC and at locations away from the WC for L-Seam welds are 60^0C higher than the C-Seam welds. This minor difference in peak temperature may not be a reason for stress variation between L-Seam and C-Seam welds.

(iii) The FE analysis of hoop and axial stresses revealed a considerable variation between L-Seam and C-Seam welds. The increase in hoop tensile stress at the WC for L-Seam welds was found to be 225 MPa and 180 MPa on the inner and outer surfaces respectively.

(iv) In case of C-Seam weld joint at the WL, on the inner surface the magnitude of increase in axial tensile stresses was about 60 MPa; whereas, it was about 80 MPa for compressive stresses on the outer surface. The above numerical results indicate that the L-Seam weld joints are not advisable to use while fabricating cylindrical components in order to improve the service life.

3) N-A butt welded BP-T-joints:

(i) Weld characteristics are obtained for the 50 and 150 NB butt welded branch pipe T-joints by performing numerical simulations with experimental validation. Significant differences in temperature distributions are observed between run and branch pipes; 50 and 150 NB pipe cases; and along 90^o, 180^o and 270^o sections.

(ii) Residual stress states between run and branch pipes; outer and inner surfaces; and for different pipe sizes at different sections are also explored and compared. Based on the results, the important observations are: (a) along the both BP-90^o and 270^o section lines, stress distributions portray reverse trend in between RP and BP; and 50 and 150 NB cases; (b) stress magnitudes along BP-90^o section line are less than that of 270^o section; (c) along all the BP sections lines, stresses are oppositely distributed between the outer and inner surfaces; (d) stress magnitudes along the BP-0^o section line are significantly higher than those along the BP-180^o section; (e) stress magnitudes for the 50 NB case (i.e. thick cylinder) are less than 150 NB case (i.e. thin cylinder) with the same wall thickness; (f) along the RP-180^o section, stresses on the outer and inner surfaces are tensile and compressive respectively; and (g) radial stresses are found to be negligible.

(iii) An emphasis is focused on comparing the BP-T-joint results with the open literature of circumferential butt weld joint results for the same geometrical, material and weld process parameters. The major contribution of this investigation is to conclude that the stress magnitudes are almost similar and the distributions. Hence, the joining of branch pipes to main pipes by using a single N-A butt weld joint is the most successful method with respect to cost, service life, weld length, FZ/HAZ volume etc.

4) Three plane axisymmetrical C-Seam welded joint of CE rotating bowl:

This study performs a FEA of the residual stress and weld distortions in the AISI 304 L stainless steel CE rotating bowl with different weld sequences in a three plane circumferentially butt welded joint. The following conclusions are drawn:

(i) Radial weld distortions from 3D numerical analysis are predicted and compared.

(ii) The weld distortion in the HAZ area with one segment in each plane could be decreased by using a sequence of four segments in each plane, indicating the benefits of welding sequence to decrease the welding distortions.

(iii) The maximum tensile axial and hoop stresses are generated at the weld bead 2 on the inner surface. Whereas, the peak compressive axial stress is noticed at bead 2 on the outer surface.

(iv) The results of the FE simulation revealed that the radial residual stresses are found to be negligible. Magnitudes of axial and hoop residual stresses are found to be lesser in this study when compared to single plane continuous C-Seam butt weld joint. The residual stress induced is below the yield strength of the material in this study. This reduces the susceptibility of the weld to fatigue damage, SCC and fracture.

(v) The numerical results for residual stress distributions obtained were in good agreement with those obtained by the X-ray experiments.

FUTURE SCOPE:

The apprehension in the metal joining is the analysis of different type of axisymmetrical and N-A butt weld joints of cylindrical components for the study of weld induced imperfections. This research work has considerably contributed towards this requirement for welding of thick and thin walled cylindrical components using both numerical simulations and experimental validation. The prediction of weld induced imperfections for all the critical components is essential before the start of actual welding process. Further, the future scope is discussed in the following.

(i) The present analysis of characterization of heat source parameters needs to be enhanced to study their influence on the and distortion patterns.

(ii) Weld characteristics can also be obtained between L-Seam and C-Seam weld joints of cylindrical components for dissimilar materials, thick cylinders, multi pass welds, large diameter pipes and for different welding processes.

(iii) This methodology for different axisymmetrical and N-A butt weld joints of cylindrical components based on FEA can also be applied for the analysis of other steel materials like P91 etc., by incorporating the temperature dependent thermal and material properties with necessary experimental validation.

(iv) It is further proposed to study the peak cyclic stress and the non-linear through-thickness stress distributions of various weld parameters on the assessment of the fatigue crack initiation life of the component due to welding induced imperfections by using strain-life methodology.

(v) Metallurgical aspects pertain to phase transformations, grain size and hardness in concurrence with different axisymmetrical and N-A butt joints can be studied.

References

[1] O.W. Blodgett. Distortion: How to minimize it with Sound Design Practices and Controlled Welding Procedures plus Proven Methods for Straightening Distorted Members, pp. 1-19, Bulletin G261, The Lincoln Electric Company, Cleveland, OH.

[2] Z. Feng. Processes and Mechanisms of Welding Residual Stress and Distortion. Woodhead Publishing, 2005.

[3] Murugan S, Rai SK, Kumar PV, Jayakumar T, Baldev Raj Bose MSC. Temperature distribution and residual stresses due to multipass welding in type 304 stainless steel and low carbon steel weld pads. Inter J Press Ves Piping 2001; 78: 307–17.

[4] K. Masubuchi. Analysis of Welded Structures, Pergamon Press, London 1980. ISBN 0-08-022714-7.

[5] D. Radaj. Heat Effects of Welding, ISBN 0-387-54820-3, Springer-Verlag, 1992.

[6] Y. Ueda, K. Fukuda and Y.C. Kim. New Measuring Method of Axis-symmetric Three-Dimensional Residual Stresses Using Inherent Strains as Parameters. Journal of Engineering Materials and Technology 1986; 108: 328-334.

[7] R. W. Messler (Jr.), “Principles of Welding (Processes Physics, chemistry and metallurgy), Wiley International, NY, 1999.

[8] S.R. Ikeagu. Evaluating the Effects of Different Welding Processes on the Distortion of 4mm Thick DH36 Ship Panels. M. Sc. Thesis, School of Applied Sciences, Cranfield University, 2007.

[9] B. Ahmed. Distortion Response of Synchronized Tandem Wire Gas Metal Arc Welding. M. Sc. Thesis, School of Industrial and Manufacturing Science, Cranfield University, 2006.

[10] Y. Takeda. Prediction of Butt Welding Deformation of Curved Shell Plates by Inherent Strain Method. Journal of Ship Production 2002; 18(2): 99-104.

[11] L. Hong and H. Ren. Simulation of Welding Deformations of Ship Structures. Key Engineering Materials 2006; 324-325: 651-654.

[12] P. Segle, S.-T. Tu, J. Storesund, L. A. Samuelson. Some issues in life assessment of longitudinal seam welds based on creep tests with cross-weld specimens. Inter J Press Ves Piping 1996;66:199–222.

[13] Maddox, S.J., "Influence of Tensile Residual Stresses on the Fatigue Behavior of Welded Joints in Steel", American Society for Testing and Materials, 1982, 776: 63-96.

[14] P. Dong, F.W. Brust,., Welding residual stresses and effects on fracture in pressure vessel and piping components: A Millennium Review and Beyond [J]. Trans. ASME Journal of Pressure Vessel Technology, 2000, 122: 329-338.

[15] Toribio J., Residual stress effects in stress-corrosion cracking, Journal of Materials Engineering and Performance, 1998, 7 (2):173-182.

[16] A. Ravisankar, Satish K. Velaga, Gaurav Rajput, S. Murugan and S. Venugopal, "Numerical simulation of welding distortion: A comparative study of variable weld speeds and powers with constant heat input", Int. conference on advances in manufacturing technology – ICAMT, June 15-17, 2012.

[17] Rosenthal, D., The Theory of Moving Heat Source and its Application to Metal Treatment, Transaction ASME, 1946.

[18] Eager, T. W., and Tsai, N. S. 1983. Temperature fields produced by travelling distributed heat sources. Welding Journal 62(12): 346-s to 355-s.

[19] Jeong, S. K., and Cho, H. S. 1997. An analytical solution to predict the transient temperature distribution in fillet arc welds. Welding Journal 76(6): 223-s to 232-s.

[20] Goldak J, Chakravarti A, Bibby M. A new element model for welding heat source. Metall Trans B 1984;15B:299–305.

[21] Nirasanametla YADAIAH and Swarup BAG, Effect of heat source parameters in thermal and mechanical analysis of linear GTA welding process, ISIJ International, 52. (2012): 2069–75.

[22] Victor D. Fachinotti and Alberto Cardona, Semi- analytical solution of the thermal field induced by a moving double-ellipsoidal welding heat source in a semi-finite body, The mechanical computational, Association Argentina, 10-13 November, (2008): 1519- 30.

[23] Guangming Fu, Marcelo Igor Lourenco de Souza and Segen F. Estefen, Transient temperature distribution analysis using Goldak's double ellipsoidal moving heat source, 6 congresso brasileiro de P&D EM, Subsea Technology Laboratory, COPPE/UFRJ-Ocean Engineering Department, P.O.Box 68508, 21945/970 Rio de Janeiro, Brazil.

[24] Amin S. Azar, Sigmund K. As and Odd M. Akselsen, Determination of welding heat source parameters from actual bead shape, Comp Mater Sci, 54. (2012): 176–82.

[25] D. Gery, H. Long and P. Maropoulos, Effects of welding speed, energy input and heat source distribution on temperature variations in butt joint welding, J Mater Process Tec, 167. (2005): 393–401.

[26] N. T. Nguyen, A. Ohta, K. Matsuoka, N. Suzuki and Y. Maeda, Analytical solutions for transient temperature of semi-infinite body subjected to 3D moving heat sources, Welding Research, supplement to the welding journal, August, (1999): 265s – 274s.

[27] Suraj Joshi, Jorg Hildebrand, Abdulkareem S. Aloraier and Timon Rabczuk, Characterization of material properties and heat source parameters in welding simulation of two overlapping beads on a substrate plate, Comp Mater Sci, 69. (2013): 559–65.

[28] Guang Ming Fu, Ji jun gu, John alex, Marcelo igor and Segen F. Estefen, An analytical and numerical study of parametric research of Goldak's heat source model in MIG welding process and experimental calibrations, 24 congresso nacional de transporte aquaviario, Rio de janeiro, 15-19 October, (2012).

[29] Maria Behulova and Daniel svrcek, Analysis of the influence of parameters of Goldak model on the computed temperature distribution in a weld, Slovak university of technology in Bratislava, Paulinska 16, 917 24 Trnava, Slovak Republic.

[30] V. N. Maksimovich, E. N. Novosad, G. V. Plyatsko. Determination of optimum heating zones in strengthening of longitudinal welded joints in cylindrical shells. Strength of materials: Springer-Verlag1982;14(4):512-7.

[31] R. A. Silva, G. Z. Batista, L.F. G. de Souza, I.S. Bott. Effect of Varying High Frequency Induction Bending on the Longitudinal SAW Weld of API X80 Steel Pipe. Trans Tech Publications, Switzerland: Materials Science Forum 2012;706-709:2059-65.

[32] J. Guirao, E.Rodríguez, A.Bayón, F.Bouyer, J.Pistono, L.Jones. Determination through the distortions analysis of the best welding sequence in longitudinal welds VATS electron beam welding FE simulation. Fusion Eng Des 2010;85:766–779.

[33] V. M. Prokhorenko, A. O. Perepichay, I. Mamuzić, A. Čikić. Reduction of longitudinal axial residual stresses in near-root region of circumferential joint of steam pipeline in technological way. METALURGIJA 2013;52(4):449-52.

[34] Z. Barsoum. Residual stress analysis and fatigue of multi-pass welded tubular structures. Eng failure anal 2008;15:863-74.

[35] Ji-Hua Zhu, Ben Young. Effects of transverse welds on aluminum alloy columns. Thin-Walled Structures 2007;45:321-9.

[36] Chin-Hyung Lee, Kyong-Ho Chang. Three-dimensional finite element simulation of residual stresses in circumferential welds of steel pipe including pipe diameter effects.Mater Sci Eng A 2008;487(1-2):210-18.

[37] Malik AM, Ejaz M. Qureshi, Naeem Ullah Dar, Iqbal Khan. Analysis of circumferentially arc welded thin-walled cylinders to investigate the residual stress fields. Thin-Walled Structures 2008;46(12):1391-401.

[38] Dean Deng, Hidekazu Murakawa. Numerical simulation of temperature field and residual stress in multi-pass welds in stainless steel pipe and comparison with experimental measurements. Comp Mater Sci 2006;37(3):269-77.

[39] Tso-Liang Teng, Peng-Hsiang Chang, Wen-Cheng Tseng. Effect of welding sequences on residual stresses. Comp Struct 2003;81:273-86.

[40] Kermanpur, M. Shamanian, V. Esfahani Yeganeh. Three-dimensional thermal simulation and experimental investigation of GTAW circumferentially butt-welded Incoloy 800 pipes. J Mater Process Tec 2008;199:295–303.

[41] Brickstad B, Josefsonb BL. A parametric study of residual stresses in multi-passbutt-welded stainless steel pipes. Inter J Press Ves Piping 1998;75:11–25.

[42] Chin-Hyung Lee, Kyong-Ho Chang, Jeong-Ung Park. Three-dimensional finite element analysis of residual stresses in dissimilar steel pipe welds. Nuclear engineering and design 2013;256:160-8.

[43] I. Sattari-Far, Y. Javadi. Influence of welding sequence on welding distortions in pipes. Inter J Press Ves Piping 2008;85:265–74.

[44] Deng Dean, Murakawa Hidekazu. Prediction of welding residual stress in multi-pass butt-welded modified 9Cr–1Mo steel pipe considering phase transformation effects. Comp Mater Sci 2006;37:209-19.

[45] S. Paddea, J.A. Francis, A.M. Paradowska, P.J. Bouchard, I.A. Shibli. Residual stress distributions in a P91 steel-pipe girth weld before and after post weld heat treatment. Mater Sci Eng A 2012;534:663-72.

[46] Dean Deng, Shoichi Kiyoshima. FEM prediction of welding residual stresses in a SUS304 girth-welded pipe with emphasis on stress distribution near weld start/end location. Comp Mater Sci 2010;50:612-21.

[47] Wen-chun Jiang, Xue-wei Guan. A study of the residual stress and deformation in the welding between half-pipe jacket and shell. Mater Des 2013;43:213-9.

[48] Panagiotis Michaleris. Residual Stress Distributions for Multi-Pass Welds in Pressure Vessel and Piping Components. PVP-ASME 1996;327.

[49] J. J. Blass, R. L. Battiste, D.G. O’Connor. Reduction factors for creep strength and fatigue life of modified 9 Cr-1 Mo steel weldments, ASME pressure vessels and piping conference (910602). San Diego, CA (USA), 23-27 Jun 1991; 22:17.

[50] Satish K. Velaga, Gaurav Rajput, S. Murugan, A. Ravisankar, S. Venugopal. Comparison of weld characteristics between longitudinal seam and circumferential butt weld joints of cylindrical components. J Manuf Process 2015;18:1-11.

[51] Hong-Yeol Bae, Yun-Jae Kim, Ju-Hee Kim, Sung-Ho Lee, Kyung-Soo Lee, Chi-Yong Park. Three-dimensional finite element welding residual stress analysis of penetration nozzles:1 - Sensitivity of analysis variables. Int J Press Vessels Pip 2014;114-115:1-15.

[52] Dean Deng. Influence of deposition sequence on welding residual stress and deformation in an austenitic stainless steel J-groove welded joint. Mater Des 2013;49:1022-33.

[53] Ayjwat A. Bhatti, Zuheir Barsoum, Hidekazu Murakawa, Imad Barsoum. Influence of thermo-mechanical material properties of different steel grades on welding residual stresses and angular distortion. Mater Des 2015;65:878-89.

[54] Guangming Fu, Marcelo I. Lourenco, Menglan Duan, Segen F. Estefen. Effect of boundary conditions on residual stress and distortion in T-joint welds. J Constr Steel Res 2014;102:121–35.

[55] A.C. Oliveira, R.H.M. Siqueira, R. Riva, M.S.F. Lima. One-sided laser beam welding of autogenous T-joints for 6013-T4 aluminium alloy. Mater Des 2015;65:726-36.

[56] C.K. Lee, S.P. Chiew, Jin Jiang. 3D residual stress modelling of welded high strength steel plate-to-plate joints. J Constr Steel Res 2013;84:94–104.

[57] C.K. Lee, S.P. Chiew, Jin Jiang. Residual stress of high strength steel box T-joints Part 1: Experimental study. J Constr Steel Res 2014;93:20–31.

[58] C.K. Lee, S.P. Chiew, Jin Jiang. Residual stress of high strength steel box T-joints Part 2: Numerical study. J Constr Steel Res 2014;98:73–87.

[59] Ding-fa FU, Chang-qing ZHOU, Can LI, Guan WANG, Luo-xing LI. Effect of welding sequence on residual stress in thin-walled octagonal pipe−plate structure. Trans. Nonfer. Met. Soc. China. 2014;24:657-64.

[60] Wenchun Jiang, Yun Luo, B.Y. Wang, S.T. Tu, J.M. Gong. Residual stress reduction in the penetration nozzle weld joint by overlay welding. Mater Des 2014;60:443-50.

[61] Khalid Nasim, A.F.M. Arif, Y.N. Al-Nassar, M. Anis. Investigation of residual stress development in spiral welded pipe. J Mater Process Tec 2015;215:225–38.

[62] Shugen Xu, Weiqiang Wang. Numerical investigation on weld residual stresses in tube to tube sheet joint of a heat exchanger. Int J Press Vessels Pip 2013;101:37-44.

[63] Xiaohui Zhao, Yu Liu, Yong Liu, Yuan Gao. Research on fatigue behavior and residual stress of large-scale cruciform welding joint with groove. Mater Des 2014;63:593-9.

[64] Gurinder Singh Brar, Chandra Shekhar Singh. FEA of residual stress in cruciform welded joint of hollow sectional tubes. J Constr Steel Res 2014;102:44–58.

[65] Mohsen Eshraghi, Mark A. Tschopp, Mohsen Asle Zaeem, Sergio D. Felicelli. Effect of resistance spot welding parameters on weld pool properties in a DP600 dual-phase steel: A parametric study using thermomechanically-coupled finite element analysis. Mater Des 2014;56:387-97.

[66] Jie Xu, Xiaolei Jia, Yu Fan, Anmin Liu, Chonghao Zhang. Residual stress analyses in a pipe welding simulation: 3D pipe versus axi-symmetric models. Proc Mater Sci 2014;3:511-16.

[67] Shugen Xu, Weiqiang Wang, Yinglei Chang. Using FEM to predict residual stresses in girth welding joint of layered cylindrical vessels. Int J Press Vessels Pip 2014;119:1-7.

[68] Fu-Zhen Xuan, Pei-Ning Li. Finite element-based limit load of piping branch junctions under combined loadings. Nucl Eng Des 2004;231:141-50.

[69] M.D. Xue, D.F. Li, K.C. Hwang. Theoretical stress analysis of intersecting cylindrical shells subjected to external loads transmitted through branch pipes. Int J solids struc 2005;42:3299-319.

[70] J.P. Finlay, G. Rothwell, R. English, R.K. Montgomery. Effective stress factors for reinforced butt-welded branch outlets subjected to internal pressure or external moment loads. Int J Press Vessels Pip 2003;80:311-31.

[71] Liping Xue, G. E. O. Widera, Zhifu Sang. Flexibility factors for branch pipe connections subjected to in-plane and out-of-plane moments. J. Pressure Vessel Technol 2006;128:89-94.

[72] Connor. L.P., Welding handbook-welding processes, American Welding Society, vol. 2, edition 8, 1991.

[73] Liang Wang, Sergio D. Felicelli, Phillip Pratt. Residual stresses in LENS-deposited AISI 410 stainless steel plates. Mater Sci Eng A, 2008,496(1-2):234–241.

[74] R. Spina, L. Tricarico, G. Basile, T. Sibillano. Thermo-mechanical modeling of laser welding of AA5083 sheets. J Mater Process Tech, 2007,191:215-219.

[75] Kazuo Ogawa, Dean Deng, Shoichi Kiyoshima, Nobuyoshi Yanagida, Koichi Saito. Investigations on welding residual stresses in penetration nozzles by means of 3D thermal elastic plastic FEM and experiment. Computational Materials Science, 2009,45:1031-1042.

[76] Chaowen Li, Yong Wang, Huanxiao Zhan, Tao Han, Bin Han, Weimin Zhao. Three-dimensional finite element analysis of temperatures and stresses in wide-band laser surface melting processing. Materials & Design, 2010,31:3366-3373.

[77] C.S. Wu, J.S. Sun. Numerical analysis of temperature field during double-sided arc welding of thick materials. Computational Materials Science, 2002, 25:457-468.

[78] C.S. Wu, H.L. Wang, Y.M. Zhang. Numerical analysis of the temperature profiles and weld dimension in high power direct-diode laser welding. Computational Materials Science, 2009, 46:49-56.

[79] J.J. del Coz Díaz, P. Menéndez Rodríguez, P.J. García Nieto, D. Castro-Fresno. Comparative analysis of TIG welding distortions between austenitic and duplex stainless steel s by FEM. Appl Therm Engg. 2010,30:2448-2459.

[80] Yanhong Tian, Chunqing Wang, Danyang Zhu, Y. Zhou. Finite element modeling of electron beam welding of a large complex Al alloy structure by parallel computations. J Mater Process Tech, 2008,199:41-48.

[81] E.F. Rybicki, D.W. Schmueser, R.W. Stonesifer, J.J. Groom and H.W. Mishaler, A Finite Element model for residual stresses and deflections in girth-butt welded pipes, ASME Journal of Pressure Vessel Technology.1978, 100:256–262.

[82] Dong, Y., Hong, J.K., Tsai, C.L. and Dong, P., Finite Element Modeling of Residual Stresses in Austenitic Stainless Steel Pipe Girth Welds, Welding Journal, 1997, 76(10):442-449.

[83] Fricke. S, Keim. E and Schmidt. J, Numerical Weld Modeling - A Method for Calculating Weld-Induced Residual Stresses, Nuclear Engineering and Design, 2001, 206:139-150.

[84] Andreas Lundbäck, Lars-Erik Lindgren, Modelling of metal deposition, Finite Elements in Analysis and Design, 2011, 47(10):1169-1177.

[85] Teng. T.L. and Chang, P.H., Three-Dimensional Thermo-mechanical Analysis of Circumferentially Welded Thin-Walled Pipes, International Journal of Pressure Vessels and Piping, 1998,75: 237-47.

[86] Shoichi Kiyoshima, Dean Deng, Kazuo Ogawa, Nobuyoshi Yanagida, Koichi Saito, Influences of heat source model on welding residual stress and distortion in a multi-pass J-groove joint, Computational Materials Science, 2009 , 46(4): 987-995.

[87] Andres Anca, Alberto Cardona, Jose Risso, Victor D. Fachinotti. Finite element modeling of welding processes, Applied mathematical modeling, 2011,35: 688-707.

[88] Y. Ueda, T. Yamakawa, Analysis of thermal elastic–plastic stress and strain during welding, Trans. Jpn. Weld. Soc. 2 (2) (1971) 90–100.

[89] P. Marcal, Weld Problems, Structural Mechanics Programs, University Press, Charlottesville, 1974. pp. 191–206.

[90] L. Karlsson, Thermomechanical fnite element models for calculation of residual stresses due to welding, in: Hauk et al. (Eds.), Residual Stresses, DGMInformationsgesellschaft Verlag, 1993, p. 33.

[91] J. Goldak, A. Oddy, M. Gu, W. Ma, A. Mashaie, E. Hughes, Coupling heat transfer, microstructure evolution and thermal stress analysis in weld mechanics, in: IUTAM Symposium on the Mechanical Effects of Welding, Springer-Verlag, 1992, pp. 1–30.

[92] R. Radaj, Finite element analysis of welding residual stresses, in: Proceedings of 2nd International Conference on Residual Stresses (ICRS-2), 1988, p.510.

[93] J. Song, J. Peters, A. Noor, P. Michaleris, Sensitivity analysis of the thermomechanical response of welded joints, Int. J. Solids Struct. 40 (2003) 4167–80.

[94] T. Branza, A. Duchosal, G. Fras, F. Deschaux-Beaume, P. Lours, Experimental and numerical investigation of the weld repair of super plastic forming dies, J. Mater. Process. Technol. (2004) 1673–80.

[95] C. Cho, G. Zhao, S.-Y. Kwak, C.B. Kim, Computational mechanics of laser cladding process, J. Mater. Process. Technol. (2004) 494–500.

[96] T.H. Hyde, A.A. Becker, Y. Song, W. Sun, Failure estimation of TIG butt-welded Inco718 sheets at 620 _C under creep and plasticity conditions, Comput. Mater. Sci. 35 (2006) 35–41.

[97] Z. Hou, I.-S. Kim, Y. Wang, C. Li, C. Chen, Finite element analysis for the mechanical features of resistance spot welding process, J. Mater. Process.Technol. 185 (1–3) (2007) 160–165.

[98] M. Mochizuki, Control of welding residual stress for ensuring integrity against fatigue and stress-corrosion cracking, Nucl. Eng. Des. 237 (2) (2007) 107–123.

[99] P. Mollicone, D. Camilleri, T.F. Gray, T. Comlekci, Simple thermo-elastic–plastic models for welding distortion simulation, J. Mater. Process. Technol. 172 (2006) 77–86.

[100] P. Duranton, J. Devaux, V. Robin, P. Gilles, J.M. Bergheau, 3d modelling of multipass welding of a 316l stainless steel pipe, J. Mater. Process. Technol. (2004) 457–463.

[101] P. Ferro, H. Porzner, A. Tiziani, F. Bonollo, The influence of phase transformations on residual stresses induced by the welding process – 3D and 2D numerical models, Model. Simul. Mater. Sci. Eng. 14 (2006) 117–136.

[102] H. Alberg, D. Berglund, Comparison of plastic, viscoplastic, and creep models when modelling welding and stress relief heat treatment, Comput. Methods Appl. Mech. Eng. 192 (2003) 5189–5208.

[103] V. Fachinotti, A. Cardona, Constitutive models of steel under continuous casting conditions, J. Mater. Process. Technol. 135 (2003) 30–43.

[104] Mohsen Eshraghi, Mark A. Tschopp, Mohsen Asle Zaeem, Sergio D. Felicelli. Effect of resistance spot welding parameters on weld pool properties in a DP600 dual-phase steel: A parametric study using thermomechanically-coupled finite element analysis. Mater Des 2014;56:387-97.

[105] S.A. Tsirkas, P. Papanikos, Th. Kermanidis. Numerical simulation of the laser welding process in butt-joint specimens. J Mater Process Tec 2003;134:59–69.

[106] U. Peil, M. Wichers, Schweißen unter Betriebsbeanspruchung - Numerische und experimentelle Bestimmung des Temperaturfeldes beim Schweißen. Stahlbau 74, 11, 2005.

[107] A. N. Brink, Einsatz der Impuls-Thermografie zur quantitativen zerst¨orungsfreien Pr¨ufung im Bauwesen. Diss., Thechnische Universit¨at Berlin 2004.

[108] N. Schuster, V. G. Kolobrodov Infrarotthermographie. Wiley-VCH, 2004.

[109] E.M. Vander. Finite Element Modeling of Temperature Profiles, Distortions and Residual Stresses due to TIG Welding - M. Sc Thesis, Delft University of Technology, 2003.

[110] A. Ravisankar, Satish K. Velaga, Gaurav Rajput, S. Venugopal. Influence of welding speed and power on residual stress during gas tungsten arc welding (GTAW) of thin sections with constant heat input: A study using numerical simulation and experimental validation. J Manuf Processes 2014;16:200-11.

[111] X.K. Zhu, Y.J. Chao. Numerical simulation of transient temperature and residual stresses in friction stir welding of 304L stainless steel. J Mater Process Tec 2004;146:263–72.

[112] Mir Zahedul H. Khandkar, Jamil A. Khan, Anthony P. Reynolds, Michael A. Sutton. Predicting residual thermal stresses in friction stir welded metals. J Mater Process Tec 2006;174:195–203.

[113] Sysweld reference manual and material data, ESI group; 2012.

[114] V. Pavelic, R. Tanbakuachi, O. A. Uyehara, P. S. Myers. Experimental and computed temperature histories in Gas Tungsten Arc Welds in thin plates. Welding journal research supplement, 1975; 48:295s-305s.

[115] V. Pavlyk, U. Dilthey. A numerical and experimental study of fluid flow and heat transfer in stationary GTA weld pools. H. Cerjak (ed.) Mathematical modeling of weld phenomena 5, The institute of materials, 2001.

[116] Norton JT. X-ray determination of residual stress. Mater Eval 1973,February;31:21A.

[117] Noyan IC, Cohen JB. Residual stress-measurement by diffraction and interpretation. In: IIschner B, Grant NJ, editors. A very complete treatment of stress andstress tensors and how stresses are measured in polycrystalline samples. NewYork: Springer-Verlag;1987.

[118] N.S. Rossini, M. Dassisti, K.Y. Benyounis, A.G. Olabi. Methods of measuring residual stresses in components. Mater Des 2012;35:572-88.

[119] Muhammad Ejaz Qureshi. Analysis of residual stresses and distortions in circumferentially welded thin-walled cylinders. Ph.D. Dissertation, National university of science and technology; 2008.

[120] Muhammad Zain-ul-abdein, Daniel Nélias, Jean-François Jullien, Fréderic Boitout, Luc Dischert, Xavier Noe. Finite element analysis of metallurgical phase transformations in AA 6056-T4 and their effects upon the residual stress and distortion states of a laser welded T-joint. Int J Press Vessels Pip 2011;88:45-56.